



저작자표시-동일조건변경허락 2.0 대한민국

이용자는 아래의 조건을 따르는 경우에 한하여 자유롭게

- 이 저작물을 복제, 배포, 전송, 전시, 공연 및 방송할 수 있습니다.
- 이차적 저작물을 작성할 수 있습니다.
- 이 저작물을 영리 목적으로 이용할 수 있습니다.

다음과 같은 조건을 따라야 합니다:



저작자표시. 귀하는 원저작자를 표시하여야 합니다.



동일조건변경허락. 귀하가 이 저작물을 개작, 변형 또는 가공했을 경우에는, 이 저작물과 동일한 이용허락조건하에서만 배포할 수 있습니다.

- 귀하는, 이 저작물의 재이용이나 배포의 경우, 이 저작물에 적용된 이용허락조건을 명확하게 나타내어야 합니다.
- 저작권자로부터 별도의 허가를 받으면 이러한 조건들은 적용되지 않습니다.

저작권법에 따른 이용자의 권리는 위의 내용에 의하여 영향을 받지 않습니다.

이것은 [이용허락규약\(Legal Code\)](#)을 이해하기 쉽게 요약한 것입니다.

[Disclaimer](#) 

공학박사학위논문

원자층 증착법을 이용한 SnO₂, TiO₂ 박막의
성장과 성장된 박막의 구조적 특성
및 수소 가스 감응 특성 연구

Growth of SnO₂ and TiO₂ thin films by PE-ALD
: their structural characteristics
and H₂ gas sensing properties

2014 년 8 월

서울대학교 대학원

재료공학부

김 대 홍

원자층 증착법을 이용한 SnO₂, TiO₂ 박막의
성장과 성장된 박막의 구조적 특성
및 수소 가스 감응 특성 연구

Growth of SnO₂ and TiO₂ thin films by PE-ALD
: their structural characteristics
and H₂ gas sensing properties

지도교수 홍성현

이 논문을 공학박사 학위논문으로 제출함

2014년 8월

서울대학교 대학원

재료공학부

김대홍

김대홍의 공학박사 학위논문을 인준함

2014년 7월

위원장 김형준 印

부위원장 홍성현 印

위원 장호원 印

위원 이종훈 印

위원 김영민 印

Abstract

Growth of SnO₂ and TiO₂ thin films by PE-ALD : Their structural characteristics and H₂ gas sensing properties

Dai-Hong Kim

Department of Material Science and Engineering

The Graduate School

Seoul National University

One of the potential alternatives for the fossil fuels is hydrogen (H₂) gas because it is renewable and clean. However, a high flammability and explosiveness of H₂ in the gas storage are great problems. Therefore, the detection of the H₂ gas from leakage is indispensable for safety. Gas sensors for H₂ gas have been studied and commercially available for many years. In order to meet the demands of future H₂ gas applications, however, many researches are conducted to improve low cost, low working temperature (below 100 °C), selectivity (NO_x, EtOH, H₂O, etc) and reliability in addition to reducing sensor size.

In this research, semiconductor type metal oxide gas sensor is attracted due to low cost and high sensitivity toward H₂ gas and plasma enhanced atomic layer deposition (PE-ALD) is used to control variables such as thickness and morphology. As sensing materials, SnO₂ and TiO₂ which are most widely studied materials for H₂ gas sensor are

chosen. The three main topics will be discussed to investigate gas sensing mechanism and enhance gas sensing performance: 1) Oriented SnO₂ thin films grown on TiO₂ single crystals, 2) Brookite TiO₂ thin film epitaxially grown on YSZ substrates, 3) SnO₂-TiO₂ dual layer gas sensors.

The first and second topics are focused on investigating gas sensing mechanism. Theoretical studies of gas adsorption and desorption on specific crystallographic planes or phases have been conducted. Although gas sensing performance is strongly depended on gas adsorption on a specific crystallographic plane or phases, the study of relationships between gas sensing performance and crystallographic planes or phases is very limited due to morphology change caused by crystallographic change. Therefore, in this study, I tried to separate of variables using epitaxial deposition methods to control the crystallographic planes or phases without morphology change.

First, epitaxial SnO₂ films were deposited on TiO₂ single crystals with various orientations by PE-ALD, and their structural characteristics and gas sensing properties were investigated, particularly focusing on the crystallographic orientation dependence of H₂ gas response. Dibutyltindiacetate (DBTDA) was used as Sn source, and (100), (001), (110), and (101) TiO₂ were employed as substrates for SnO₂ deposition. All the SnO₂ films were ~90 nm thick after 1000 ALD cycles and epitaxially grown on TiO₂ substrates, which were confirmed by X-ray pole figure and high resolution transmission electron microscopy (HRTEM). Differently oriented epitaxial SnO₂ films

showed the different H₂ gas response and different temperature dependence of gas response. The (101) SnO₂ films grown on (101) TiO₂ exhibited the highest H₂ gas response of ~380 toward 1000 ppm H₂/air at 400 °C, which was associated with the different temperature dependence of resistance in (101) film rather than the microstructural characteristics and chemical composition compared to the other films.

Next, epitaxial brookite TiO₂ (B-TiO₂) film was deposited on (110) YSZ substrate using PE-ALD and its structural, optical, and gas sensing properties were investigated. Chemical states and morphology of the TiO₂ film were investigated by XPS and AFM. X-ray diffraction, X-ray pole figure, and high resolution TEM analyses revealed that deposited TiO₂ film was pure B-TiO₂ and highly oriented to (120) plane. The determined in-plane orientation relationships were $[2\bar{1}0]_{\text{B-TiO}_2} \parallel [\bar{1}10]_{\text{YSZ}}$ and $[001]_{\text{B-TiO}_2} \parallel [001]_{\text{YSZ}}$ and lattice mismatches were -1.91 and 0.06 %. Phase of B-TiO₂ film was unchanged at 700 °C heat treatment and the sensor showed stable and high sensing properties for H₂ gas. The highest magnitude of the gas response ($R_{\text{air}}/R_{\text{gas}}$) was determined to be ~150 toward 1000 ppm H₂/air at 150 °C. In addition, B-TiO₂ sensor showed a high selectivity for H₂ against CO, EtOH, and NH₃.

The last topic is concentrated to enhance high sensing ability and selectivity in addition to low working temperature and low cost using silicon substrate. Although SnO₂ thin film is extensively studied in H₂ gas sensor owing to high gas sensing performance, most SnO₂

thin film sensors have great problems to be commercialized because of high working temperature and low selectivity. First, to reduce working temperature, the thickness effect of SnO₂ gas sensor is studied. When the thickness of SnO₂ thin film is ~ 4 nm which is near debye length, the maximum gas response was exhibited at low temperature (below 100 °C) but the sensors have still poor selectivity. To enhance the gas selectivity, SnO₂-TiO₂ dual layer gas sensor was suggested. When TiO₂ was deposited on SnO₂, the gas response was increased and the optimum thickness was ~ 4 nm of SnO₂ and ~ 4 nm of TiO₂. Dual layer sensor showed the excellent gas selectivity against NO_x gas compared with SnO₂ single layer sensor. Although the dual layer sensors exhibited poor selectivity against humidity, the problem is solved with adjusting of operating temperature up to 100 °C.

Keywords: gas sensor, semiconductor type gas sensor, metal oxide, H₂ gas sensor, thin film, tin dioxide (SnO₂), titanium dioxide (TiO₂), atomic layer deposition, epitaxy, brookite, dual-layer, gas selectivity

Student number: 2008-30847

Table of Contents

Chapter 1. Introduction	1
Chapter 2. Literature survey	6
2.1. Semiconductor metal oxide gas sensor	6
2.1.1. Sensing mechanism of gas sensor	6
2.1.2. Main factor of gas sensor	7
2.1.3. H ₂ gas sensor	9
2.2. SnO ₂ and SnO ₂ based gas sensor for H ₂ gas	13
2.3. TiO ₂ and TiO ₂ based gas sensor for H ₂ gas	20
2.4. Epitaxial thin films and their gas sensing performance	29
2.5. Atomic layer deposition and epitaxial films	34
Chapter 3. Experimental	38
3.1. ALD deposition and precursor	38
3.2. SnO ₂ and TiO ₂ deposition	39
3.3. Characterization	40
3.4. Gas sensor measurement	41

Chapter 4. Results and discussions	47
4.1. Oriented SnO ₂ thin films grown on TiO ₂ single crystals	47
4.1.1. Structural characterization	47
4.1.2. Gas sensing properties	50
4.2. Brookite TiO ₂ thin film epitaxially grown on YSZ substrates	64
4.2.1. Structural characterization	64
4.2.2. Gas sensing properties	68
4.3. SnO ₂ -TiO ₂ dual layer gas sensors	85
4.3.1. SnO ₂ and TiO ₂ single layer gas sensor	85
4.3.2. Structure of SnO ₂ -TiO ₂ dual layer	86
4.3.3. Gas sensing properties of SnO ₂ -TiO ₂ dual layer	88
4.3.4. Gas selectivity of SnO ₂ -TiO ₂ dual layer	89
4.3.5. Gas sensing mechanism	90
Chapter 5. Conclusions	102
References	105
Abstract (Korean)	113

List of Figures and Tables

Figures

Figure 2.1. The mechanism of H₂ gas sensing in SnO₂ gas sensor

Figure 2.2. The hydrogen sensing mechanism of metal oxide semiconductor gas sensor

Figure 2.3. (a) A simple model for selectivity and sensing mechanism to hydrogen, (b) Dependence of sensor output in H₂ and C₂H₅OH with air [14]

Figure 2.4. Sensing properties of the ZnO-modified SnO₂ nanorod sensors at 350 °C: (a) H₂ gas selectivity; (b) sequential response to H₂ concentrations; (c) n-p-n transition response; (d) the resistance change after 2000 ppm H₂ gas; (e) effect of the relative humidity; (f) nanoprobe EDX line-scan analysis [10]

Figure 2.5. (a) SEM and TEM images of SnO₂ NWs and Sn NPs (b) The schematic images of the SnO₂ sensors competing one hydrogen cycle in air and in N₂ [11]

Figure 2.6. (a) H₂ gas sensitivity at 150 °C as a function of sputtering time. (b) A model illustrating the effect of film thickness on the depletion region. [23]

Figure 2.7. (a) The surface morphology of the titania nanoporous structure and (b) H₂ gas response transient with various concentrations at 500 °C [34]

Figure 2.8. (a) A schematic illustration showing the configuration for measurement of sensing, (b) Hydrogen (1000 ppm in N₂)-induced electrical switching from the off to the on state with a current ~0.3 μA, and schematic depictions of the two major processes taking place at the Pd-TiO₂ surface (c) in air and (d) in H₂ [36]

Figure 2.9. (a) Cross-sectional FE-SEM images of the TiO₂ nanotube arrays and (b) H₂ gas response of TiO₂ nanotubes with temperature variations [37]

Figure 2.10. (a) I-V characteristics of the Pt/TiO₂ nanotube arrays sensors at room temperature in different ambient and (b) The response behavior of sensors with Pt or Pt/Ti electrodes [39]

Figure 2.11. (a) SEM images of the surface of as-prepared A-TiO₂ nanotubes and (b) H₂ sensing mechanism based on variation in Shottky barrier height [42]

Figure 2.12. Typical gas-sensing characteristics of three types of SnO₂ whiskers, (a) a [101] whisker, (b) a [010] whisker, (c) a [110] whisker [44]

Figure 2.13. (a) XRD patterns of TiO₂ films grown on various sapphire substrates and (b) the sensitivity of TiO₂ thin films with concentration dependence [35]

Figure 2.14. (a) XRD patterns of SnO₂ films grown on various sapphire substrates and (b) the sensitivity of TiO₂ thin films with concentration dependence [45]

Figure 2.15. (a) Film growth model of CVD and ALD process, (b) layer by layer deposition with number of cycles by ALD [77]

Figure 2.16. Model of epitaxial deposition [80]

Figure 3.1. (a) PE-ALD system of this experiment and (b) schematic diagram of PE-ALD system

Figure 3.2. Molecular structures of (a) Dibutyl tin Diacetate (DBTDA) as Sn precursor and (b) Titanium Tetraisopropoxide (TTIP) as Ti precursor

Figure 3.3. (a) Electrode structure of thin film gas sensor and (b) Schematic diagram of gas sensor measurement system [58]

Figure 4.1. XRD patterns of SnO₂ thin films deposited on (a) (100), (b) (001), (c) (110), and (d) (101) TiO₂ substrates.

Figure 4.2. {101} pole figures of the SnO₂ deposited on the (a) (100), (b) (001), (c) (110), and (d) (101) TiO₂ substrates.

Figure 4.3. (a) Low magnification TEM image of (110) SnO₂ film grown on (110) TiO₂ substrate and HRTEM images of SnO₂/TiO₂ interfaces for the films grown on (b) (100), (c) (001), (d) (110), and (e) (101) TiO₂ substrates.

Figure 4.4. AFM topographic images of the SnO₂ films grown on (a) (100), (b) (001), (c) (110), and (d) (101) TiO₂ substrates.

Figure 4.5. (a) Sn3d and (b) O1s core level XPS spectra of the SnO₂ films deposited on (100), (001), (110), and (101) TiO₂ substrates.

Figure 4.6. Response transient of the SnO₂ films grown on (101) TiO₂ substrate toward H₂ gas (100–1000 ppm) measured at 400 °C.

Figure 4.7. Magnitude of gas response (S) toward 1000 ppm H₂/air in the films grown on (100), (001), (110), and (101) TiO₂ substrates as a function of sensing temperature.

Figure 4.8. Electrical resistance of the SnO₂ films in air and in 1000 ppm H₂/air as a function of sensing temperature deposited on (a) (100), (b) (001), (c) (110), and (d) (101) TiO₂ substrates.

Figure 4.9. Magnitude of gas response (S) toward 1000 ppm (a) ethanol, (b) NH_3 , and (c) CO gases in the films deposited on (100), (001), (110), and (101) TiO_2 substrates as a function of sensing temperature.

Figure 4.10. Surface morphology of as-deposited TiO_2 film grown on (110) YSZ at the substrate temperature of (a) 100, (b) 300, and (c) 500 °C.

Figure 4.11. Cross-sectional TEM image of as-deposited TiO_2 film grown on (110) YSZ.

Figure 4.12. (a) Ti2p and (b) O1s core level XPS spectra of as-deposited TiO_2 film grown on (110) YSZ.

Figure 4.13. XRD patterns of (a) as-deposited and annealed (at 700 °C for 1 h) TiO_2 films grown on (110) YSZ at 300 °C and (b) TiO_2 films with deposition temperature variations. The reference is the standard diffraction pattern of brookite TiO_2 (ICDD #29-1360).

Figure 4.14. {120} pole figure of as-deposited TiO_2 film grown on (110) YSZ.

Figure 4.15. HRTEM images and FFT patterns for B- TiO_2 film and YSZ viewed along (a) $[00\bar{1}]$ and (b) $[1\bar{1}0]$ directions of YSZ. (c) Schematic diagrams of in-plane atomic configurations for (120) B- TiO_2 film and (110) YSZ substrate.

Figure 4.16. (a) HRTEM image and FFT patterns for B-TiO₂ film viewed along along [00 $\bar{1}$] direction of YSZ. (120) B-TiO₂ and 180° rotated (120) B-TiO₂ films were observed, which was consistent with pole figure data. (b) Schematic diagrams of in-plane atomic configurations for (120) and 180 rotated (120) B-TiO₂ films on (110) YSZ substrate.

Figure 4.17. Optical transmittance spectra of B-TiO₂ film and bare YSZ substrate. The inset shows a plot of $(\alpha E)^2$ vs. E for B-TiO₂ film.

Figure 4.18. (a) Typical response transient of the B-TiO₂ film toward H₂ gas/air (1000-100 ppm) measured at 150 °C. (b) Magnitude of gas response toward 1000 ppm H₂/air in the films grown on (110) YSZ and (110) Al₂O₃ substrates as a function of sensing temperature. (c) Electrical resistances of the films grown on (110) YSZ and (110) Al₂O₃ substrates in air and 1000 ppm H₂/air as a function of operating temperature. (closed circles : resistance in air (R_{air}), open circles : resistance in 1000 ppm H₂/air (R_{gas})).

Figure 4.19. XRD pattern of TiO₂ film deposited on a-cut (110) Al₂O₃ substrate.

Figure 4.20. HRTEM images and FFT patterns for the films deposited on (a) (100) and (b) (111) YSZ substrates.

Figure 4.21. Magnitude of H₂ gas response for the films deposited on (100), (110), and (111) YSZ substrates.

Figure 4.22. Magnitude of gas response for 1000 ppm CO, EtOH, and NH₃ in B-TiO₂ film sensor.

Figure 4.23. Magnitude of gas response to 1000 ppm H₂/air and electrical resistance of SnO₂ thin film annealed at 400 °C ((a) and (b)) and 600 °C ((c) and (d))

Figure 4.24. Magnitude of gas response to 1000 ppm H₂/air of TiO₂ thin film with temperature variations

Figure 4.25. High resolution TEM image and EDS profiles of SnO₂-TiO₂ dual layer sensors with annealing temperature variations: (a) as deposited, (b) annealed at 450 °C, and (c) annealed at 600 °C

Figure 4.26. AFM images of SnO₂-TiO₂ dual layer sensors with annealing temperature variations: (a) as deposited, (b) annealed at 450 °C, and (c) annealed at 600 °C

Figure 4.27. Gas response transients of SnO₂-TiO₂ dual layer sensors with annealing temperature variations

Figure 4.28. Gas response and electrical resistance of SnO₂-TiO₂ dual layer sensors (a) and (b) with processing cycle variations of SnO₂, and (c) and (d) with processing cycle variations of TiO₂

Figure 4.29. (a) Low temperature gas response of SnO₂-TiO₂ dual layer sensor with electrode variations and (b) I-V characteristics of SnO₂-TiO₂ dual layer sensor at 25 °C

Figure 4.30. Gas response transient of SnO₂ single layer gas sensor (a) at 25 °C and (b) at 100 °C, and gas response transient of SnO₂-TiO₂ dual layer gas sensor (c) at 25 °C and (d) at 100 °C.

Figure 4.31. Humidity influences of SnO₂-TiO₂ dual layer sensor (a) at 25 °C, and (b) at 100 °C

Figure 4.32. Gas response of various reduction gases (1000 ppm H₂/air, 1000 ppm EtOH/air, 1000 ppm NH₃/air) on SnO₂-TiO₂ dual layer sensor measured at 100 °C.

Tables

Table 2.1. Selective or low operating temperature SnO₂ gas sensors [10, 11, 14-23]

Table 2.2. Comparison of three TiO₂ phases (Rutile, Anatase, Brookite) [ICDD # 21-1276 (Rutile), # 21-1272 (Anatase), # 29-1360 (Brookite)]

Table 2.3. TiO₂ based H₂ gas sensors in the literature [12, 34-43]

Table 3.1. Deposition conditions of SnO₂ and TiO₂ thin films

Chapter 1. Introduction

1) The necessity of H₂ gas sensor

Hydrogen (H₂) gas with high heat of combustion energy (142 kJ/g) has been attracted as the best clean energy carriers, which is the ultimate fossil fuel candidates, due to renewable, clean, and abundant in air [1]. The combustion product of H₂ gas is water and can be converted into hydrogen and oxygen again [2]. However, a high flammability and explosiveness of H₂ gas under low ignition energy (0.017 mJ) and a concentration range (4–75%) are great problem [1]. H₂ gas is tasteless, colorless and odorless so it cannot be detected by human beings. Therefore rapid and accurate hydrogen detection is necessary during the storage and use of hydrogen.

Among the various H₂ sensors, metal oxide (mainly SnO₂) gas sensor has been mostly conducted due to high sensitivity, low cost, and good compatibility to silicon microfabrication [3]. The working mechanism of metal oxide H₂ gas sensors is represented the convection of electrical conductivity surface reactions and many researchers have developed various nanostructures as gas sensor materials due to high surface to volume ratio [4]. However, these sensors have still limitation of high operating temperature, reproducibility, and H₂ gas selectivity. To solve these problems, the influence factors for enhancing gas

sensing properties should be precisely investigated.

2) Factor of sensing properties

The performance of metal oxide gas sensors is strongly influenced by the surface morphology, composition, crystallographic structure [5]. Most researchers have been focused on morphology and composition effects due to effective and easy handling factors to enhance gas sensing properties [5,6]. The crystallographic structure is another important factor to decide the electrical, optical, and electrochemical properties and many researches have investigated to find out the dependence of these properties on crystallographic structure. However, gas sensing properties depending on crystallographic structure has been barely investigated because of difficulty in controlling crystallographic planes and phases. Epitaxial films with a single orientation and few grain boundaries can be suggested to study effect of crystallographic structure on gas sensing properties without other influences such as morphology and composition. For example, the epitaxial films are expected to produce more uniform and homogenous adsorption and desorption kinetics, which provides the fundamental understanding of gas sensing mechanism isolating from the grain boundary effect [7].

3) Thin film gas sensor

Thin film gas sensor using deposition equipment has great advantages comparing other nanostructure gas sensors due to simple integration, reproducibility, and established controlling system. Among the various deposition methods, ALD is a promising technique to produce ultra-thin films through a self-limiting surface reaction. The advantage of this technique lies in accurate and simple thickness control by number of cycles, good conformality, capability to produce sharp interfaces and multilayer structures, large area capability, and so on [8]. Especially, plasma enhanced atomic layer deposition (PEALD) has great advantages such as less limitation of precursor selections and obtaining crystalline thin films by O₂ plasma.

4) Objectives and scope of research

The objective of this research includes:

- Effect of crystallographic plane on gas sensor
- Effect of crystalline phase on gas sensor
- To fabricate low temperature and high gas response H₂ gas sensor

In this thesis, to confirm the gas sensing dependence of thin film structures and to enhance the gas sensing properties, three main works were performed using PE-ALD.

The first work is gas sensing dependences of oriented SnO₂ thin films. Single crystal SnO₂ is not commercially available and epitaxial films with a single like orientations are alternative to study their gas sensing properties. Therefore, SnO₂ thin films were deposited on the four kinds of TiO₂ single crystal substrates ((100), (001), (110), and (101)) and their gas sensing properties are investigated.

Next, B-TiO₂ films were grown for H₂ gas sensor. TiO₂ exhibits three polymorphs in nature: anatase (A-TiO₂, tetragonal), brookite (B-TiO₂, orthorhombic), and rutile (R-TiO₂, tetragonal). Each crystalline phase has different optical, electrical, and photochemical properties, and the performance of TiO₂ strongly depends on the crystal structure, morphology, and size of the particles. Anatase and rutile phases have been extensively studied and widely used in the form of powders and thin films. On the contrary, pure brookite phase is difficult to prepare in either form and there are no reports on gas sensing properties of pure B-TiO₂. B-TiO₂ epitaxial films are successfully

grown on (110) YSZ substrate and the sensing properties of B-TiO₂ sensor are compared to R-TiO₂ sensor.

The last one is low temperature H₂ gas sensing properties of SnO₂-TiO₂ dual-layer. To fabricate effective H₂ gas sensor, manufacturing cost, low working temperature and gas selectivity to H₂O, NO_x should be considered. Therefore, sensing properties of SnO₂, TiO₂, and SnO₂-TiO₂ dual layer sensors grown on SiO₂ substrate are investigated with thickness variations, respectively. Also, the mechanism of H₂ selective sensing at low temperature is discussed.

In the each part, their structural characteristics were determined using X-ray pole figure and high resolution transmission electron microscopy (HRTEM) and H₂ gas sensing properties depended on thin film structure were also discussed.

Chapter 2. Literature survey

2.1. Semiconductor metal oxide gas sensor

It has been known since the 1950s that the electrical properties of metal oxides change when they are exposed to reducing gases [1,9]. In 1962 Seiyama and Taguchi was applied this phenomenon to detection low concentration of combustible and reducing gases using ZnO and SnO₂ based semiconductors, respectively [1,9]. Typically a metal-oxide film is mounted on an insulating substrate with two metal electrodes. During sensor operation, the film is heated to high temperature to promote reaction with the target gases. Therefore, the metal oxides which are stable at high temperature are mainly used such as SnO₂, ZnO, TiO₂, Fe₂O₃, NiO, Ga₂O₃, In₂O₃, Sb₂O₅, MoO₃ and WO₃ are mainly used. These metal oxide gas sensors have a great advantage due to a simple circuit, cheap manufacturing prices and a lot of detecting gases including combustible and toxic gases.

2.1.1. Sensing mechanism of gas sensor

Mechanism of semiconducting oxide gas sensors is simply represented electrical resistance changes following adsorption and desorption of gases on the metal oxide surface [1,9]. Figure 2.1 exhibited H₂ sensing mechanism of

SnO₂. The SnO₂, a typical gas sensing material, is n-type semiconductor and the oxygen lattice defects of SnO₂ act as electron donor. When the oxygen molecules adsorb on the surface, the oxygen atoms pick up the electrons from the conduction band of SnO₂ resulting in the space charge layer and reaction is simply expressed by $O_2 + 2e^- \rightarrow 2O^-_{ads}$. These space charge layers act as the barrier for the electronic conduction in figure 2.1 (a). When the sensor is exposed to the reducing gases such as H₂, the oxygen adsorbates react with the reducing gases and release the electrons to the conduction band, which decreases the potential barrier and increase the electrical conductivity. The reduction reactions can be represented by $H_2 + O^-_{ads} \rightarrow H_2O + e^-$. Gas sensors measure the electrical resistance changes under a fixed applied voltage or current.

2.1.2. Main factor of gas sensor

The performances of gas sensors are evaluated by the magnitude of gas response, selectivity, response & recovery time, and reproducibility & stability.

The magnitude of gas response of gas sensor is the most important factor to estimate the sensor performances and means the conductance or resistance changes during gas reactions and typically exhibited by equation below.

$$S \text{ (the magnitude of gas response)} = R_a/R_g$$

(R_a : resistance under air or reference gas, R_g : resistance under target gas)

The selectivity means the ability to distinguish a specific target gas among various gases. The selectivity of A gas to B gas is expressed by below equation under mixing A gas with B gas.

$$\text{Selectivity} = S_A/S_B$$

(S_A : the magnitude of gas response at A gas, S_B : the magnitude of gas response at B gas)

Most metal oxide gas sensors including SnO_2 exhibited the poor selectivity because metal oxides simultaneously react with various gases (H_2 , CO , H_2S , EtOH , NO_x , etc) [10].

The response and recovery time ($t_{90\%}$) indicate the spending time until stable reaction after reacting target gas and reference gas. It generally is obtained by the time considering about 90 % value of stable resistance. The short response and recovery time means fast response to target gas and fast recover to reference gas. The response & recovery time is concerned by activation energy of gas reaction. Therefore, most sensors are modified to reduce the activation energy using high temperature heater or metal catalyst loading. [11]

Reproducibility & stability of gas sensor exhibit the ability to recover the original sensing property and the biggest problem to solve in metal oxide gas sensor. In the metal oxide gas sensor, nanostructures have been attributed by

high performance gas sensor due to high surface to volume ratio but nanostructure has also a great problem reproducibility & stability due to easy grain growth.

2.1.3. H₂ gas sensor

The mechanism of H₂ gas detection on metal oxide gas sensors have been investigated by many researchers. The commonly accepted mechanism is based on the variation of the surface electron depletion region which is discussed in the part 2-1-1. Another mechanism is dissociated hydrogen atoms are used for chemisorption on the film surface besides desorption of oxygen species. As reported, hydrogen dissociated on the surface of a metal oxide induces an intermediate level for the transfer of charges from hydrogen to the conduction band. Therefore, accumulation layer of electrons is created in a metalized region on surface. In figure 2-2, two possible H₂ sensing mechanisms are illustrated [2,12].

Hydrogen sensors have been commercially available for many years. In order to meet the demands of a future hydrogen economy however, a lot of research is ongoing to continuously improve sensitivity, selectivity, response time and reliability in addition to reducing sensor size, cost and power consumption. These demands on hydrogen sensors can be summarized as follows [1,13]:

- Indication of hydrogen in concentration range 0.01–10% (safety) or 1–100% (fuel cells)
- Reliable results of sufficient accuracy and sensitivity
- Stable signal with low noise
- Robustness including low sensitivity to environmental parameters such as:
 - temperature (–30–80 °C (safety), 70–150 °C (fuel cells))
 - pressure (80–110 kPa)
 - relative humidity (10–98%)
 - gas flow rate
- fast response and recovery time (<1 s)
- High selectivity (e.g. hydrocarbons, CO, H₂S, NO_x)
- long life time (>5 years)
- low power consumption (<100 mW)
- low cost
- small size
- simple system integration and interface

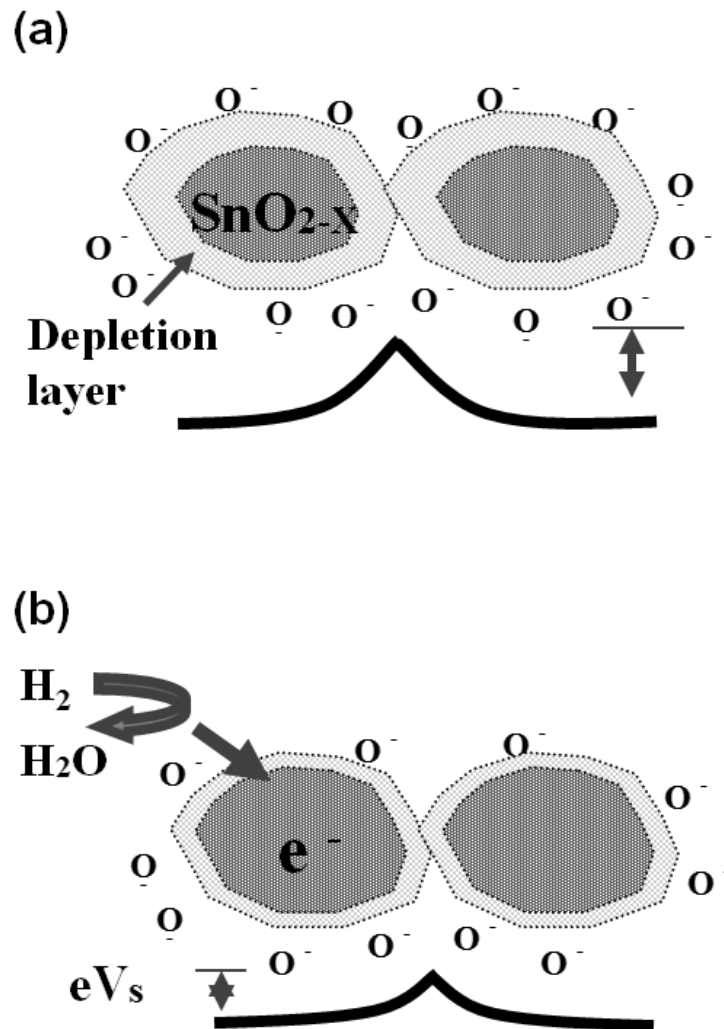


Figure 2.1. The mechanism of H_2 gas sensing in SnO_2 gas sensor

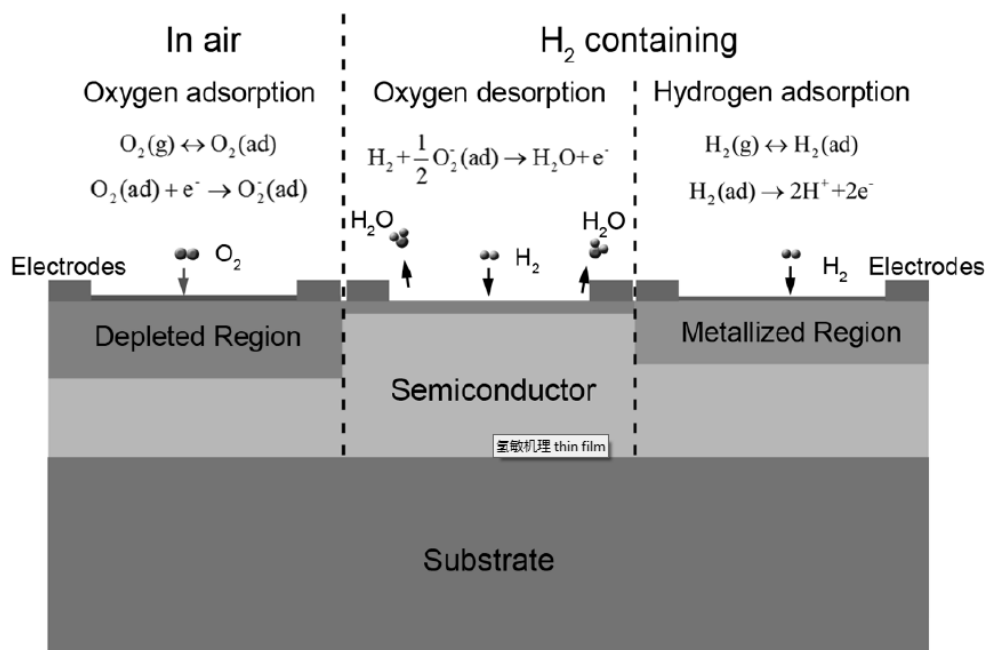


Figure 2.2. The hydrogen sensing mechanism of metal oxide semiconductor gas sensor [2]

2.2. SnO₂ and SnO₂ based gas sensor for H₂ gas

Tin dioxide (SnO₂) is a wide band gap (3.6 eV) n-type semiconductor and extensively used in the gas sensor materials. Since the high H₂ gas sensing properties of nanocrystalline SnO₂-based sensor in various forms (thin / thick film and pellets) are well known, much attention has been paid recently to understand the low operating temperature (< 100 °C) and H₂ gas selectivity. Several reports to enhance H₂ gas selectivity or low temperature gas sensing of SnO₂ gas sensor are summarized in Table 2.1.

To enhance H₂ gas selectivity of SnO₂ gas sensor, other metal oxides such as SiO₂ and ZnO are coated on SnO₂ surface. A. Katsuki et al. [14] exhibited the highly selective H₂ gas sensor based on a hot wire type gas sensor with dense layer of 0.1 mm by SiO₂ CVD coating illustrated in Figure 2.3. The dense layer functioned as a ‘molecular sieve’; thereby the diffusion of gases with large molecular diameters, except for H₂, was effectively controlled. Also, addition effect of cerium oxide was investigated and the sensors showed significantly minor humidity dependence and prominent long term stability. Hui Huang et al. [10] fabricated ZnO coated SnO₂ nanorods using PE-CVD and spin coating method to enhance gas selectivity and humidity dependence in Figure 2.4. The type of gas sensing properties are changed with H₂ concentration and showed excellent selectivity to other gases such as CO, NH₃, and CH₄.

Low temperature gas sensing was related with activation energy of gas reaction. Generally the maximum gas response is occurred at 300 ~ 400 °C conducted but in the industry, low operating temperature under 100 °C. To fabricated low operating gas sensors, catalyst doping or decorating such as Pt, Pd, In₂O₃, and F is usually used to reduce activation energy. Lee et al. [11] exhibited room temperature high H₂ gas sensor using Pd-decoration with fast gas response in Figure 2.5. Also, the mechanism of SnO₂ sensors is discussed with schematic illustrations. There is a report which is conducted at low operating temperature without catalyst. Suzuki et al. [23] deposited thin film SnO₂ using ion-beam sputtering with various film thickness and measured H₂ gas sensing properties to find out thickness effects as shown Figure 2.6. The maximum gas responses at relatively low temperature at 150 °C realized by ultra-thin SnO₂ thin films which is near to depletion layer about 5 nm.

Materials	Synthesis	Working Temp. (°C)	Detected Conc. (ppm)	S _{max}	Ref.
SnO ₂ -SiO ₂ (bulk)	Sintering	480	High selectivity using molecular sieve		[14]
SnO ₂ -SiO ₂ HMDS (thick film)	Sol-gel Screen-printing CVD	500 (100~500)	500 (0.25~500)	~ 170	[15]
SnO ₂ (nanotube)	Electro-spinning	150 (100~200)	10000 (600~10000)	~ 2.5	[16]
SnO ₂ (thin film)	Sol-gel Spin-coating	150 (90~150)	1000 (1000~5000)	5~100	[17]
SnO ₂ -ZnO (nanowire)	PE-CVD Spin-coating	350	100 (10~3000)	~ 10	[10]
SnO ₂ -Sn, Pd dot (nanowire)	Thermal evaporation	R.T.	10000 (40~10000)	7*10 ⁴	[11]
SnO ₂ -RGO-Pt (nanopowder)	Microwave assisted method	50 (25~50)	10000 (5000~30000)	~ 3	[18]
SnO ₂ -In ₂ O ₃ (nanopowder)	Sol-gel	22 (R.T.)	15000 (100~15000)	3*10 ⁵	[19,20, 21]
SnO ₂ -F doped (nanopowder)	Sol-gel	R.T.	600 (100~600)	4.5	[22]
SnO ₂ (thin film)	Ion-beam sputtering	100 (150~350)	4700	13	[23]

Table 2.1. Selective or low operating temperature SnO₂ gas sensors [10, 11, 14-23]

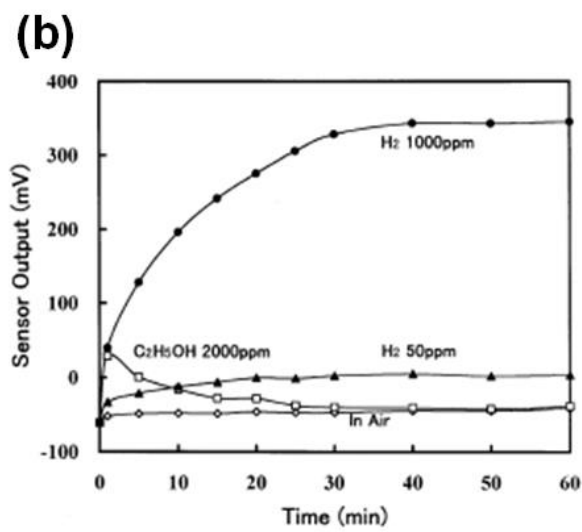
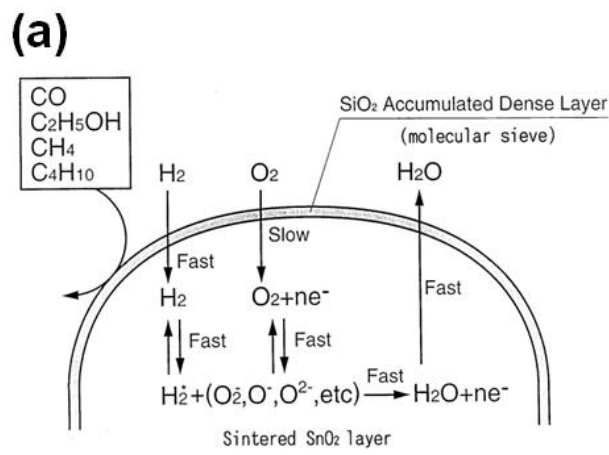


Figure 2.3. (a) A simple model for selectivity and sensing mechanism to hydrogen, (b) Dependence of sensor output in H₂ and C₂H₅OH with air [14]

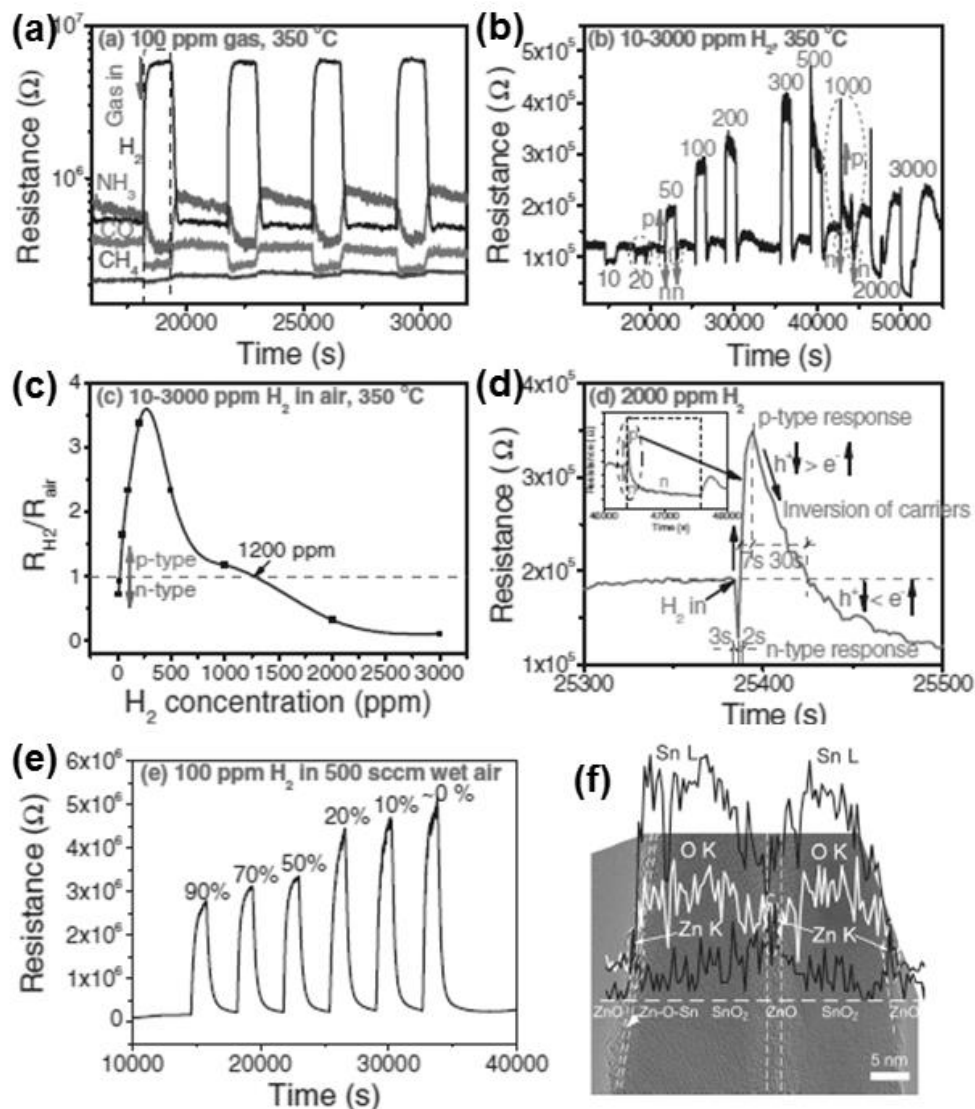


Figure 2.4. Sensing properties of the ZnO-modified SnO₂ nanorod sensors at 350 °C: (a) H₂ gas selectivity; (b) sequential response to H₂ concentrations; (c) n-p-n transition response; (d) the resistance change after 2000 ppm H₂ gas; (e) effect of the relative humidity; (f) nanoprobe EDX line-scan analysis [10]

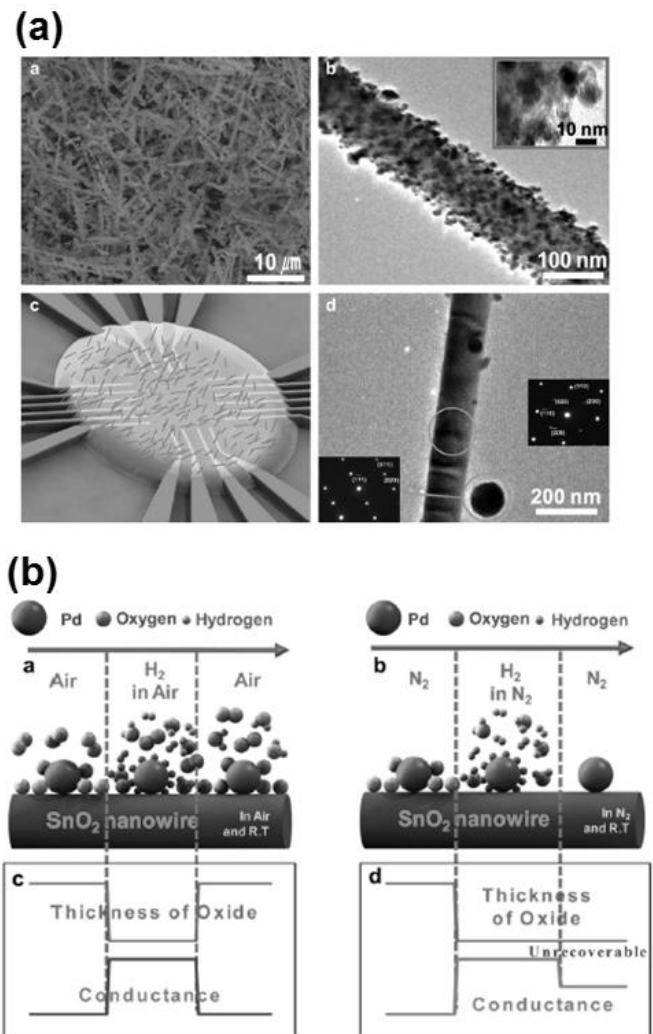


Figure 2.5. (a) SEM and TEM images of SnO₂ NWs and Sn NPs (b) The schematic images of the SnO₂ sensors competing one hydrogen cycle in air and in N₂ [11]

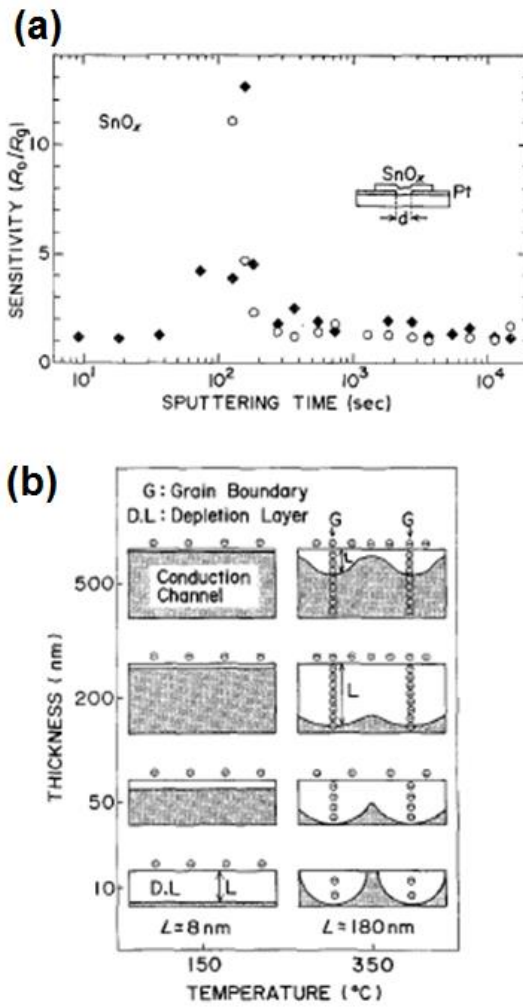


Figure 2.6. (a) H₂ gas sensitivity at 150 °C as a function of sputtering time. (b) A model illustrating the effect of film thickness on the depletion region. [23]

2.3. TiO₂ and TiO₂ based gas sensor for H₂ gas

TiO₂ (Anatase (A-TiO₂), Rutile (R-TiO₂) and Brookite (B-TiO₂)) have been studied for their photocatalytic [24], photo electrochemical [25] and gas sensors applications [26]. The difference in these three crystal structures can be attributed due to different physical, electrical, and chemical properties. At lower temperatures the A-TiO₂ and B-TiO₂ phases are more stable, but both will revert to the R-TiO₂ when subjected to high temperatures (915°C for the anatase phase and 750°C for the B-TiO₂ phase) [9]. Although R-TiO₂ is the most abundant of the three phases, many quarries and mines containing only the A-TiO₂ or B-TiO₂ form exist. The several features to distinguish the three phases are summarized on Table 2.2. The B-TiO₂ structure is more complicated and has a larger cell volume than the other two. The unit cell is composed of eight formula units of TiO₂ and is formed by edge sharing TiO₂ octahedra, similar to R-TiO₂ and A-TiO₂. However, the Ti-O bond lengths vary more than in the R-TiO₂ or A-TiO₂ due to orthorhombic structure [28]. B-TiO₂ showed higher photocatalytic activity, better photoinduced hydrophilicity, and higher volumetric energy density than the other phases, which suggest the potential applications as photocatalyst and anode for LIB but there are a few reports on its gas sensing properties [29-33].

The H₂ gas sensing properties of various TiO₂ structures are investigated and summarized in Table 2.3. In the case of TiO₂, most researchers are studied of H₂ gas sensing properties using N₂ balance gas due to chemical attraction of Oxygen and TiO₂. Because H₂ gas sensing properties using N₂ balance gas is not important in this thesis, the references are focused on H₂ gas sensing properties using air balance. Lu et al. [34] reported the high gas sensing properties of TiO₂ nanostructures using H₂/N₂ gas in Figure 2.7. In this case, measuring gas sensing properties are performed 500 °C which is relatively high temperature even though they used N₂ balance gas. Manippady et al. [36] exhibited extremely high gas response at room temperature using ultra-thin TiO₂ with Pd catalyst in Figure 2.8 but the sensing properties are measured at N₂ balance. Therefore, it seems that H₂/air gas sensor using TiO₂ is more difficult than SnO₂ and new gas sensing mechanism is needed for TiO₂ sensing at air balance. Several reports suggest the TiO₂ can be measured at H₂ gas in air balance. Lee et al. [37] fabricated low temperature (at near 100 °C) gas sensor using anatase TiO₂ nanotube which is metastable phase of TiO₂ in Figure 2.9. Chen et al. [39] and Shimizu et al. [42] suggested new gas sensing mechanism to explain the low temperature TiO₂ gas sensing properties in air balance, which is schottky contact effect enables the TiO₂ material to sense H₂ gas at low temperature.

Unit cell	Rutile TiO ₂	Anatase TiO ₂	Brookite TiO ₂
Form. Wt.	79.890	79.890	79.890
Z	2	4	8
Crystal System	Tetragonal	Tetragonal	Orthorhombic
Space Group	P42/mnm	I4 ₁ /amd	Pbca
Unit Cell			
a (Å)	4.5845	3.7842	9.18
b (Å)	4.5845	3.7842	5.447
c (Å)	2.9533	9.5146	5.145
Density (g/cm ³)	4.250	3.893	4.120
Band gap	3.03~3.37 eV	3.20~3.51 eV	3.11~3.56 eV

Table 2.2. Comparison of three TiO₂ phases (Rutile, Anatase, Brookite) [ICDD

21-1276 (Rutile), # 21-1272 (Anatase), # 29-1360 (Brookite)]

Materials	Synthesis	Detected Gas	Working Temp. (°C)	Detected Conc. (ppm)	S _{max}	Ref.
Rutile TiO ₂ (nanoporous)	Thermal oxidation	H ₂ /N ₂	500	500 (5~500)	90	[34]
Rutile TiO ₂ (thin film)	Sputter	H ₂ /N ₂	500	10000 (200~10000)	8*10 ³	[35]
Anatase-rutile TiO ₂ (nanotube)	Anodization	H ₂ /N ₂	290 (180~375)	1000 (100~1000)	10 ³	[12]
Anatase TiO ₂ (nanofilm)	ALD	H ₂ /N ₂	R.T.	1000 (5~1000)	10 ⁴	[36]
Anatase TiO ₂ (nanotube)	ALD using template	H ₂ /air	100 (75~175)	1000 (100~1000)	10 ²	[37]
Pt-rutile TiO ₂ (thin film)	Sol-gel	H ₂ /air	360 (330~500)	10000 (60~20000)	8*10 ²	[38]
Pt-anatase TiO ₂ (thin film)	Sol-gel	H ₂ /air	330 (330~500)	10000 (60~20000)	8*10 ⁴	[38]
Anatase-rutile TiO ₂ (nanotube)	Anodization	H ₂ /air	25	1000 (100~3000)	10 ⁴	[39]
Rutile TiO ₂ (nanoporous)	Anodization	H ₂ /air	225 (100~300)	10000 (1200~10000)	1.24	[40]
Anatase-rutile TiO ₂ (nanoporous)	Micro-arc oxidation	H ₂ /air	250 (100~300)	1000 (100~2000)	2.5	[41]
Rutile TiO ₂ (nanoporous)	Anodization	H ₂ /air	300 (250~400)	10000	49	[42]
Anatase-rich TiO ₂ (nanoporous)	Anodization	H ₂ /air	250 (250~400)	10000	408	[42]
Rutile TiO ₂ on FTO (thin film)	Hydrothermal	H ₂ /air	100 (25~100)	1000 (100~1000)	500	[43]
Anatase TiO ₂ on FTO (thin film)	Hydrothermal	H ₂ /air	100 (25~100)	1000 (100~1000)	50	[43]

Table 2.3. TiO₂ based H₂ gas sensors in the literature [12, 34-43]

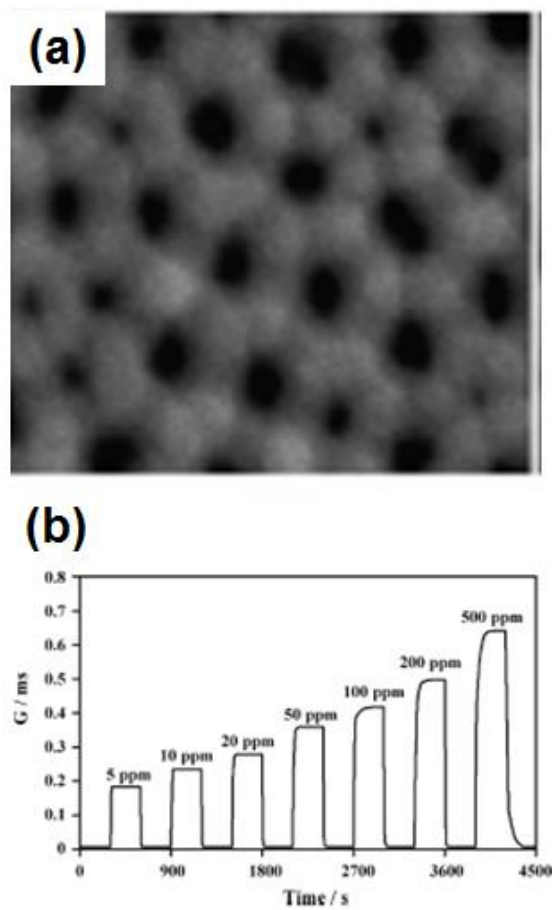


Figure 2.7. (a) The surface morphology of the titania nanoporous structure and
(b) H₂ gas response transient with various concentrations at 500 °C [34]

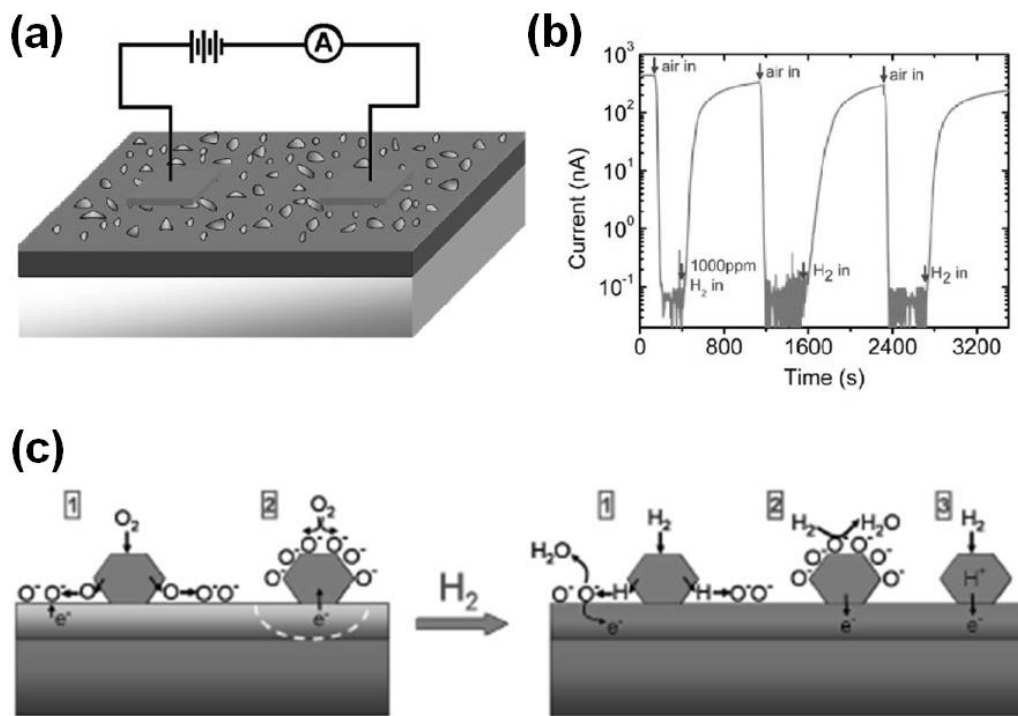


Figure 2.8. (a) A schematic illustration showing the configuration for measurement of sensing, (b) Hydrogen (1000 ppm in N₂)-induced electrical switching from the off to the on state with a current $\sim 0.3 \mu\text{A}$, and schematic depictions of the two major processes taking place at the Pd-TiO₂ surface (c) in air and (d) in H₂ [36]

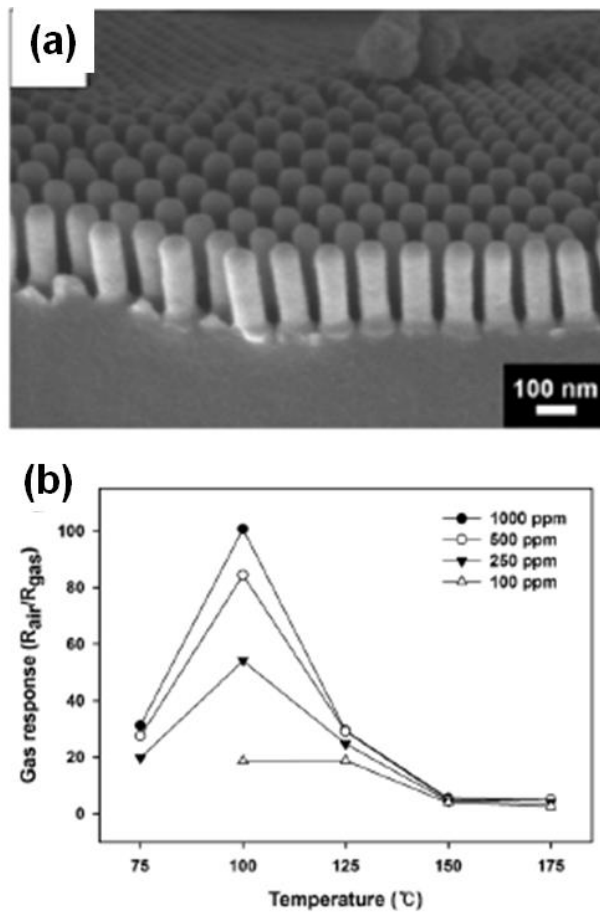


Figure 2.9. (a) Cross-sectional FE-SEM images of the TiO₂ nanotube arrays and (b) H₂ gas response of TiO₂ nanotubes with temperature variations [37]

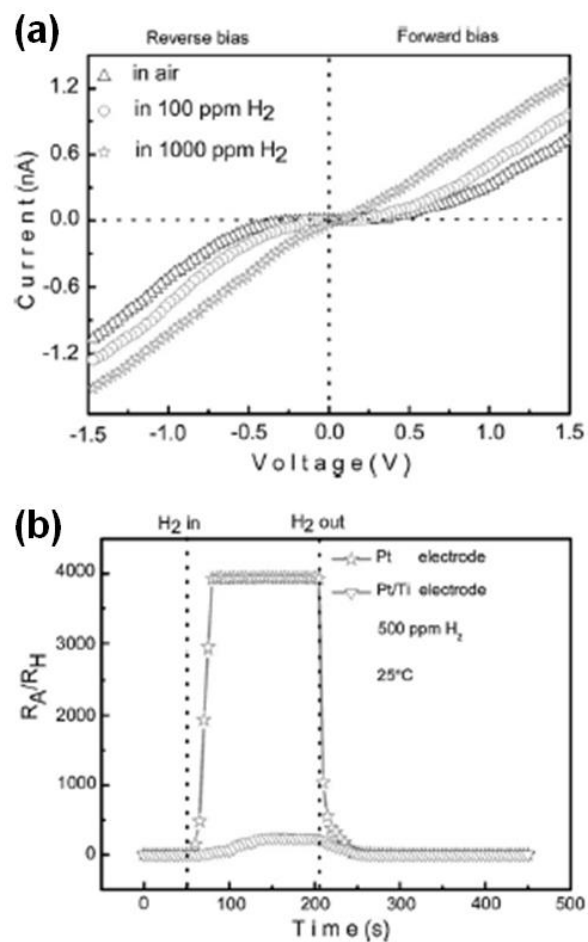


Figure 2.10. (a) I-V characteristics of the Pt/TiO₂ nanotube arrays sensors at room temperature in different ambient and (b) The response behavior of sensors with Pt or Pt/Ti electrodes [39]

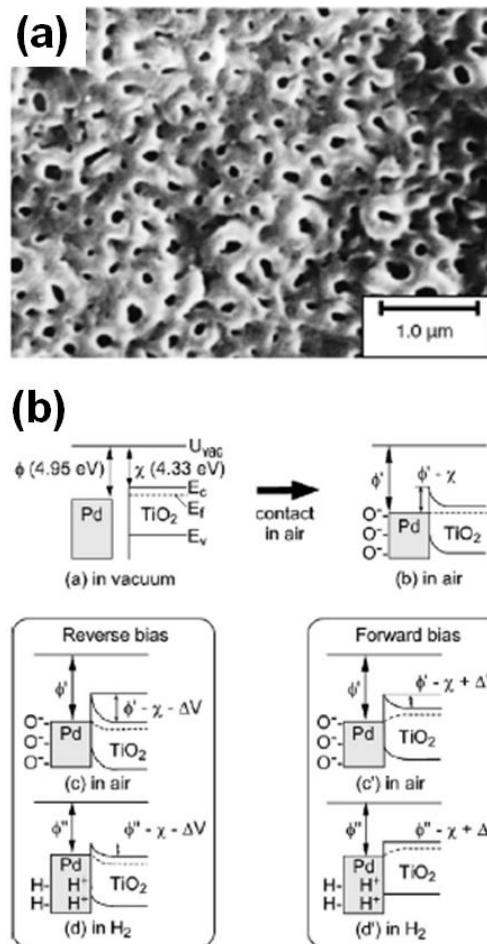


Figure 2.11. (a) SEM images of the surface of as-prepared A-TiO₂ nanotubes and (b) H₂ sensing mechanism based on variation in Schottky barrier height [42]

2.4. Epitaxial growth thin films and their gas sensing performance

As the study of gas sensing properties on nanostructures is increased, the sensing properties of surfaces with specific planes and phases have also been attributed from the many researchers. Egashira et al [44] measured H₂ gas sensing properties of single crystal whiskers grown with [101], [010], and [110] directions. The sensitivity was differed with crystallographic planes but the effect of crystallographic planes could not clearly explain due to different morphology of whiskers. Shimizu et al. [42] obtained different phases of TiO₂ thin films using micro arc oxidations and measured gas sensing properties. The gas sensing properties of TiO₂ thin films were changed with phase transition but they could not imply the effect of crystallographic phase on gas sensing properties due to different morphologies. The epitaxial growth of thin films is one of the solutions to solve these problems which could grow the different phases and orientations without significant morphology changes. Also, metastable phases and single crystal-like planes can be easily obtained due to lattice mismatch between thin film and single crystal. Moon et al. [35] and Choi et al. [45] deposited highly oriented TiO₂ and SnO₂ thin films on various sapphire substrates using sputtering methods, respectively. In the case of TiO₂, the highest gas sensing properties was exhibited at TiO₂ thin film oriented with

(200) plane which is grown on a-cut sapphire substrate as shown in Figure 2.13. On the other hand, (101) orientation in SnO₂ thin film showed the highest gas sensing properties. This difference can be considered due to inherent differences of materials or deposition conditions.

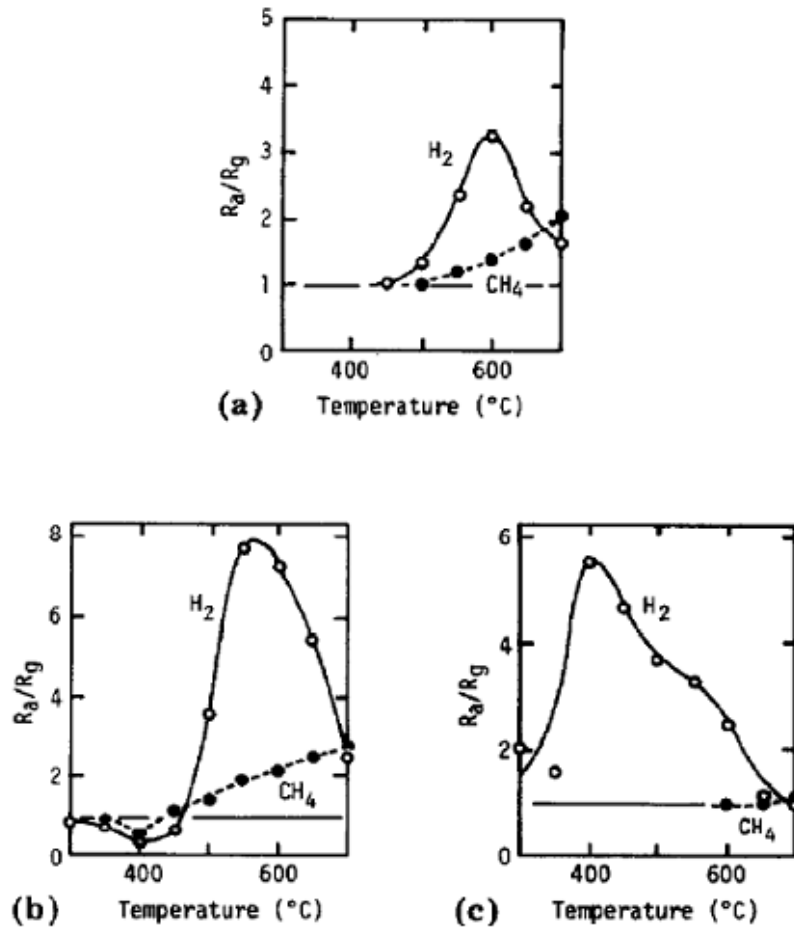


Figure 2.12. Typical gas-sensing characteristics of three types of SnO_2 whiskers,

(a) a $[101]$ whisker, (b) a $[010]$ whisker, (c) a $[110]$ whisker [44]

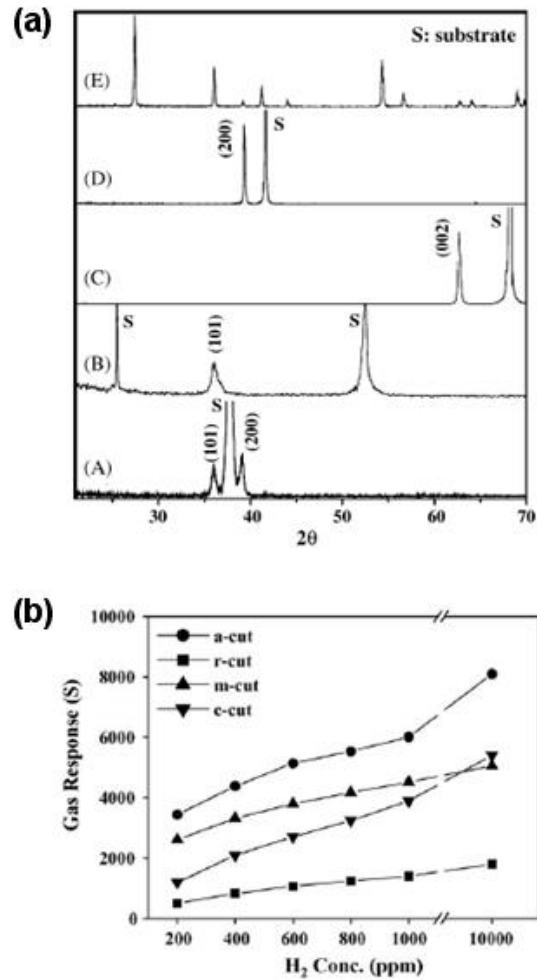


Figure 2.13. (a) XRD patterns of TiO₂ films grown on various sapphire substrates and (b) the sensitivity of TiO₂ thin films with concentration dependence [35]

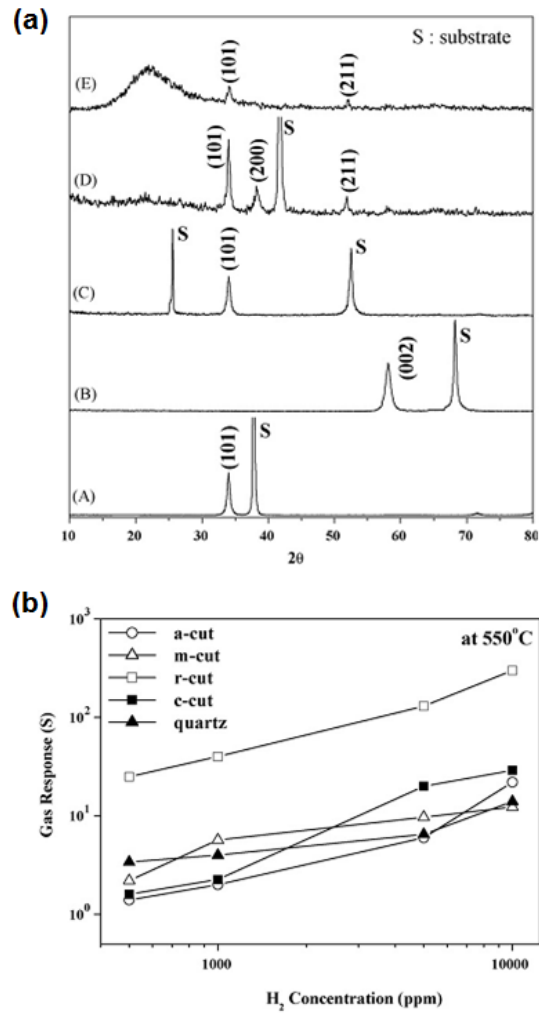


Figure 2.14. (a) XRD patterns of SnO₂ films grown on various sapphire substrates and (b) the sensitivity of TiO₂ thin films with concentration dependence [45]

2.5. Atomic layer deposition and epitaxial films

Atomic layer deposition (ALD) is a process for depositing thin films layers by alternating exposures of a surface to vapors of two chemical reactants. Figure 2.15 shows a schematic illustration of the ALD process. [77] The first reactant is introduced to react with the substrate surface. The reaction is allowed to proceed until the surface is saturated with chemisorbed species. Excess reactants and gaseous reaction products are then removed to avoid uncontrolled deposition. The second reactant is allowed to react with the surface species left behind by the first reactant, completing thereby an “atomic layer” on the surface, and leaving behind reactive sites for the first reactant. A purge completes the ALD reaction cycle. Reaction cycles are repeated to increase the film thickness. [78] Therefore, thickness is easily controlled by number of cycles and ALD has a great advantage to grow ultra-thin and uniform film with excellent step coverage. Moreover, due to self-limiting process controlled by surface reaction, many researches have been conducted to grow epitaxial thin film using ALD.

Epitaxy which refers single crystal formation on top of a crystalline substrate is arguably the most important phenomenon in semiconductor thin-film device technology. Epitaxial film is influenced by surface atomic arrangement of a substrate because mechanism of epitaxy is reducing the surface energy. Figure

2.16 shows the differences between homo and hetero epitaxy. When the epilayer and substrate crystal are identical, the lattice parameters are perfectly matched and there is no interfacial-bond straining. [79,80] In heteroepitaxy, the lattice parameters are necessarily unmatched, and depending on the extent of the mismatch, we can envision two distinct epitaxial regimes. As shown in figure 2.16, strained and relaxed thin films can be grown on substrates. Small lattice mismatch is universally desired and actually achieved in a number of important applications through careful composition control of the materials involved.

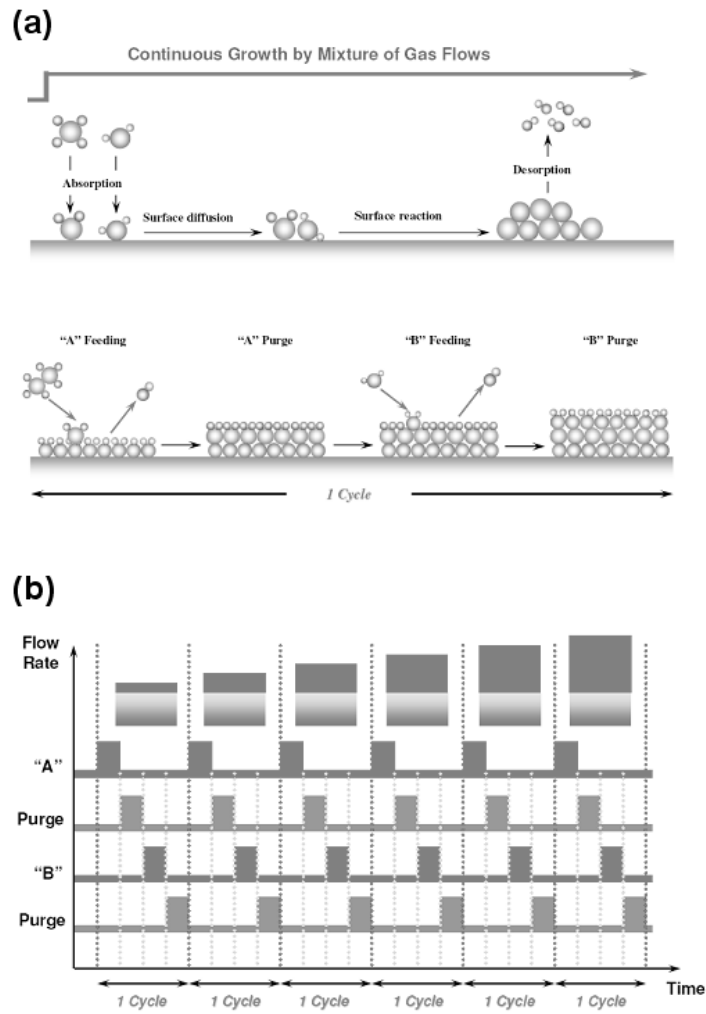


Figure 2.15. (a) Film growth model of CVD and ALD process, (b) layer by layer deposition with number of cycles by ALD [77]

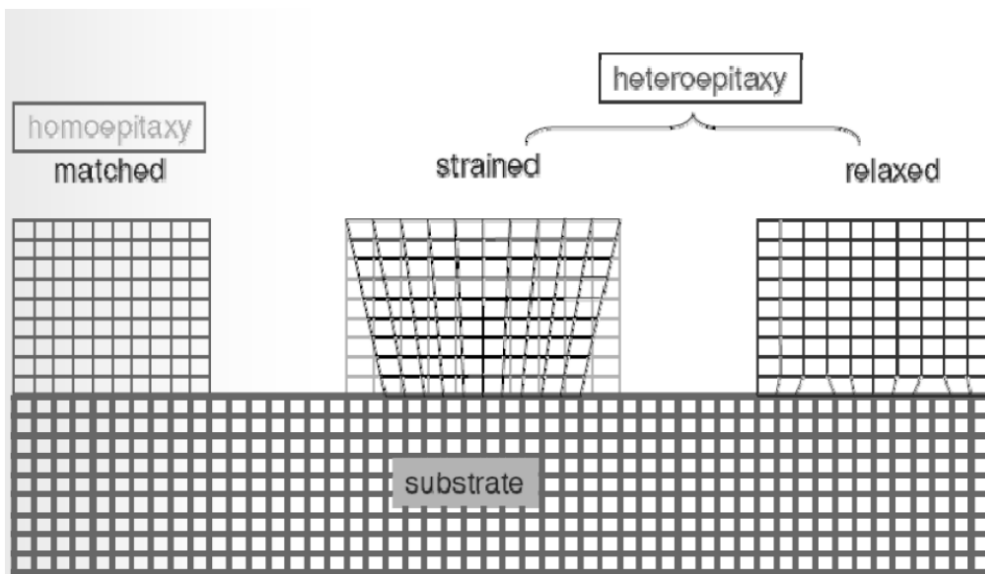


Figure 2.16. Model of epitaxial deposition [80]

Chapter 3. Experimental

3.1. ALD deposition and precursor

ALD is one of powerful deposition methods to produce uniform thin films with simple thickness control. In this experiment, Plasma enhanced atomic layer deposition (PEALD) have been explored to deviate from source selection and deposition temperature. Schematic diagram of PE-ALD system is described in figure 3.1. Processing chamber and load lock chamber are separately connected with dry pump and rotary pump, respectively. The maximum temperature, vacuum, and plasma power of processing chamber are up to 500 °C, 10^{-3} torr, and 600W. For the SnO₂ deposition, SnCl₄ [46,48,50,52-56] and SnI₄ [47-51] are commonly employed as Sn precursor, which requires a relatively high growth temperature (~600 °C) and yields a halide contamination. However, dibutyltindiacetate (DBTDA) ((CH₃CO₂)₂Sn [(CH₂)₃-CH₃]₂) was used to reduce deposition temperature and avoid a halide contamination. Titanium isopropoxide (TTIP) (Ti(OCH(CH₃)₂)₄) was used for the TiO₂ deposition, which is widely known as Ti precursor [57]. Schematic diagram of DBTDA and TTIP is represented in figure 3.2.

3.2. SnO₂ and TiO₂ deposition

SnO₂ thin films were deposited by plasma enhanced atomic layer deposition (PEALD) on single crystal TiO₂ substrates. The substrates used were (100), (001), (110), and (101) TiO₂. Dibutyltindiacetate (DBTDA) ((CH₃CO₂)₂Sn [(CH₂)₃-CH₃]₂) was used as Sn precursor, which was evaporated at 40 °C and transported to the deposition chamber by Ar (99.99%) gas of 50 sccm. The O₂ (99.99%) and Ar (99.99%) gases of 50 sccm were used as plasma and purge gases, respectively. The time sequence for source pulse, first purge, plasma pulse, and second purge was 3, 12, 12 and 12 s, respectively. The deposition was conducted with an rf power of 100 W at 240 mTorr for 1000 cycles. The substrate temperature during deposition was maintained at 300 °C. All the films were post-deposition annealed at 600 °C to enhance their crystallinity.

TiO₂ thin films were deposited on (110) YSZ substrate by PEALD. Titanium Isopropoxide (TTIP) (Ti(OCH(CH₃)₂)₄) was used as a Ti precursor, which was evaporated at room temperature and transported to the deposition chamber by 10 sccm Ar (99.99%). The 50 sccm O₂ (99.99%) and Ar (99.99%) were used as plasma and purge gases, respectively. The time sequence for the source pulse, first purge, O₂ pulse, O₂ plasma pulse, and second purge was 1, 12, 2, 10, and 12 s, respectively. The deposition was conducted with an rf power of 100 W at

220 mTorr for 1000 cycles, and the substrate temperature was maintained at 300 °C. Deposition conditions of SnO₂ and TiO₂ thin film are simply summarized in table 3.1.

3.3. Characterization

The thickness of the film was measured by X-ray reflectivity (XRR, Model X'Pert Pro, PANalytical, the Netherlands). The phases of the films were determined by X-ray diffraction (XRD, Model M18XHF-SRA, Mac Science, Japan) using Cu K α radiation ($\lambda=0.154$ nm) and the scan rate was 6°/min in the range from 10° to 80°. The in-plane orientation and out of-plane alignment were examined by X-ray pole figure (Model X'Pert Pro, PANalytical, the Netherlands), which were performed in Schulz reflection geometry by scanning the tilt angle of goniometer, χ (chi), in the range of 0~85° and the azimuthal angle, ϕ (phi), in the range of 0~360°, using a 5° step. The in-plane orientation relationships between SnO₂ films and TiO₂ substrates were further investigated by transmission electron microscopy (TEM). For this, cross-sectional specimens were prepared by mechanical polishing and subsequent ion milling at 4 kV. The samples were examined using JEM-3000F (JEOL, Japan) and TECNAI F20 (FEI, USA) TEM operating at 300 kV and 200 kV, respectively.

The surface morphology was examined by an atomic force microscope (AFM, Model SPA-400, Seiko, Japan). The chemical bonding information of the films was examined by X-ray photoelectron spectroscopy (XPS, Model AXIS, KRATOS) with a Mg K α radiation (1253.6 eV). The core level XPS spectra for O1s and Sn3d were measured, and energy calibration was achieved by setting the hydrocarbon C1s line at 284.6 eV.

3.4. Gas sensor measurement

Schematic illustration of gas sensors and measuring systems are showed in figure 3.3 (a) and (b), respectively. For the gas sensing measurements, a pair of comb-like Pt electrodes was formed by sputtering on the SnO $_2$ or TiO $_2$ films through a mask and Au lead wires were attached to them using Ag paste. Thereafter, all the sensors were annealed at 600 °C for 1 h in order to make the electrical contact between Ag paste and Au lead wires. The H $_2$ sensing properties were determined by measuring the changes in electric resistance between sample gas (100~1,000 ppm H $_2$, ethanol, NH $_3$, and CO balanced with air) and pure air at 300~500 °C. The electrical resistance was measured using a multimeter (2000 multimeter, Keithley) and a sourcemeter (2400, Keithley). The magnitude of the gas response (S) was defined as the ratio (R_o/R_g) of the

resistance in air (R_o) to that in a sample gas (R_g). Water bubbling system was used with dry air carrier gas to confirm H₂ selectivity toward humidity. When dry air (250 sccm) and wet air (250 sccm) were mixed at same ratio, the relative humidity was 50 % at room temperature and it can be changed as absolute humidity which is about 12 g/m³.

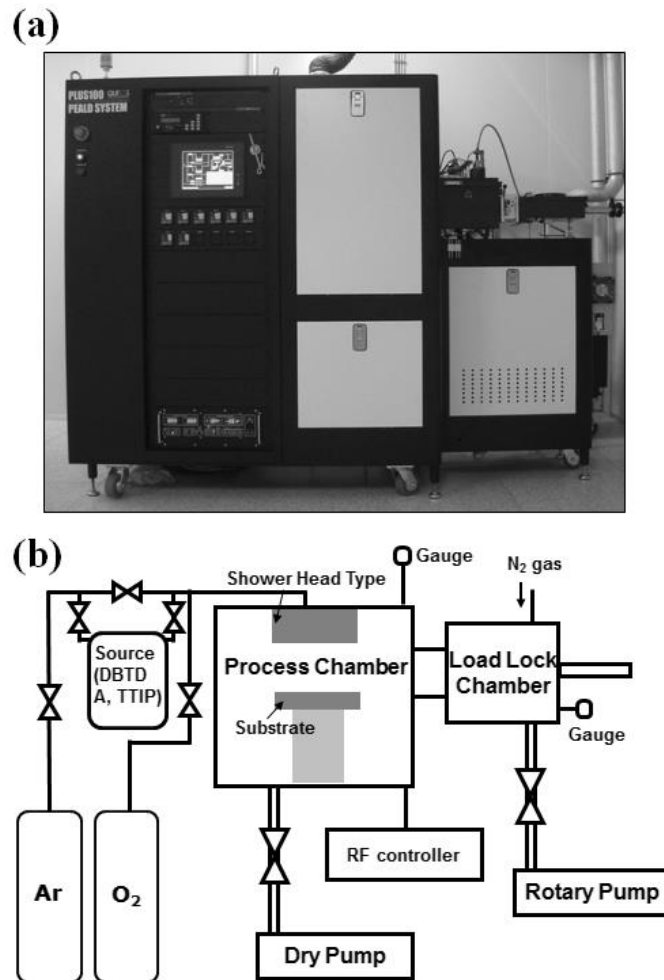


Figure 3.1. (a) PE-ALD system of this experiment and (b) schematic diagram of PE-ALD system

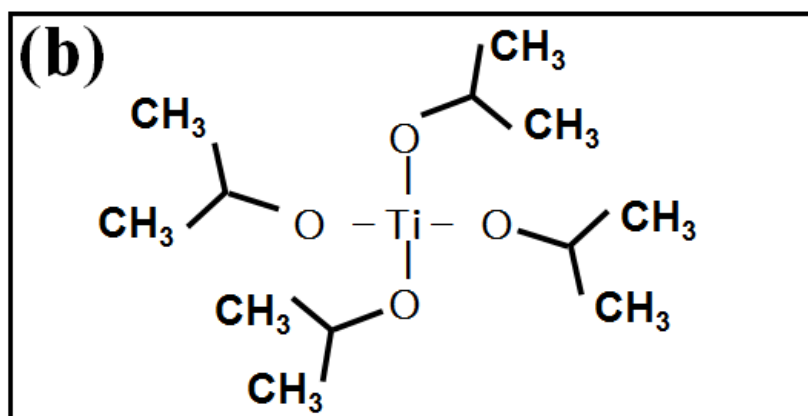
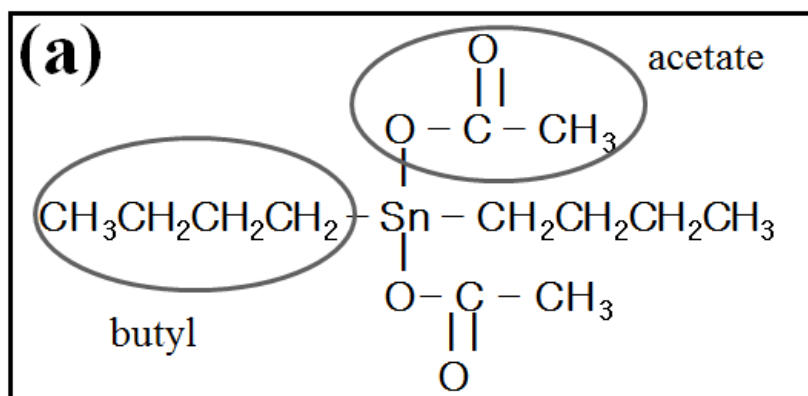


Figure 3.2. Molecular structures of (a) Dibutyl tin Diacetate (DBTDA) as Sn precursor and (b) Titanium Tetraisopropoxide (TTIP) as Ti precursor

	SnO ₂	TiO ₂
Substrate temperature	300 °C	300 °C
Canister temperature	40 °C	R.T.
Wall temperature	100 °C	100 °C
Line temperature	70 °C	70 °C
Working pressure	240 mTorr	240 mTorr
RF power	100 W	100 W
Deposition cycle	1000 cycle	1000 cycle
Deposition time (sec) (Source, first purge, O ₂ plasma, second purge)	3, 12, 12, 12	1, 12, 12(2), 12

Table 3.1. Deposition conditions of SnO₂ and TiO₂ thin films

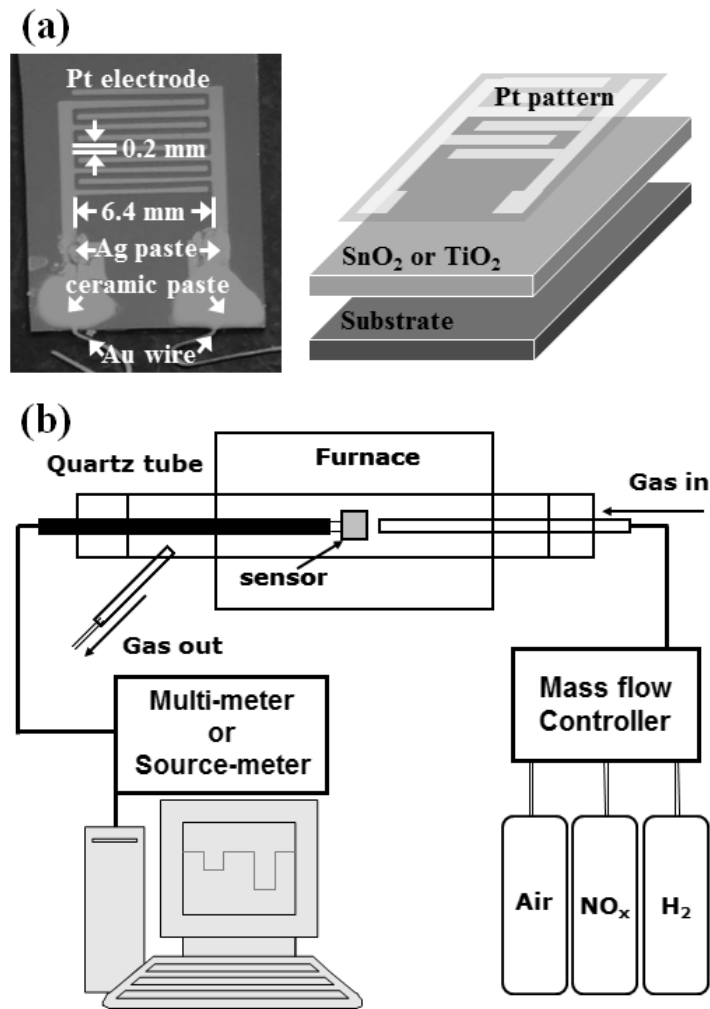


Figure 3.3. (a) Electrode structure of thin film gas sensor and (b) Schematic diagram of gas sensor measurement system [58]

Chapter 4. Results and discussions

4.1. Oriented SnO₂ thin films grown on TiO₂ single crystals

4.1.1. Structure characterization

XRD patterns of the SnO₂ films deposited on the various TiO₂ substrates are shown in Figure 4.1. Both as-deposited and annealed (at 600 °C) films were crystalline and highly oriented. SnO₂ and TiO₂ have a tetragonal rutile structure with lattice constants of $a=4.738$, $c=3.187$ and $a=4.593$, $c=2.959$ Å, respectively. Thus, all the diffraction peaks were indexed based on the rutile structure. SnO₂ peaks were located at lower 2θ compared to the corresponding TiO₂ peaks due to its larger lattice constants. Only (200), (002), (110), and (101) diffraction peaks were observed in the films deposited on (100), (001), (110), and (101) TiO₂ substrates, respectively, indicating that SnO₂ films were highly oriented and epitaxially grown on the TiO₂ substrates.

The in-plane orientation relationships of SnO₂ films on TiO₂ substrates were investigated by X-ray pole figure. Figure 4.2 shows the {101} pole figures of SnO₂ films along with those of the TiO₂ substrates. In the pole figure of SnO₂ film on (100) TiO₂ substrate (Figure 4.2(a)), two strong reflections were

observed with eight additional weak reflections marked as T1 and T2 (one T1 and one T2 were overlapped with the strong reflections). Two strong peaks originate from the {101} family of planes ((101), (10 $\bar{1}$)) consistent with TiO₂ substrate, and eight additional peaks can be attributed to the {101} planar defects formed in the film to relax the misfit-induced large biaxial compressive stress, reported previously [59]. On the other hand, the {101} pole figures of SnO₂ films deposited on (001), (110), and (101) TiO₂ substrates exactly match with those of TiO₂ substrates without additional reflections. Based on these observations, it was confirmed that SnO₂ films were epitaxially grown on these substrates without noticeable planar defects and out of- and in-plane orientations exactly followed the TiO₂ substrate orientations.

The in-plane epitaxial relationships were further investigated by TEM. Figure 4.3(a) is a typical low magnification TEM image for the cross-section of SnO₂ film deposited on TiO₂ substrate. All the films had the flat surface and were approximately 90 nm thick after 1000 ALD cycles. Selected area electron diffraction (SAED) patterns for films and substrates exactly matched each other confirming the epitaxial growth of SnO₂ films on TiO₂ substrates consistent with the results of X-ray pole figure. High resolution TEM images (Figure 4.3(b)-(e)) indicates that the SnO₂ films had the well-defined and atomistically sharp interfaces, which was marked by arrows. The HRTEM image for the film

deposited on (100) TiO₂ substrate (Figure 4.3(b)), viewed along the SnO₂ [010] direction, exhibited the sharp (101) and ($\bar{1}01$) lattice fringes in both film and substrate. However, the SnO₂ film showed the high-density dislocations and wedge-shaped planar defects existing on two crystallographically equivalent (101) and ($\bar{1}01$) planes consistent with the previous report [59]. These {101} planar defects yielded the additional peaks in the {101} pole figure (Figure 4.2(a)) and some modulated strips in the fast Fourier transformation (FFT) pattern of SnO₂ film (inset of Figure 4.3(b)). The lattice mismatch along [001] direction is 8% and the planar defects are believed to be formed to relax the misfit-induced large biaxial compressive stress in the film as suggested by Wakabayashi et al. [59]. In case of (001) TiO₂ substrate (Figure 4.3(c)), (101) and ($\bar{1}01$) lattice fringes were also clearly seen in both film and substrate, but only a few dislocations were observed across the interface due to the smaller lattice mismatch along [100] direction (3%). The HRTEM image for the film deposited on (110) TiO₂ substrate exhibited the sharp (110) and (001) lattice fringes parallel and perpendicular to the interface (Figure 4.3(d)). Similarly, the (101) and (010) lattice fringes were observed parallel and perpendicular to the interface in the film deposited on (101) TiO₂ (Fig. 4.3(e)). Both SnO₂ films showed a few dislocations.

The surface morphologies of the SnO₂ films examined by AFM are shown in

Figure 4.4. The obtained SnO₂ films were smooth and featureless irrespective of the substrate orientations. The root-mean-square (RMS) values of the surface roughness were in the range of 0.9~1.8 nm (scan area 2 μm × 2 μm). A very fine surface feature developed in the film deposited on (110) TiO₂, possibly because (110) SnO₂ is the most stable plane. On the other hand, a rather rough surface was obtained in the film grown on (001) TiO₂, which appears to be related to the high surface energy of (001) SnO₂ surface [60,61]. However, the determined surface areas were not significantly different.

The chemical states of Sn and O in SnO₂ films were investigated by XPS and the core level Sn3d and O1s spectra were shown in Figure 4.5. All films exhibited a Sn3d doublet with a Sn3d_{5/2} at ~486.5 eV and a single peak of O1s at ~530.4 eV, which are in good agreement with the values for the lattice tin and oxygen of SnO₂, respectively [62]. Thus, the deposited films are close to the stoichiometric SnO₂ irrespective of the substrate orientations.

4.1.2. Gas sensing properties

SnO₂ is an n-type semiconductor with a band gap of 3.6 eV. Its electrical conduction results from oxygen vacancies and interstitial tin atoms that act as donors. When the SnO₂ film is exposed to the air O₂ is adsorbed onto the

surface of film, $1/2\text{O}_2 (\text{g})+2\text{e}^- \rightarrow 2\text{O}^- (\text{ad})$. The oxygen atoms pick up the electrons from the conduction band which introduces a depletion region on the surface having a thickness d (debye length). The presence of an electrical double layer on the surface increases the potential barrier for the electronic conduction. If reducing gases, such as H_2 , EtOH , NH_3 , etc, are induced, the oxygen atoms are desorbed by reaction with reducing gas and release the electrons to the conduction band. As a result, the depth of the electrical double layer decreases, causing a decrease in the height of the potential barrier for the electronic conduction. Then, the magnitude of gas response (S) is determined as the ratio of its resistance in air to that in a sample gas. A typical response transient of SnO_2 film grown on TiO_2 substrate toward H_2 gas balanced with air is shown in Figure 4.6. In the previous study of polycrystalline SnO_2 films deposited on the sapphire substrates by rf magnetron sputtering [45], the sensor measurements were carried out at $550\text{ }^\circ\text{C}$ due to the high resistance of films. However, the sensing temperature was greatly reduced in the present SnO_2 films with the same electrode geometry, possibly due to the single crystal-like nature of the epitaxial films, and thus, stable and reversible sensing signals were obtained at temperatures as low as $300\text{ }^\circ\text{C}$. Upon injecting a sample gas (1000 ppm H_2/air), the resistance decreased rapidly by more than two orders of magnitude. The recovery was rather slow but the sensing signal was quite stable

and reversible. The concentration dependence of each film was investigated in the range of 100~1,000 ppm H₂/air and the magnitude of the gas response increased almost linearly with increasing H₂ concentration (log (gas response) vs. log (concentration)).

The determined magnitude of gas response (*S*) toward 1000 ppm H₂/air is shown in Figure 4.7 as a function of sensing temperature. As expected, the magnitude of gas response varied with sensing temperature and substrate orientation (or resulting film orientation). A rather randomly oriented SnO₂ thin film deposited on quartz substrate showed the gas response of ~150 at 400 °C, which was close to an average value of all epitaxial films. Most of maximum magnitude of gas response was observed at the intermediate temperature (400 °C), which is a characteristic behavior of semiconductor-type gas sensor [9,63]. The highest H₂ gas response of ~380 was obtained in the (101) SnO₂ film deposited on (101) TiO₂ substrate at 400 °C, which is comparable to or even higher than the best values reported previously [45,64-67]. The higher gas response in (101) oriented SnO₂ film has been reported previously and the chemical composition and surface state played an important role for determining the sensing performance [45]. All the films in this study had similar microstructural characteristics (thickness, surface area, roughness) and chemical composition, which appear to little affect the gas sensing properties.

Thus, the electrical resistances of the SnO₂ film sensors in a sample gas (R_g) and in air (R_o) were re-examined as shown in Figure 4.8. For all the sensors, the resistances in the sample gas (1000 ppm H₂/air) decreased with increasing temperature from 300 to 400 °C and then remained constant. In contrast, the resistances in air exhibited a distinct feature for the (101) SnO₂ film sensor, i.e. the resistances of the other film sensors were relatively constant with temperature, but the (101) SnO₂ film sensor showed a sharp increase of resistance at 400 °C, which resulted in the highest gas response at that temperature. At least three sensors per each film were fabricated and tested for H₂ gas sensing properties. The obtained results were consistent except a slight fluctuation of resistance. Therefore, it is believed that the higher H₂ gas sensitivity in (101) oriented film is an inherent property of SnO₂ and it is closely related to the different temperature dependence of resistance.

The sensing properties of SnO₂ film sensors toward ethanol, NH₃, and CO gases were also investigated (Figure 4.9). The magnitude of gas response for NH₃ and CO gases was an order of magnitude lower than that for H₂ gas at all the temperatures investigated and the orientation and temperature dependence of gas response was slightly different. The magnitude of gas response for ethanol was slightly lower than that for H₂ gas, but the orientation and temperature dependence of gas response was very similar to those of H₂. Thus, the present

epitaxial SnO₂ film sensors showed a high selectivity for H₂ against NH₃ or CO gas, but they exhibited a poor selectivity against ethanol.

This part was based on my SCI journal which was already published. [83]

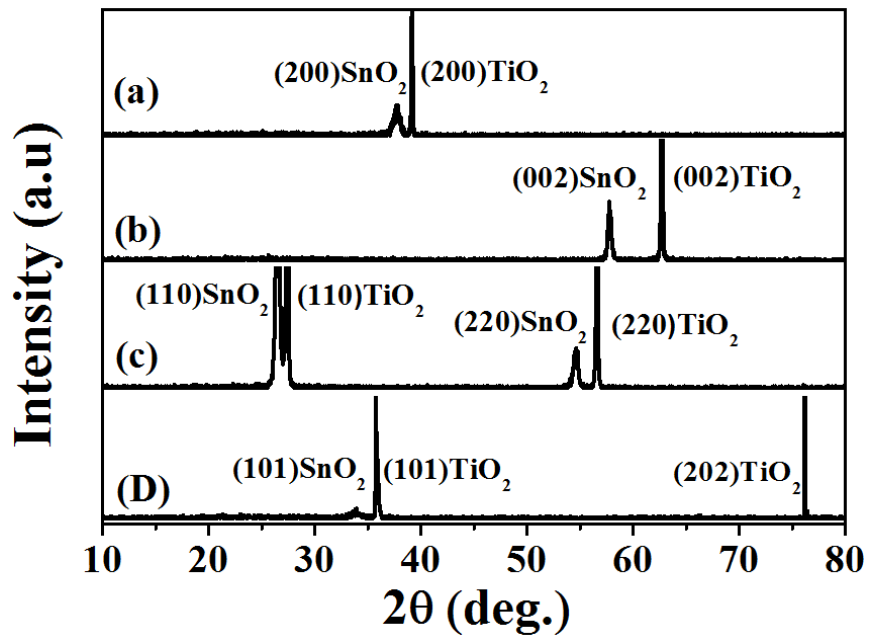


Figure 4.1. XRD patterns of SnO₂ thin films deposited on (a) (100), (b) (001), (c) (110), and (d) (101) TiO₂ substrates.

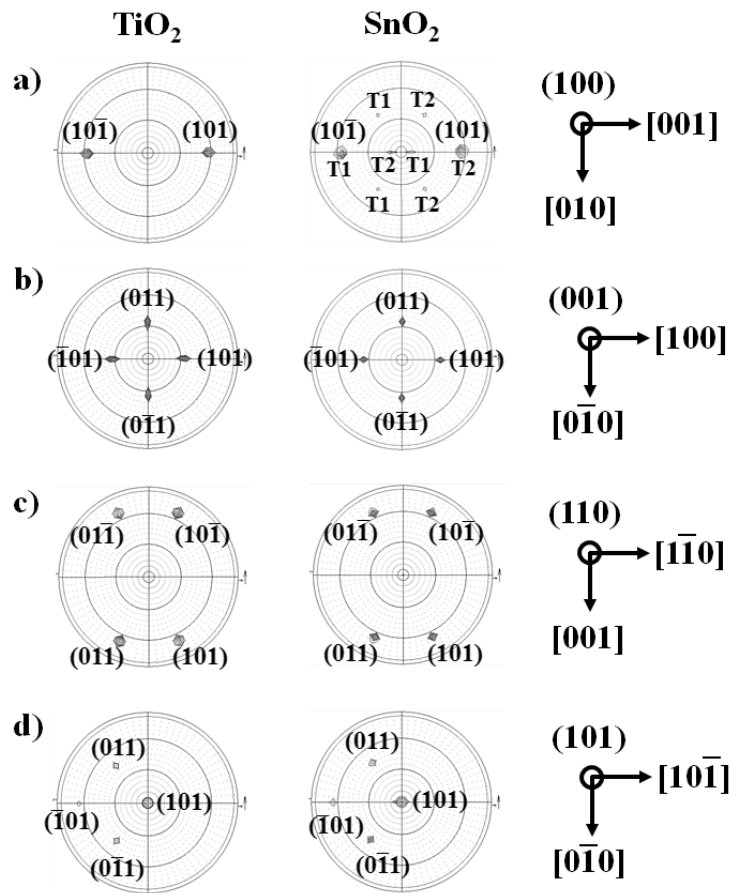


Figure 4.2. $\{101\}$ pole figures of the SnO₂ deposited on the (a) (100), (b) (001), (c) (110), and (d) (101) TiO₂ substrates.

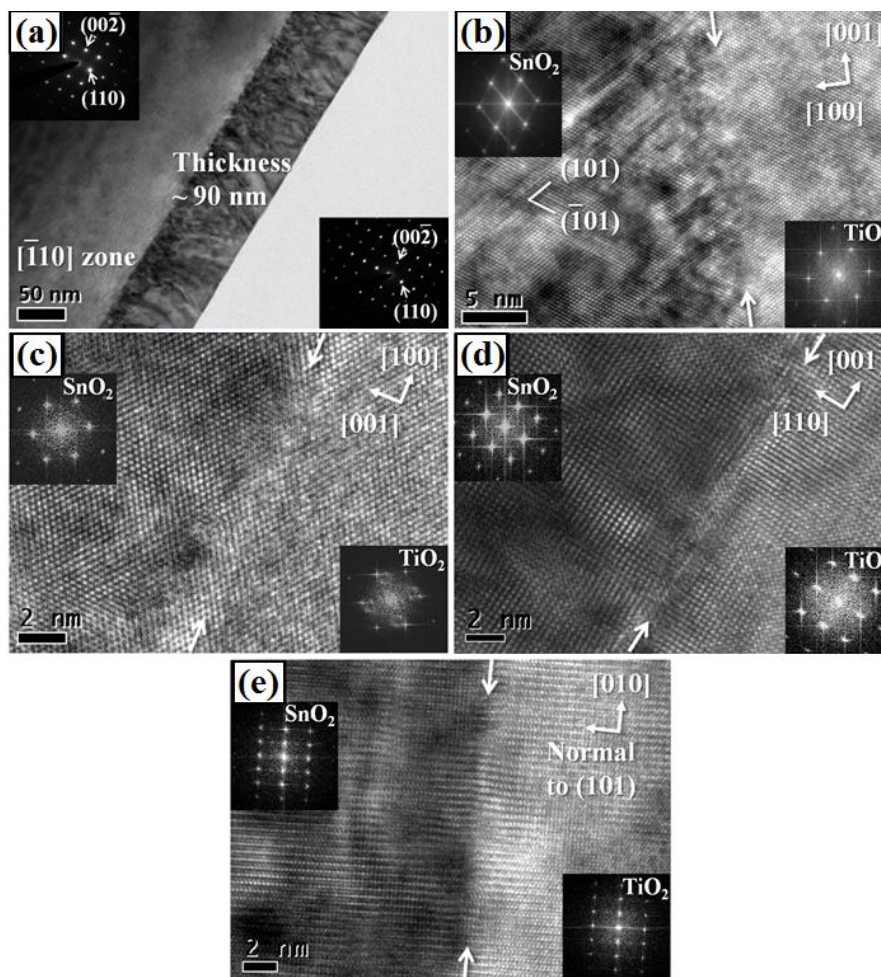


Figure 4.3. (a) Low magnification TEM image of (110) SnO₂ film grown on (110) TiO₂ substrate and HRTEM images of SnO₂/TiO₂ interfaces for the films grown on (b) (100), (c) (001), (d) (110), and (e) (101) TiO₂ substrates.

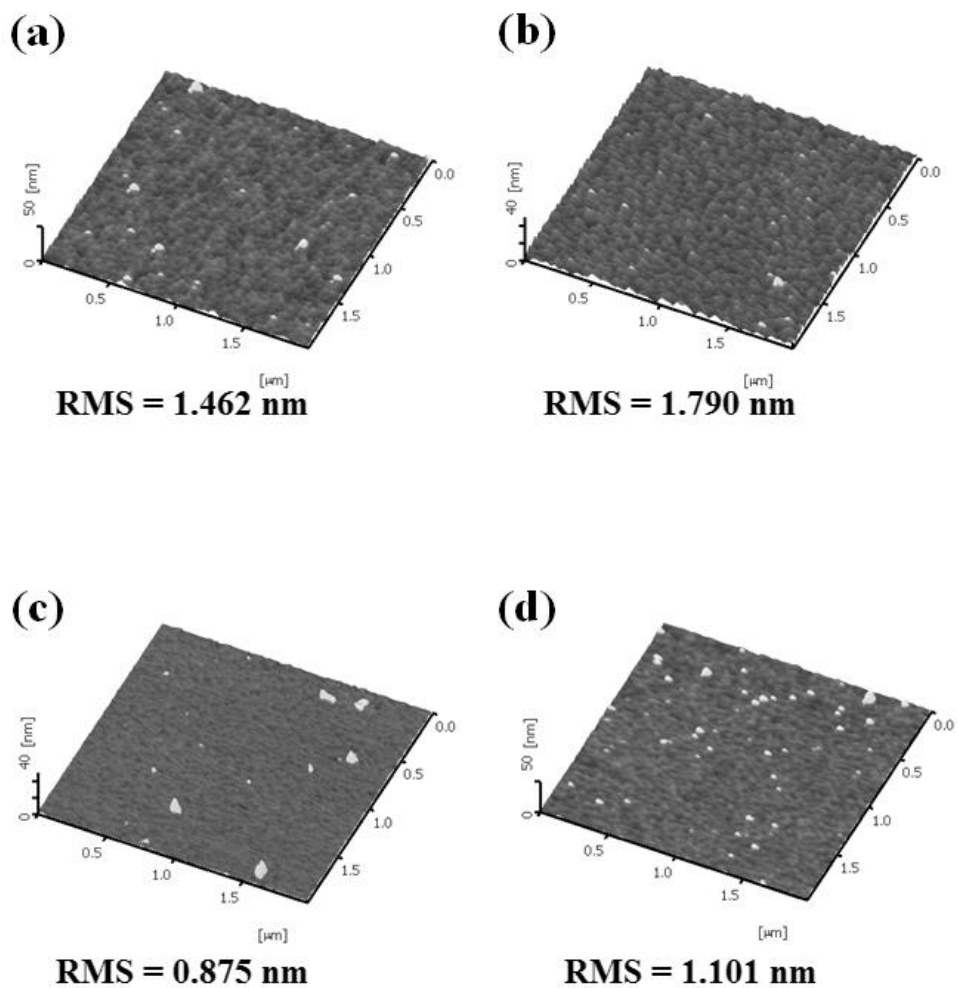


Figure 4.4. AFM topographic images of the SnO_2 films grown on (a) (100), (b) (001), (c) (110), and (d) (101) TiO_2 substrates.

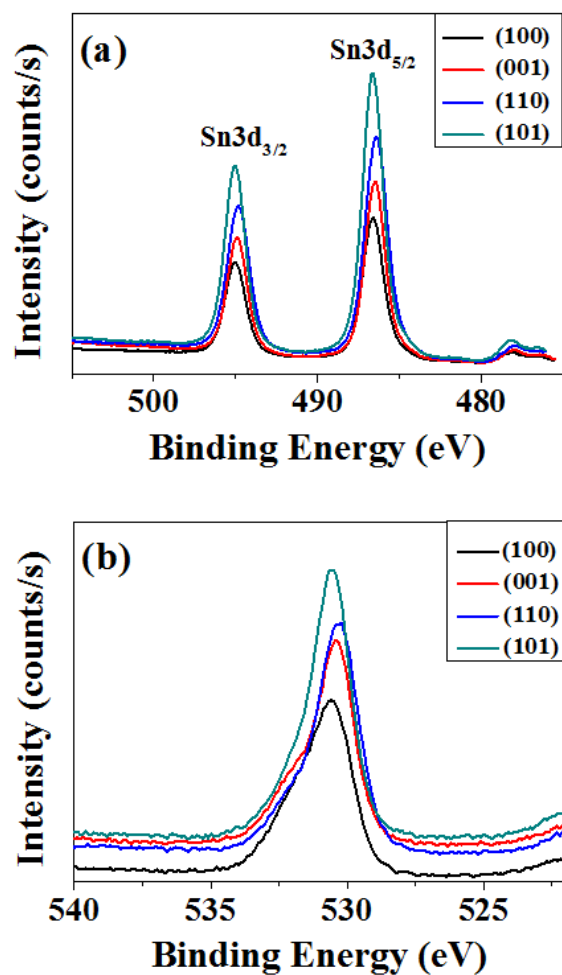


Figure 4.5. (a) Sn3d and (b) O1s core level XPS spectra of the SnO₂ films deposited on (100), (001), (110), and (101) TiO₂ substrates.

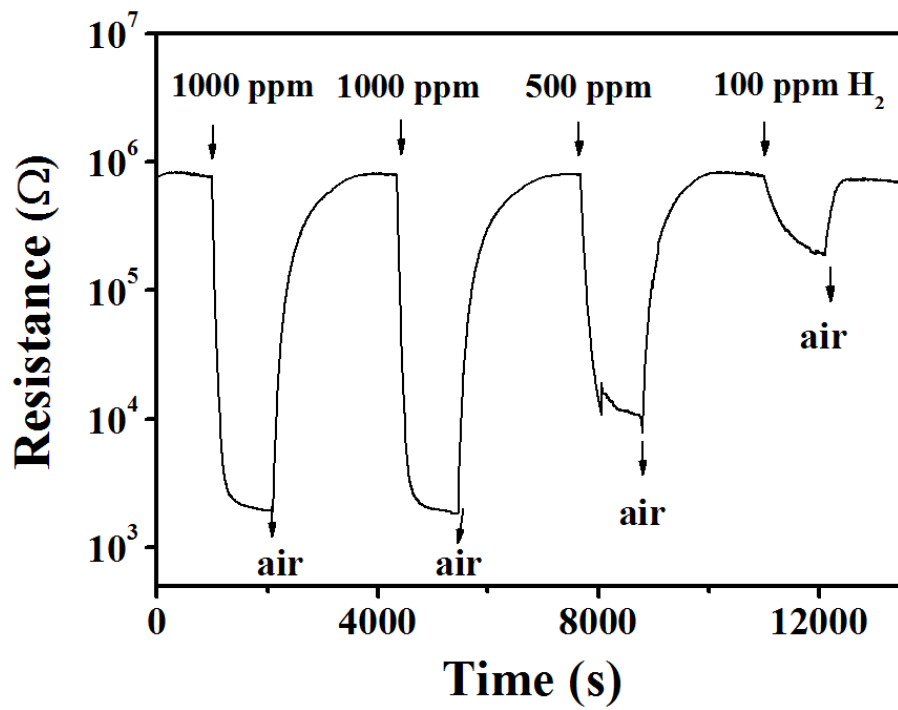


Figure 4.6. Response transient of the SnO_2 films grown on (101) TiO_2 substrate toward H_2 gas (100–1000 ppm) measured at 400 °C.

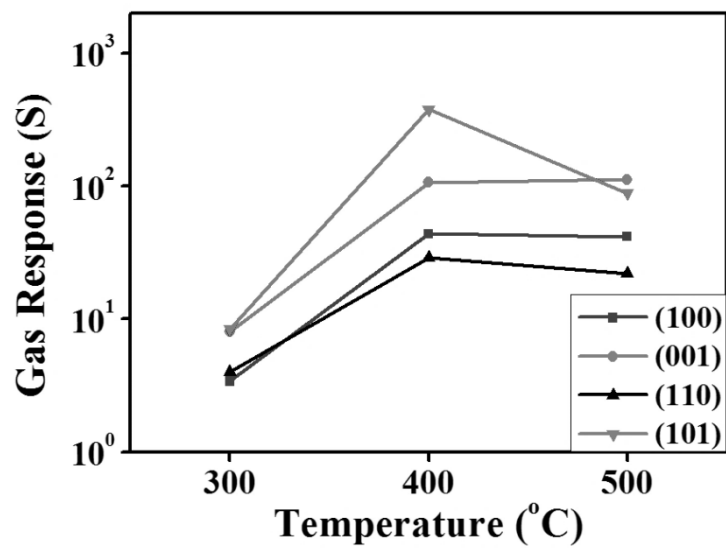


Figure 4.7. Magnitude of gas response (S) toward 1000 ppm H₂/air in the films grown on (100), (001), (110), and (101) TiO₂ substrates as a function of sensing temperature.

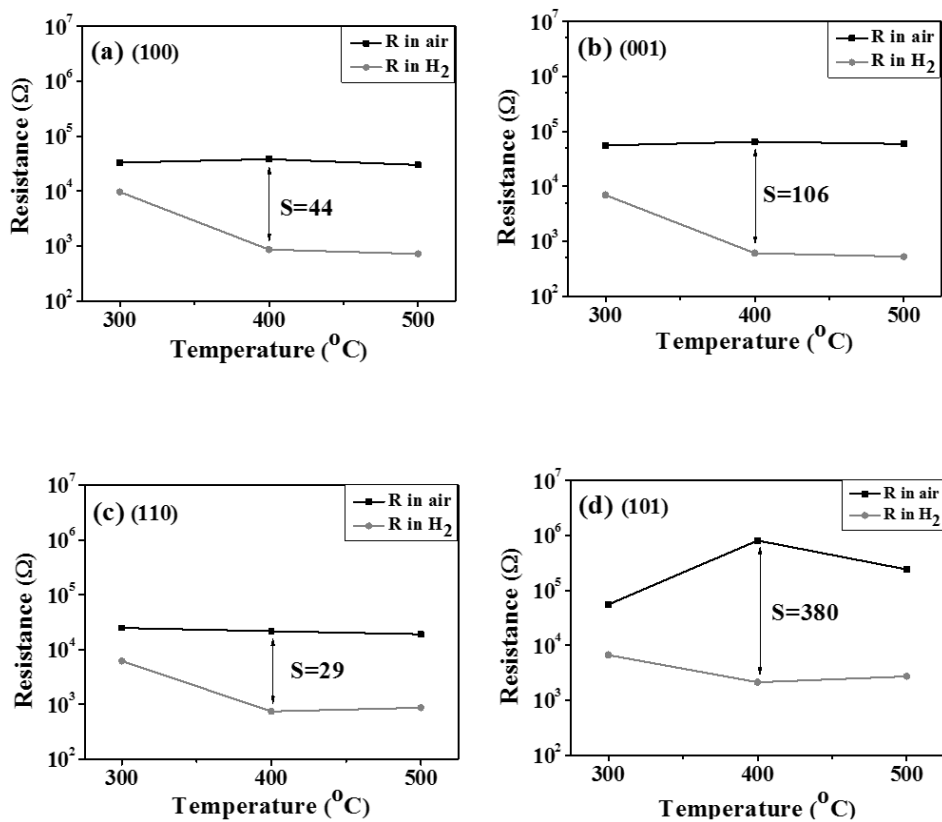


Figure 4.8. Electrical resistance of the SnO_2 films in air and in 1000 ppm H_2/air as a function of sensing temperature deposited on (a) (100), (b) (001), (c) (110), and (d) (101) TiO_2 substrates.

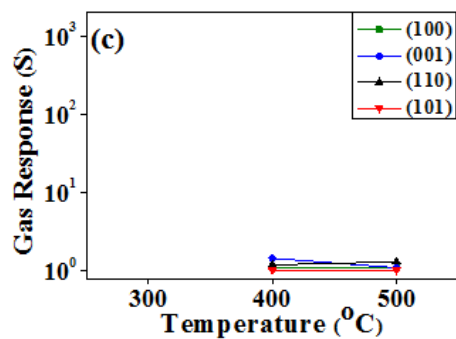
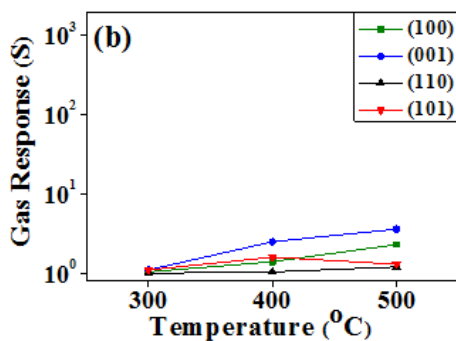
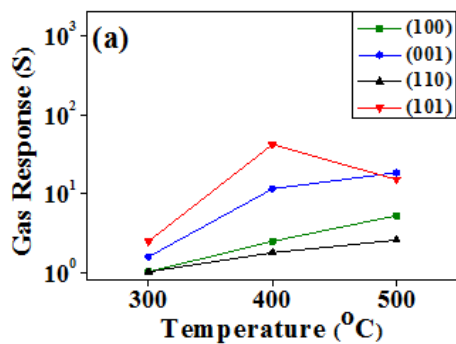


Figure 4.9. Magnitude of gas response (S) toward 1000 ppm (a) ethanol, (b) NH₃, and (c) CO gases in the films deposited on (100), (001), (110), and (101) TiO₂ substrates as a function of sensing temperature.

4.2. Brookite TiO₂ thin film epitaxially grown on YSZ substrates

4.2.1. Structure characterization

The surface morphology of as-deposited film observed by AFM is shown in Figure 4.10 (a). The surface was relatively rough, exhibiting an elongated granular morphology. The root-mean-square (RMS) value of the surface roughness was 4 nm (scan area 1 $\mu\text{m} \times 1 \mu\text{m}$). The surface roughness was much improved when the substrate temperature was reduced to 100 °C (see Figure 4.10 (b) and (c)), but the crystallinity of the film decreased and thus, the substrate temperature was fixed to be 300 °C. The cross-sectional TEM image showed that the film thickness was ~80 nm (Figure 4.11), which was also confirmed by X-ray reflectivity (XRR). The film density determined by XRR was ~3.95 g/cm³, which was ~96 % of the theoretical density for brookite TiO₂ (4.13 g/cm³) [68]. The chemical states of Ti and O in as-deposited film were determined by XPS (see Figure 4.12). The film exhibited a Ti2p doublet with a Ti2p_{3/2} at 458.5 eV and a single peak of O1s at 530.05 eV, which match well with those for stoichiometric TiO₂ [62]. The XRD patterns of as-deposited film at 300 °C and annealed film are shown in Figure 4.13 (a). The deposited film was crystalline and only one peak was observed except the peak for YSZ substrate. The diffraction peak of film was indexed as (120) based on the

orthorhombic brookite (B-TiO₂, ICDD #29-1360). Thus, highly oriented (120) B-TiO₂ was grown on the (110) YSZ substrate. The substrate temperature affected the structure of the TiO₂ film on YSZ. When the substrate temperature increased to 500 °C, B-TiO₂ was changed to the mixed phases of B-TiO₂ and R-TiO₂ (see Figure 4.13 (b), log scale of intensity). In order to investigate the thermal stability, as-deposited film (300 °C) was annealed at 700 °C for 1 h, but no phase change was observed. Thus, the obtained B-TiO₂ film was thermally stable, which is believed to be due to the constraint from the substrate (epitaxial relationship). It is known that a brookite phase is transformed into an anatase or rutile phase at over 500 °C [69,70]. In addition, Raman spectroscopy was employed to further confirm the brookite phase [29,71], but the signals were very weak and overlapped with those of the YSZ substrate and thus, the phase identification was not possible. The in-plane orientation relationship between the film and substrate was investigated using an X-ray pole figure. The {120} pole figure of B-TiO₂ film is shown in Figure 4.14, where the substrate orientation is indicated next to the pole figure. The reflections from {120} family planes ((120) and ($\bar{1}20$)) appeared with additional contributions from 180° rotation marked as T1 in the figure. The appearance of 180° rotated reflections is due to the twofold symmetry of (110) YSZ and the non-symmetry of (120) B-TiO₂, implying two variants in the film. The 180° rotated

contribution has been frequently observed in epitaxially grown TiO₂ films [72]. In the pole figure, the reflections from the {111} family of planes were detected because the diffraction angles of (111) and (120) were very close (25.689° vs 25.339°). The in-plane relationship was determined to be $[2\bar{1}0]_{B-TiO_2} // [1\bar{1}0]_{YSZ}$ and $[001]_{B-TiO_2} // [001]_{YSZ}$.

To confirm the epitaxial growth, B-TiO₂ film was further examined by high resolution transmission electron microscopy (HRTEM). Figures 4.15 (a) and (b) show the cross sectional HRTEM images of TiO₂ film along with fast Fourier transformation (FFT) patterns from the film and substrate. The interfaces between the film and substrate were well defined and atomistically sharp. The HRTEM image, viewed along the $[00\bar{1}]$ direction of YSZ (Figure 4.15 (a)), exhibited a (120) lattice fringe parallel to the interface and a $(\bar{1}20)$ lattice fringe with an angle of 99.8° to the interface. The FFT patterns confirmed that the (120) B-TiO₂ film grew epitaxially on the (110) YSZ substrate with the orientation relationship of $[2\bar{1}0]_{B-TiO_2} // [1\bar{1}0]_{YSZ}$ and $[001]_{B-TiO_2} // [001]_{YSZ}$. In the some parts of the film, 180° rotated (120) B-TiO₂ film was observed with (120) B-TiO₂, which was consistent with the X-ray pole figure (see Figure 4.16). The HRTEM image, viewed along the $[1\bar{1}0]$ direction of YSZ (Figure 4.15 (b)), exhibited (120) and $(00\bar{2})$ lattice fringes parallel and perpendicular to the

interface, respectively, and the obtained in-plane orientation relationship between film and substrate was also confirmed. Based on the determined epitaxial relationship, the in-plane atomic configurations of (120) B-TiO₂ and (110) YSZ are schematically shown in Figure 4.15 (c). The estimated lattice mismatch in each direction was -1.91 and 0.06 %, respectively, based on the reported lattice parameters of $a(\text{TiO}_2)=5.455$, $b(\text{TiO}_2)=9.181$, $c(\text{TiO}_2)=5.142$, (B-TiO₂, ICDD #29-1360) and $a(\text{YSZ})=5.139 \text{ \AA}$ (YSZ, ICDD #30-1468). The lattice mismatches in both directions are quite small and thus, (120) B-TiO₂ can be heteroepitaxially grown on (110) YSZ substrate.

Figure 4.17 shows the optical transmittance spectra of as-deposited B-TiO₂ film on (110) YSZ and bare (110) YSZ substrate as a function of wavelength in the range of 200 ~ 800 nm. The average transmittance in the visible region (400~700 nm) was about 70 %, which was slightly lower than that of the bare YSZ substrate. The film showed a strong absorption in the UV region (250~400 nm). From the plots of $(\alpha E)^2$ vs. photon energy (E), the optical band gap energy (E_g) was determined by extrapolating the straight line portion of the plot. The determined E_g was ~3.29 eV, which was close to the reported value for the B-TiO₂ nanorod and still higher than that for rutile (3.0 eV) and anatase (3.2 eV) [73,74].

4.2.2. Gas sensing properties

Figure 4.18 (a) shows a typical response transient of the B-TiO₂ film sensor toward H₂ gas balanced with air measured at 150 °C. The H₂ concentration was varied from 1000 to 100 ppm in discrete steps. The sensor exhibited a decrease in resistance upon injecting the H₂ gas and recovered to the original level after removing the H₂ gas. The sensing signal was stable and reproducible. The magnitude of the gas response (S) was defined as the ratio (R_{air}/R_{gas}) of the resistance in air (R_{air}) to that in a sample gas (R_{gas}). It was determined to be ~150 at 1000 ppm H₂/air and decreased with decreasing H₂ concentration. The determined magnitude of gas response (S) toward 1000 ppm H₂/air is shown in Figure 4.18 (b) as a function of sensing temperature. For comparison, the gas response of (200) R-TiO₂ film coated on a-cut (110) sapphire in the same deposition conditions was included (see Figure 4.19). The B-TiO₂ film sensor detected the H₂ gas even at room temperature and the highest H₂ gas response was obtained at 150 °C, which is a characteristic behavior of semiconductor-type gas sensors [9]. The magnitude of gas response obtained at room temperature was lower than the best value reported in the TiO₂ nanotube-array sensor [39], but the present B-TiO₂ film sensor was one of a few TiO₂-based gas sensors, which can detect the H₂ gas in air balance. As mentioned earlier, the

brookite phase was stable up to 700 °C and thus, the B-TiO₂ film sensor is expected to be more thermally stable than the other nanostructure-based TiO₂ sensors. The optimum working temperature of 150 °C in B-TiO₂ film sensor was much lower than the previously reported rutile TiO₂ film sensors and comparable to that of the A-TiO₂ nanotube sensor [35,37,38]. On the other hand, the (200) R-TiO₂ film sensor showed the H₂ gas response above 150 °C and the magnitude of gas response was comparatively low. At 150 °C, the magnitude of gas response was two orders of magnitude lower than that of B-TiO₂ sensor.

To further investigate the low temperature H₂ detection of B-TiO₂ sensor, the temperature dependence of the electrical resistance is shown in Figure 4.18 (c). The electrical resistance of R-TiO₂ sensor was beyond the detection limit of the equipment ($> 10^{10} \Omega$) and thus, the sensor measurement was possible above 150 °C and the resistance change with H₂ exposure was small resulting in the lower magnitude of gas response. However, in B-TiO₂ sensor, both R_{air} and R_{gas} were within the detection limit even at room temperature and the sensor stably responded to H₂ gas at low temperatures. R_{air} was relatively constant with temperature whereas R_{gas} decreased with increasing temperature from room temperature to 150 °C and then increased with a further increase of temperature, which resulted in the highest gas response at 150 °C. Consequently, B-TiO₂ film had the lower resistance and higher resistance change with H₂ exposure or

adsorption/desorption of oxygen species than R-TiO₂ film, which lead to the superior H₂ gas detection at low temperature. We have also deposited the TiO₂ films on (100) and (111) YSZ and examined the H₂ gas sensing properties. The film deposited (100) YSZ was oriented anatase-brookite mixture consistent with previous report [75] whereas the film deposited on (111) YSZ was non-oriented anatase-brookite mixture (see Figure 4.20). The magnitude of H₂ gas response in TiO₂ film deposited on (100) YSZ was comparable to that of B-TiO₂ and the film deposited on (111) YSZ exhibited the very low H₂ gas response (see Figure 4.21). At this stage, it is difficult to relate the H₂ gas sensing performance to the crystallographic orientation in B-TiO₂ film because of mixed phases. Further study is highly required. The sensing properties of B-TiO₂ film sensor toward CO, ethanol (EtOH), and NH₃ gases were also investigated (see Figure 4.22). The magnitude of gas response for CO, EtOH, and NH₃ was an order of magnitude lower than that for H₂ gas. Thus, B-TiO₂ film sensor showed a high selectivity for H₂ against CO, EtOH, and NH₃, particularly at low temperature. The high selectivity for H₂ against other gases of TiO₂ has been explained by two possible factors. The first one is dissociated hydrogen atoms are used for chemisorption on the film surface besides desorption of oxygen species [12]. Chemisorbed hydrogen acts as a surface state and a partial charge transfer takes place from hydrogen to the conduction band of TiO₂. This creates an electron

accumulation layer on the film surface that enhances its electrical conductance.

Another factor is the catalytic reaction of the Pt electrode. It is confirmed that the selective hydrogen dissociation can occur on platinum surfaces and these dissociated hydrogen atoms spill onto the film surface [12,37].

This part was based on my SCI journal which was already published. [84]

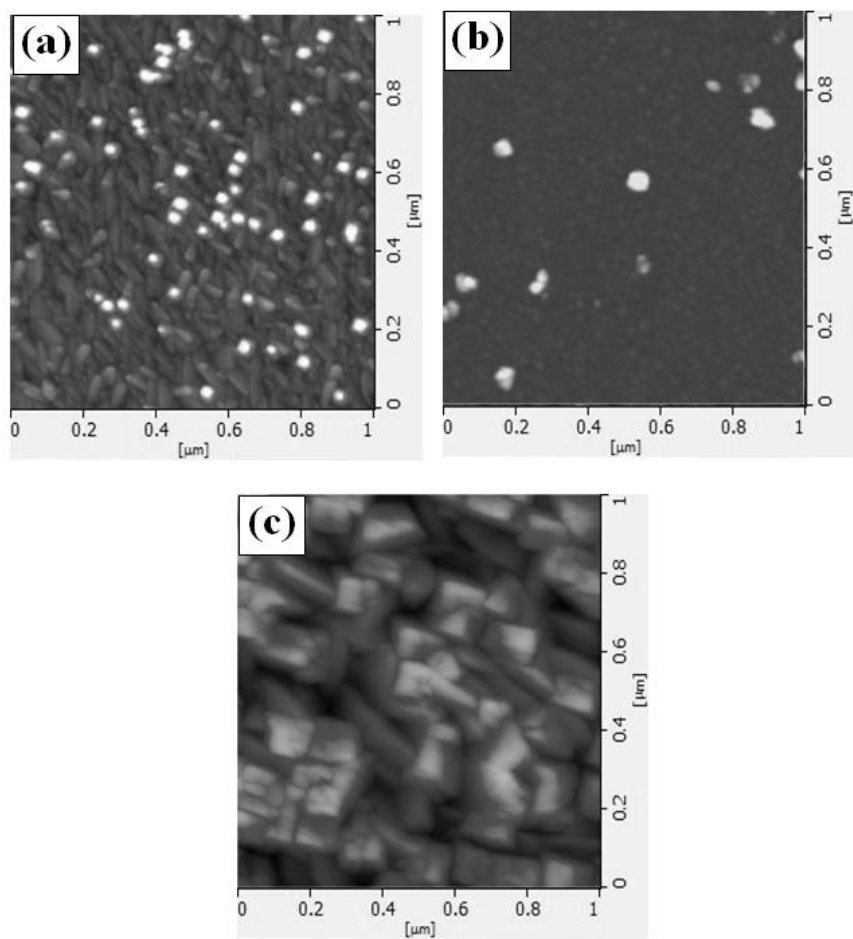


Figure 4.10. Surface morphology of as-deposited TiO₂ film grown on (110) YSZ at the substrate temperature of (a) 100, (b) 300, and (c) 500 °C,

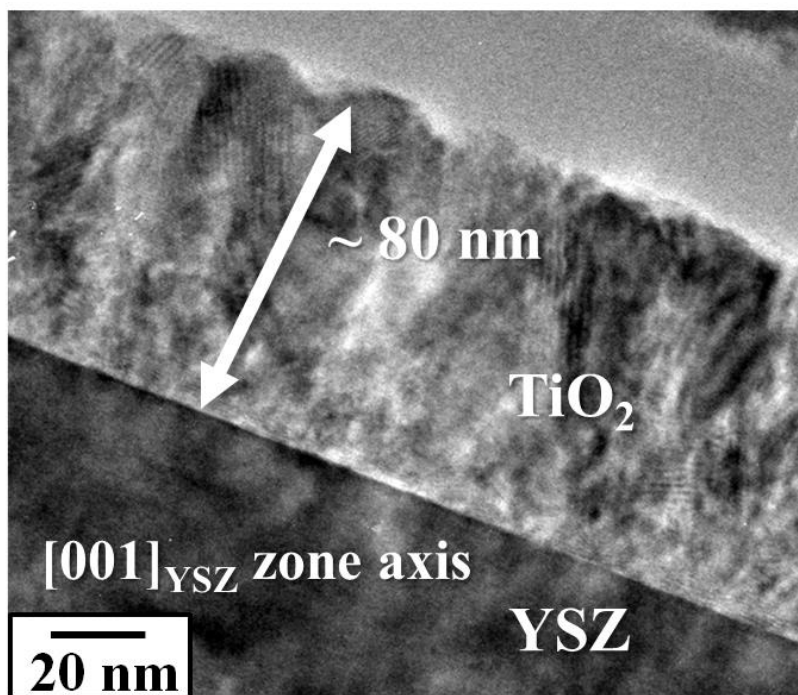


Figure 4.11. Cross-sectional TEM image of as-deposited TiO₂ film grown on (110) YSZ.

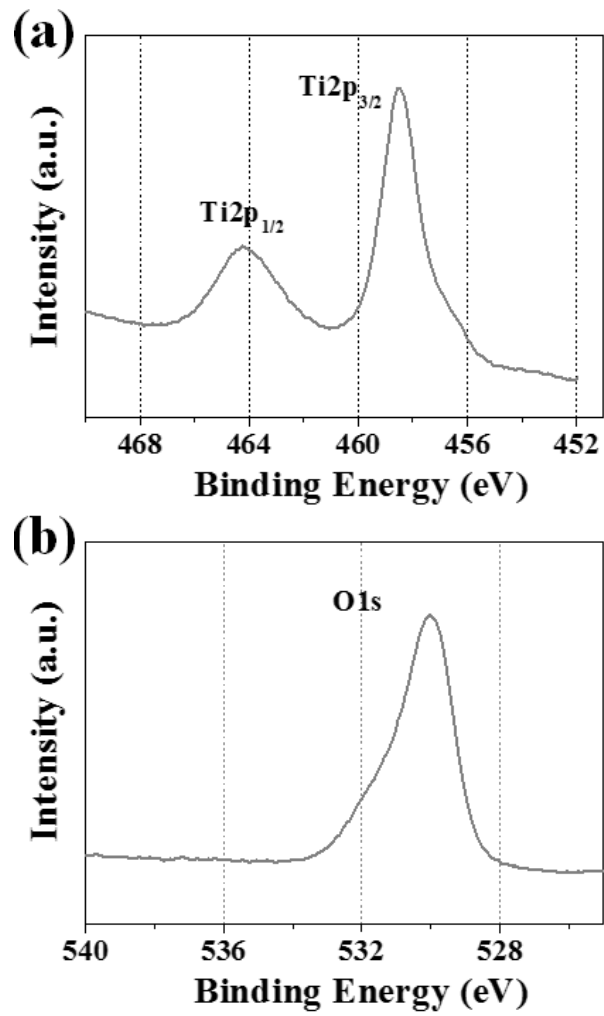


Figure 4.12. (a) Ti2p and (b) O1s core level XPS spectra of as-deposited TiO₂ film grown on (110) YSZ.

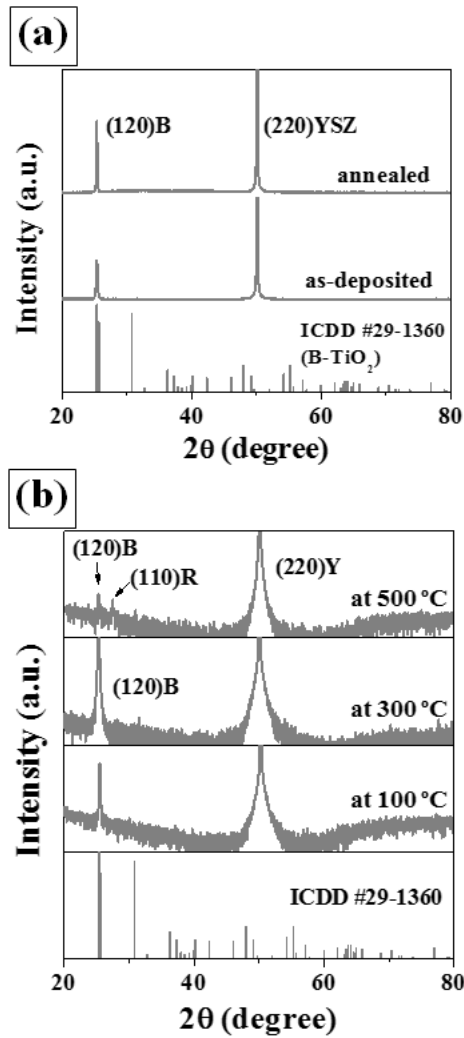


Figure 4.13. XRD patterns of (a) as-deposited and annealed (at 700 °C for 1 h) TiO₂ films grown on (110) YSZ at 300 °C and (b) TiO₂ films with deposition temperature variations. The reference is the standard diffraction pattern of brookite TiO₂ (ICDD #29-1360).

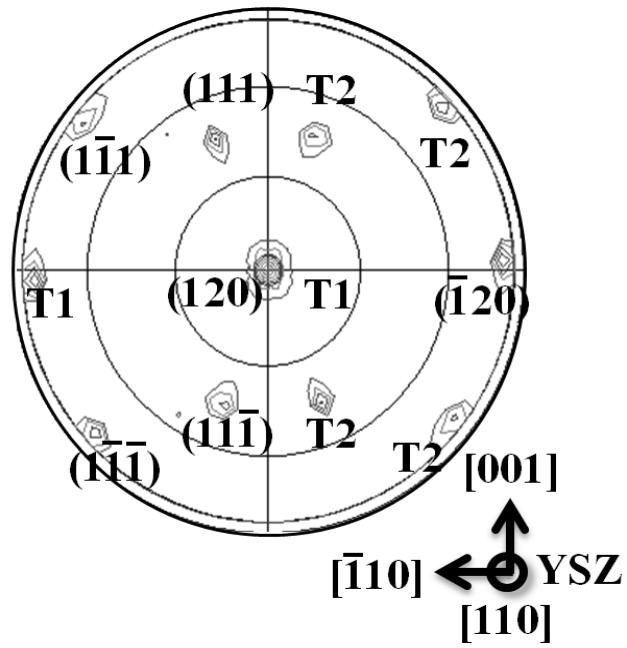


Figure 4.14. {120} pole figure of as-deposited TiO₂ film grown on (110) YSZ.

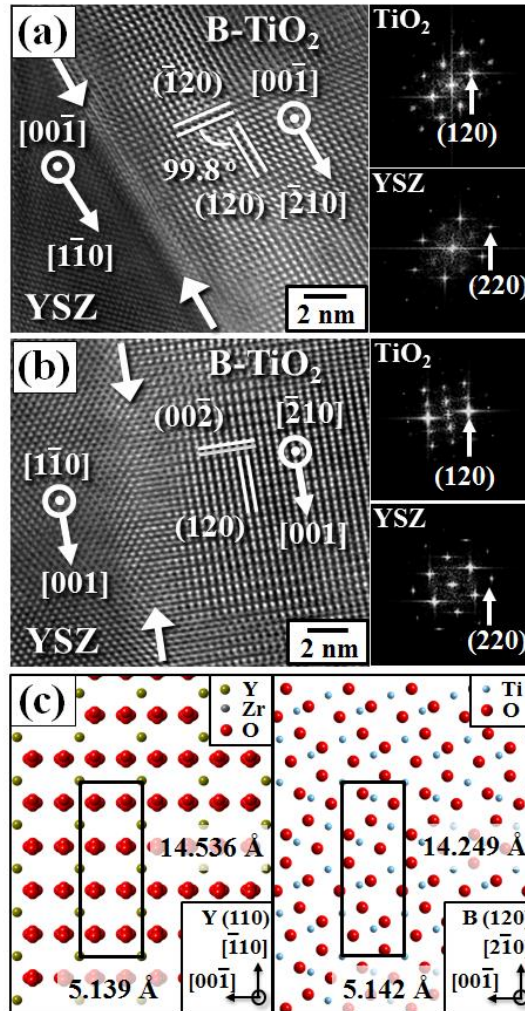


Figure 4.15. HRTEM images and FFT patterns for B-TiO₂ film and YSZ viewed along (a) [00 $\bar{1}$] and (b) [1 $\bar{1}$ 0] directions of YSZ. (c) Schematic diagrams of in-plane atomic configurations for (120) B-TiO₂ film and (110) YSZ substrate.

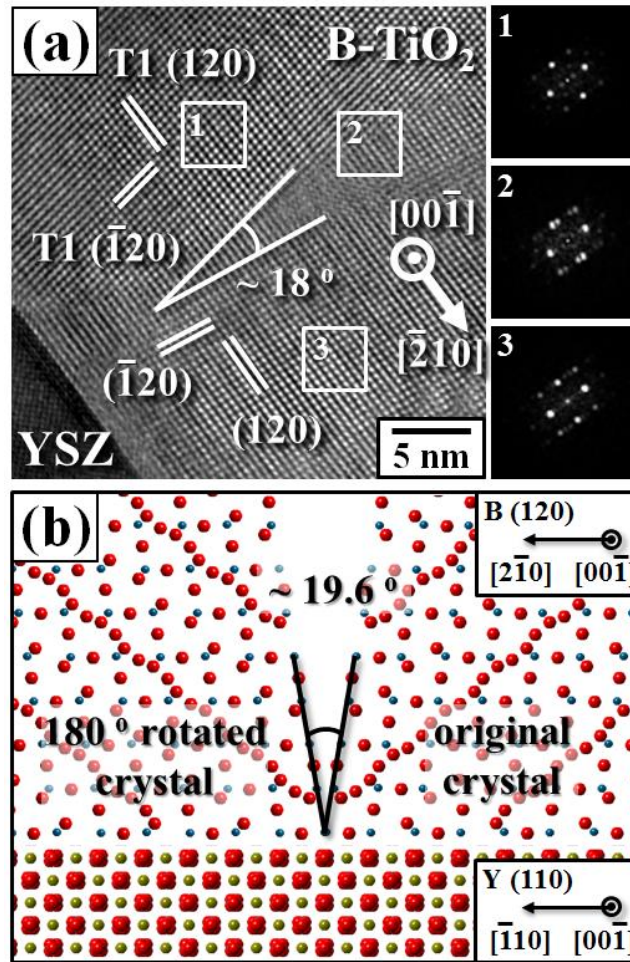


Figure 4.16. (a) HRTEM image and FFT patterns for B-TiO₂ film viewed along [00 $\bar{1}$] direction of YSZ. (120) B-TiO₂ and 180° rotated (120) B-TiO₂ films were observed, which was consistent with pole figure data. (b) Schematic diagrams of in-plane atomic configurations for (120) and 180 rotated (120) B-TiO₂ films on (110) YSZ substrate.

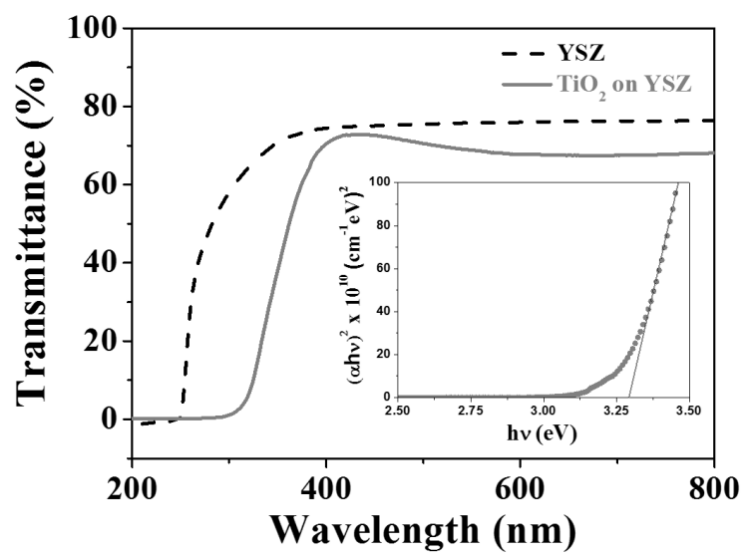


Figure 4.17. Optical transmittance spectra of B-TiO₂ film and bare YSZ substrate. The inset shows a plot of $(\alpha E)^2$ vs. E for B-TiO₂ film.

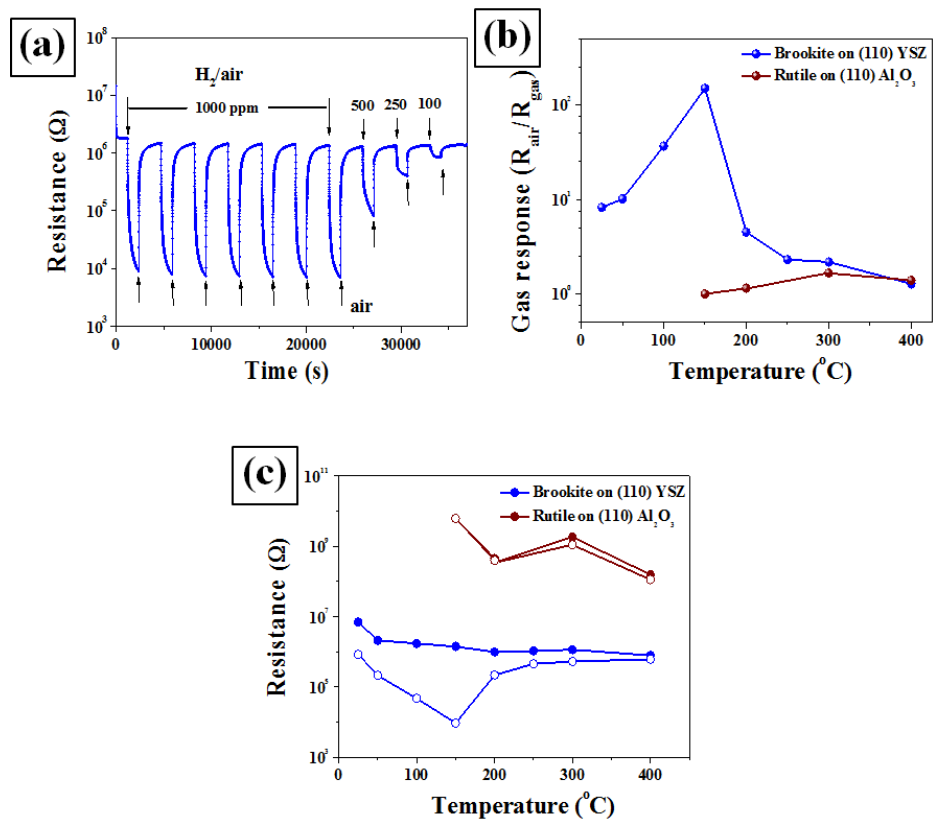


Figure 4.18. (a) Typical response transient of the B-TiO₂ film toward H₂ gas/air (1000-100 ppm) measured at 150 $^{\circ}$ C. (b) Magnitude of gas response toward 1000 ppm H₂/air in the films grown on (110) YSZ and (110) Al₂O₃ substrates as a function of sensing temperature. (c) Electrical resistances of the films grown on (110) YSZ and (110) Al₂O₃ substrates in air and 1000 ppm H₂/air as a function of operating temperature. (closed circles : resistance in air (R_{air}), open circles : resistance in 1000 ppm H₂/air (R_{gas})).

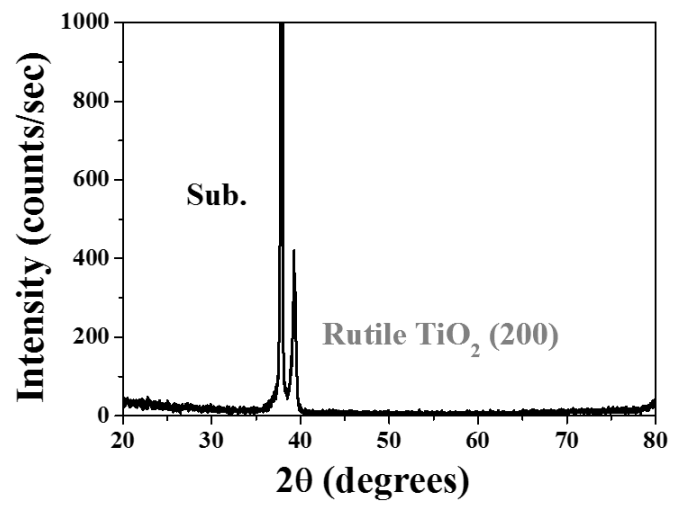


Figure 4.19. XRD pattern of TiO₂ film deposited on a-cut (110) Al₂O₃ substrate.

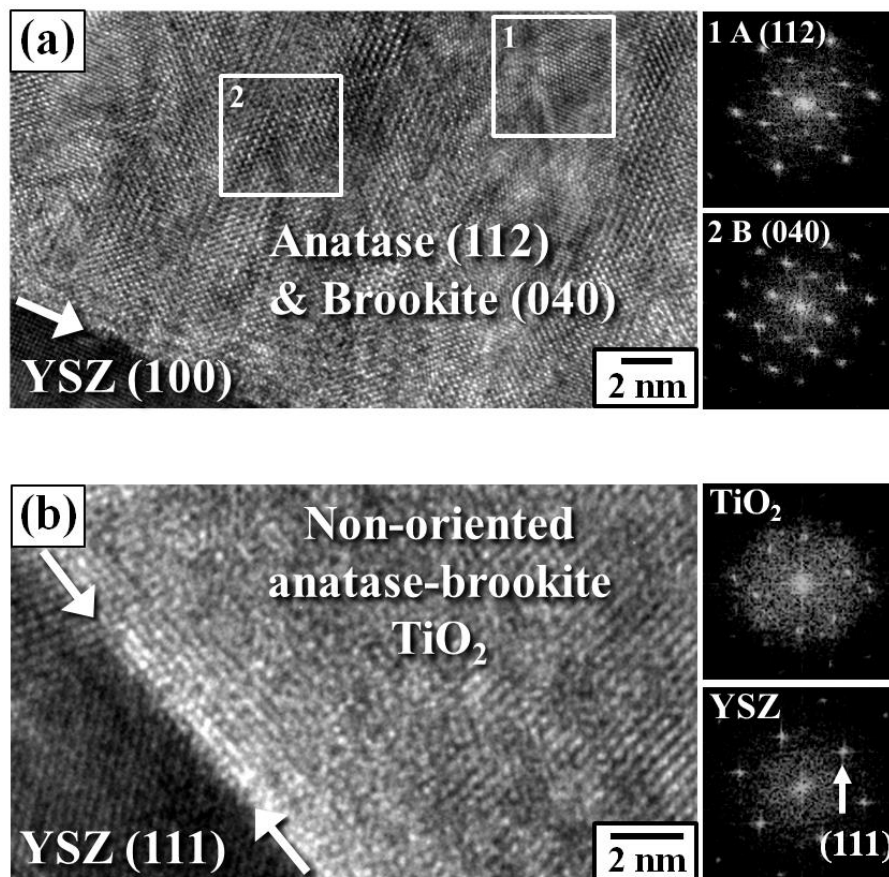


Figure 4.20. HRTEM images and FFT patterns for the films deposited on (a) (100) and (b) (111) YSZ substrates.

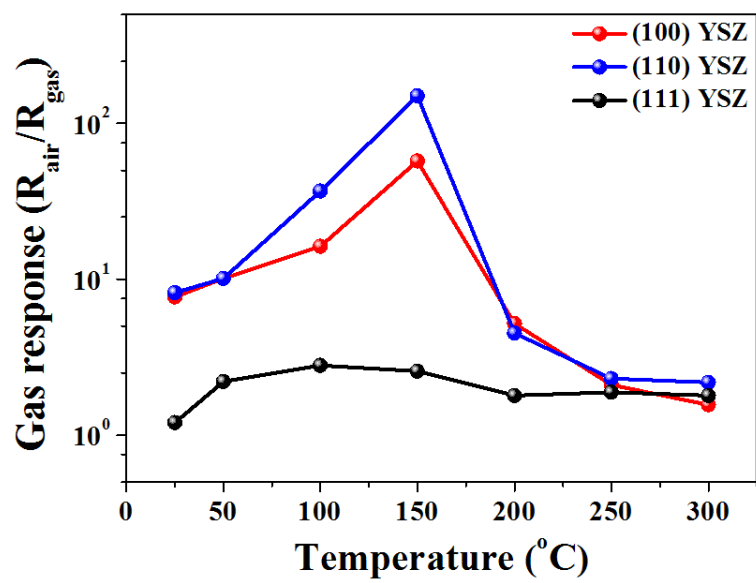


Figure 4.21. Magnitude of H₂ gas response for the films deposited on (100), (110), and (111) YSZ substrates.

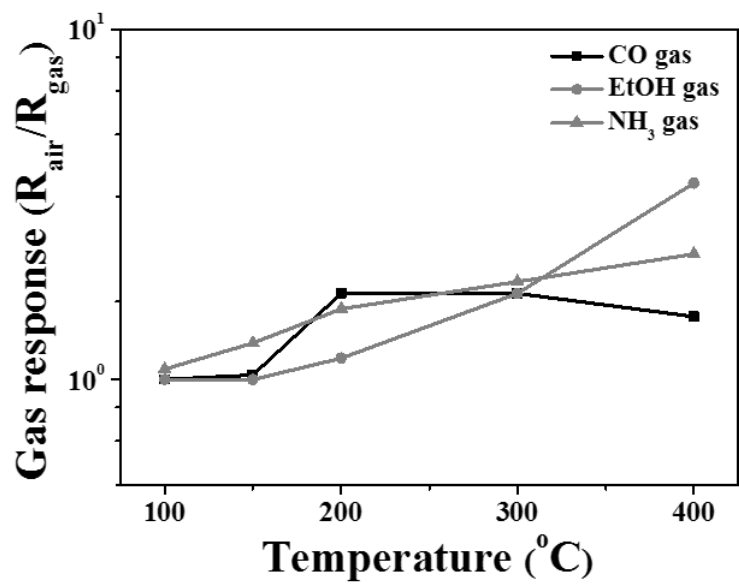


Figure 4.22. Magnitude of gas response for 1000 ppm CO, EtOH, and NH₃ in B-TiO₂ film sensor.

4.3. SnO₂-TiO₂ dual layer gas sensors

4.3.1. SnO₂ and TiO₂ single layer gas sensor

The gas sensing properties and the electrical resistance of SnO₂ thin films with temperature variations were shown in Figure 4.23. Gas response of each sample to 1000 ppm H₂ gas in air balance was measured temperature variations from 300 to 100 °C due to measuring stable gas sensing even though samples annealed at 400 °C and 600 °C. When the sensors were annealed at 400 °C, the gas response was relatively low at low temperature and maximum gas response was detected at 300 ~ 400 °C in the relatively thick film sensor and these response can be explained by activation of gases by high temperature. However, when the sensors were annealed at 600 °C, gas sensors deposited with 50 cycles ALD process showed the abnormal gas response, and showed the maximum gas response at 100 °C which is almost 10³. Suzuki et al. [23] reported H₂ gas sensing properties of SnO₂ thin film gas sensors with thickness variations. They reported when the operating temperature is at 150 °C, the maximum gas response was represented at ultra-thin SnO₂ thin film which is near debye length ~ 4 nm. Therefore, it can assume that SnO₂ thin film with 4 nm is the optimum conditions for low temperature H₂ gas sensing. Also, electrical resistance was investigated with air (closed symbol) and 1000 ppm H₂/air

(opened symbol). In the case of samples annealed at 400 °C, the tendency of resistance in air is followed that of gas response. On the other hand, the electrical resistance of gas sensor annealed at 600 °C changed both of cases in air and in gas with temperature variations.

TiO₂ single layer gas sensors were also investigated with temperature variations in Figure 4.24. Only, the gas response was represented without annealing at low temperature. When the sensors were annealed, the electrical resistance was extremely high and the sensor signal could not confirm after exposure of 1000 ppm H₂/air gas. Usually, TiO₂ gas sensors measured at high temperature [34,35] or with H₂/N₂ gases [12,36] due to high oxidation states. Some of researchers reported the low temperature gas sensing of TiO₂ using metastable structure such as anatase [37,42] and brookite. Although the structure analysis is still required, the gas response of non-annealed TiO₂ thin film should be measured due to metastable phase of TiO₂.

4.3.2. Structure of SnO₂-TiO₂ dual layer

The SnO₂-TiO₂ dual layer gas sensor is suggested for selective gas sensing because SnO₂ gas sensor shows generally show the poor selectivity which will be discussed at 4.3.4 in the gas selectivity part. Figure 4.25 is the HR-TEM

image of SnO₂-TiO₂ dual layer which is bare and 450 °C and 600 °C annealing process with EDS profiling. Bare dual layer shows the separated interfaces of SnO₂ and TiO₂ with thickness about 3 nm for each layer and the crystal structure was amorphous phase. When the dual layer is annealed at 450 °C, films were crystallized and the crystallographic structure can be defined by rutile structure using FFT pattern (see inset in Figure 4.25 (b)) with small amount of unknown peaks. After 600 °C annealing process, the dual layer is a little mixed each other and film thickness is increased which can be confirmed by EDS profile. The thickness variations are expected due to morphology changes due to high temperature annealing process. Therefore, the morphologies of dual layers are investigated using AFM with scan area (1 μm x 1 μm) in Figure 4.26. Until 450 °C annealing process, the significant morphology changes are not observed with 0.115 nm and 0.179 RMS roughness (bare and 450 °C) but when the layer is annealed at 600 °C, the groove morphology is observed with 1 nm RMS roughness. Also, some particles show the 2 nm height which is almost 1/3 of original film thickness (6 nm). From the TEM and AFM results, the annealing temperature can be optimized at near 450 °C.

4.3.3. Gas sensing properties of SnO₂-TiO₂ dual layer

The gas sensing properties of SnO₂-TiO₂ dual layer are confirmed with annealing temperature variations at room temperature in Figure 4.27. From the gas response graph, the optimum annealing condition can be also confirmed, which is 400 °C or 500 °C. When the sensors annealed at 300 °C, the initial resistance is low to react to reducing gases and after 600 °C heat treatment, the sensors is degraded due to extreme morphology change. Therefore, we fixed annealing temperature at 400 °C for low temperature H₂ gas sensing.

Figure 4.28 is the gas response and the electrical resistance of dual layer sensors with processing cycle variations of SnO₂ and TiO₂ film. When the deposition cycles of SnO₂ layer are increased to 100 cycles about 3 nm thick increases, the initial resistances of sensors are also greatly decreased and the gas response is decreased. Therefore, the optimum thickness of SnO₂ in dual layer is optimized the thickness at 50 cycles as same as SnO₂ single layer sensor at part 4.3.1. TiO₂ cycles are also varied at 50 cycles as the center. When the TiO₂ processing cycles are increased, the optimum gas response is shifted to high temperature, which means more activation energy is required for oxidation and reduction. On the other hand, the gas response of dual layer is decreased with decreasing TiO₂ layer. In this case, the low gas response is considered as low annealing temperature of dual layer as mentioned in SnO₂ single layer gas sensor at part

4.3.1.

To confirm electrode effects, the magnitude of gas response is investigated with different electrodes in Figure 4.29 (a). Au and Ti-Pt electrodes were selected to confirm the catalytic effect and Schottky effect of Pt electrode. Gas response using Au electrode showed the extremely low compared to Pt and Ti-Pt electrode. Therefore, catalytic effect is very important point in dual layer gas sensor for low temperature H₂ gas sensing as mentioned many researchers [11,12,36]. However, it seems that Schottky effect is not significant part in the dual layer sensor, which is different with low temperature sensing mechanism of TiO₂ sensor [39,42]. From the I-V curve in Figure 4.29 (b), the Schottky junction is confirmed in air and in 1000 ppm H₂/air gas with two different electrodes. The sensor with Pt electrode showed the curved graph in air which can be estimated of Schottky junction effect but the sensor with Pt-Ti electrode showed the linear graph. Therefore, dual layer gas sensor is reacted by catalytic effect.

4.3.4. Gas selectivity of SnO₂-TiO₂ dual layer

Gas selectivity is the very important part of H₂ gas sensor because environment for H₂ sensing is exposed with various gases such as NO_x, H₂O or other

reducing gases. Firstly, NO_x gas selectivity of dual layer is confirmed at room temperature and 100 °C (Figure 4.30 (c) and (d)) compared with SnO₂ single layer which is annealed at 600 °C (Figure 4.30 (a) and (b)). SnO₂ single layer sensor was significantly influenced to NO_x gas at room temperature which is almost no detection and gas response was decreased at 100 °C. This poor selectivity is concerned of favorable gas response of SnO₂ to NO_x gas due to many defective sites on SnO₂ surface [76]. On the other hand, dual layer sensors exhibited the high selectivity at both of temperatures. In this case H₂ gas selectivity against the humidity is measured using dual layer sensor in Figure 4.31 using H₂O bubbling system at 50 % R.H.@25 °C. At room temperature, the gas response is significantly decreased with wet air but the sensor showed the favorable gas sensing at 100 °C. Also, the sensor response of other reducing gas at 100 °C is exhibited in Figure 4.32. As shown in figure, dual layer showed the selective H₂ gas sensing toward other reducing gases.

4.3.5. Gas sensing mechanism

High gas response of dual-layer gas sensors are suggested by various effects such as junction effect and crystallization effect. Yeh et al. [81] suggested hetero-junction effects at SnO₂-TiO₂ dual layer interface. The hetero junction is formed at the interface between TiO₂ and SnO₂ because electrons are

transferred from TiO_2 to SnO_2 due to the higher work function of SnO_2 and the high electron affinity of TiO_2 (4.33 eV). Initial resistance of SnO_2 - TiO_2 dual layer is increased in air and dual layer film showed higher gas response than single layer film. According to the surface model, the gas response (S) can be proportional to concentration of sites in which charge transfer takes place (adsorption sites) and inverse proportional to the free electron concentration (carrier concentration). [82] In SnO_2 , because oxygen vacancies are main carrier concentration, carrier concentration can be adjusted by heat treatment. SnO_2 single layer film annealed at 600 °C shows higher gas response than SnO_2 film annealed at 400 °C. In the dual layer gas sensor, TiO_2 thin film acts as catalyst for stoichiometric SnO_2 at 400 °C and effectively reduces the carrier concentrations.

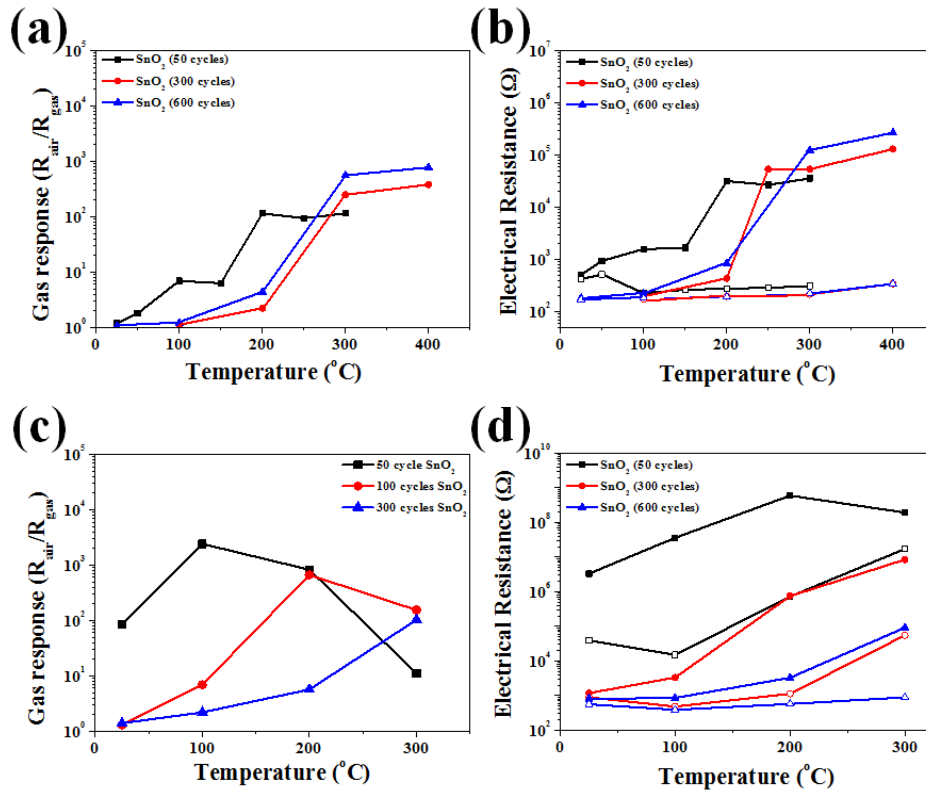


Figure 4.23. Magnitude of gas response to 1000 ppm H₂/air and electrical resistance of SnO₂ thin film annealed at 400 °C ((a) and (b)) and 600 °C ((c) and (d)) (closed circles : resistance in air (R_{air}), open circles : resistance in 1000 ppm H₂/air (R_{gas}))

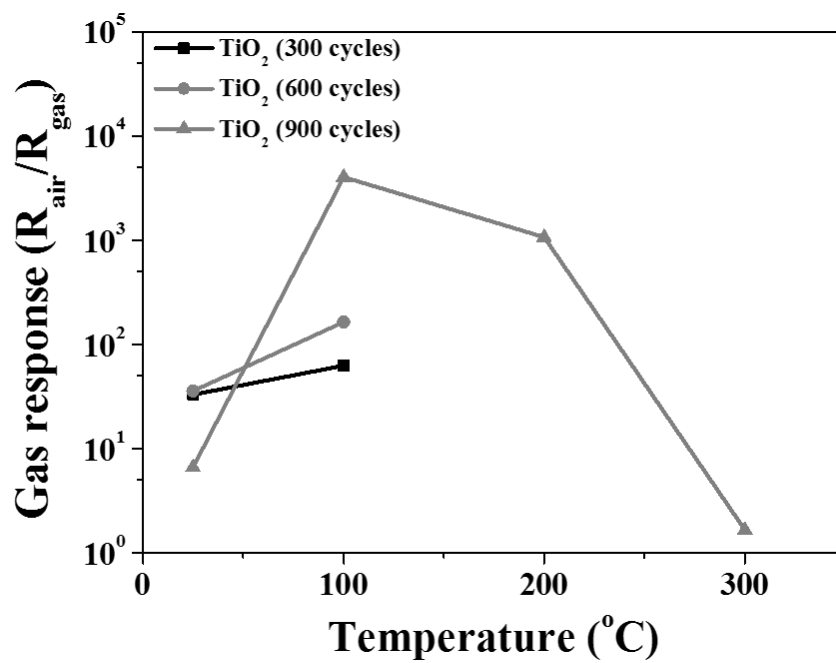


Figure 4.24. Magnitude of gas response to 1000 ppm H₂/air of TiO₂ thin film with temperature variations

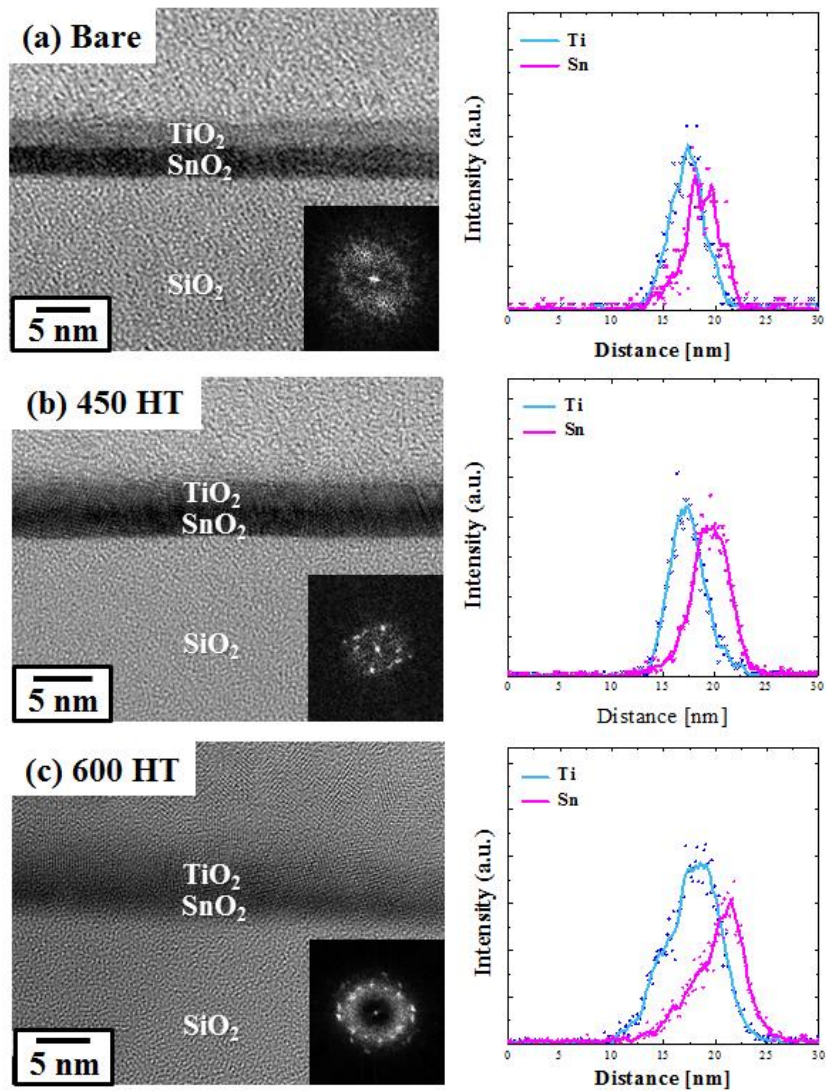


Figure 4.25. High resolution TEM image and EDS profiles of SnO₂-TiO₂ dual layer sensors with annealing temperature variations: (a) as deposited, (b) annealed at 450 °C, and (c) annealed at 600 °C

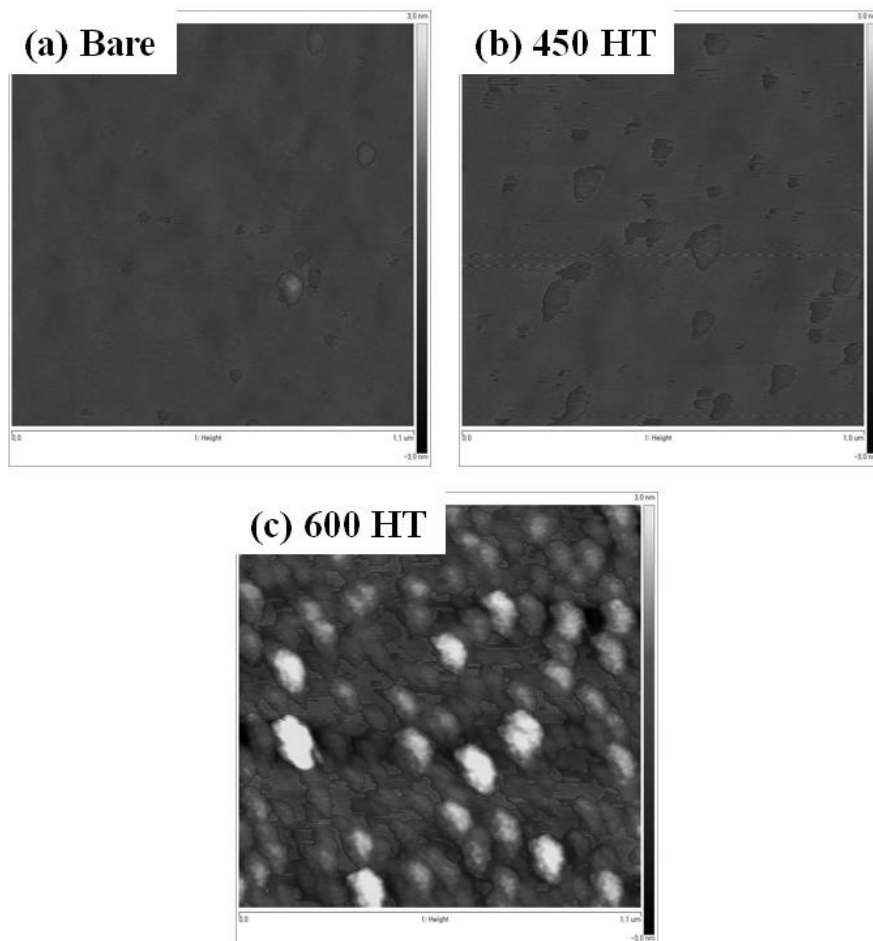


Figure 4.26. AFM images of SnO₂-TiO₂ dual layer sensors with annealing temperature variations: (a) as deposited, (b) annealed at 450 °C, and (c) annealed at 600 °C

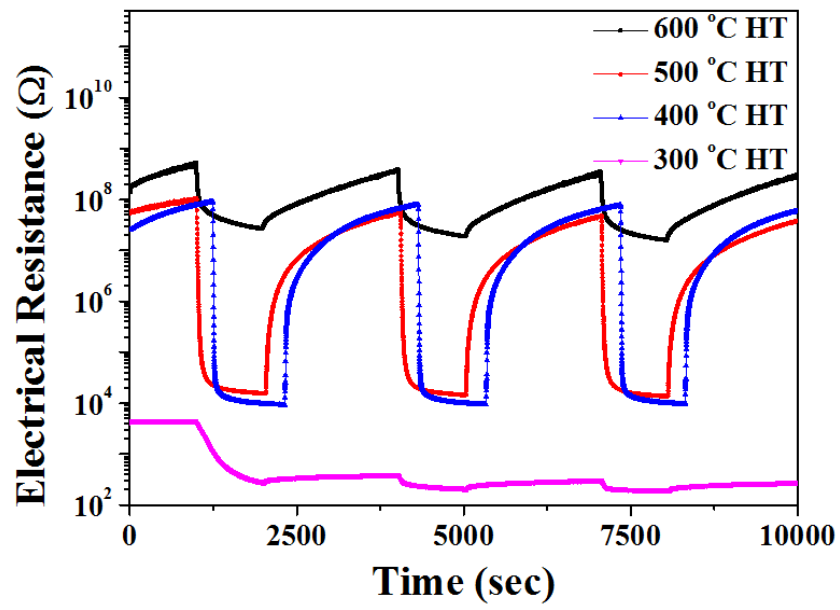


Figure 4.27. Gas response transients of SnO₂-TiO₂ dual layer sensors with annealing temperature variations

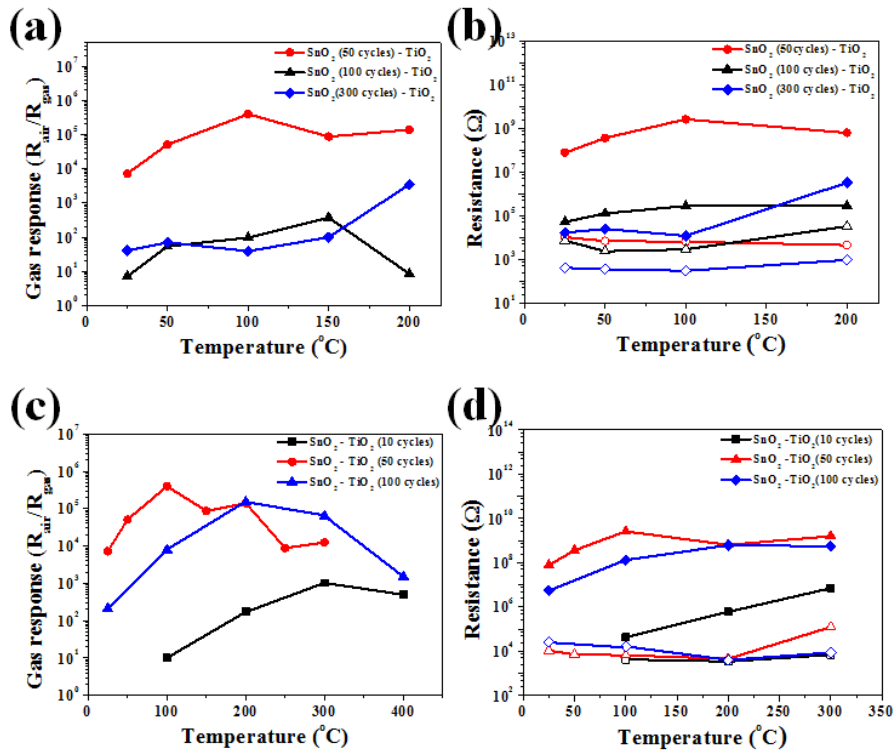


Figure 4.28. Gas response and electrical resistance of SnO₂-TiO₂ dual layer sensors (a) and (b) with processing cycle variations of SnO₂, and (c) and (d) with processing cycle variations of TiO₂ (closed circles : resistance in air (R_{air}), open circles : resistance in 1000 ppm H₂/air (R_{gas}))

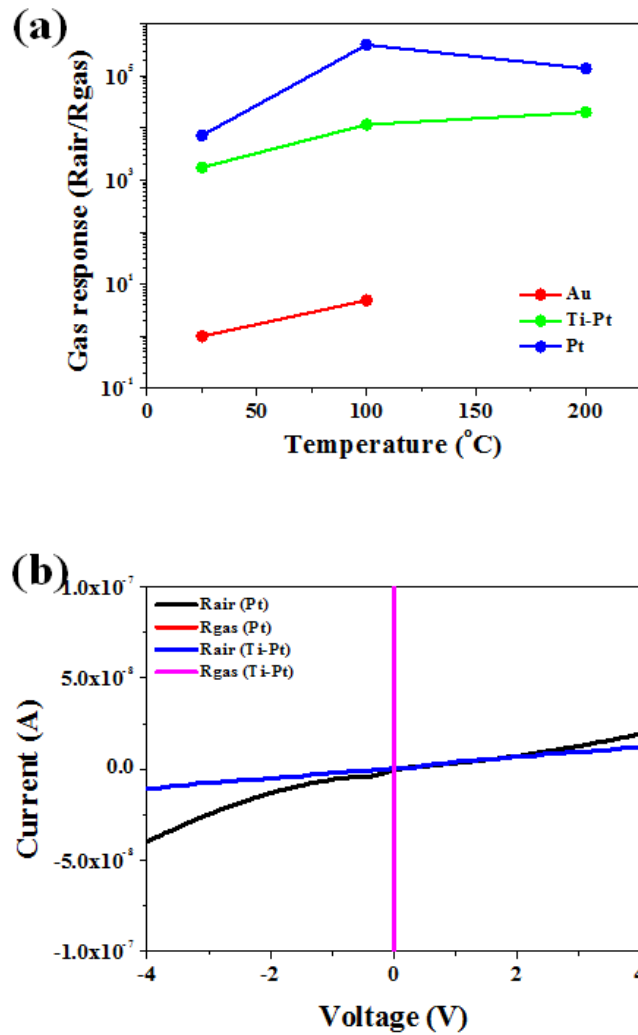


Figure 4.29. (a) Low temperature gas response of SnO₂-TiO₂ dual layer sensor with electrode variations and (b) I-V characteristics of SnO₂-TiO₂ dual layer sensor at 25 °C

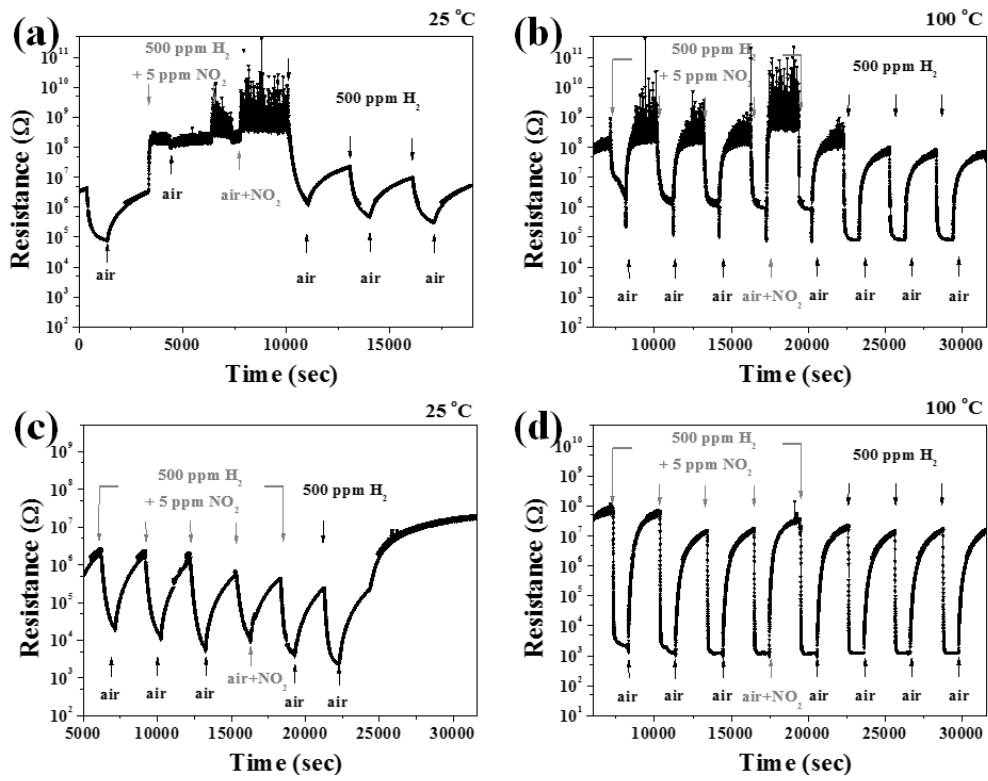


Figure 4.30. Gas response transient of SnO_2 single layer gas sensor (a) at 25 °C and (b) at 100 °C, and gas response transient of SnO_2 - TiO_2 dual layer gas sensor (c) at 25 °C and (d) at 100 °C.

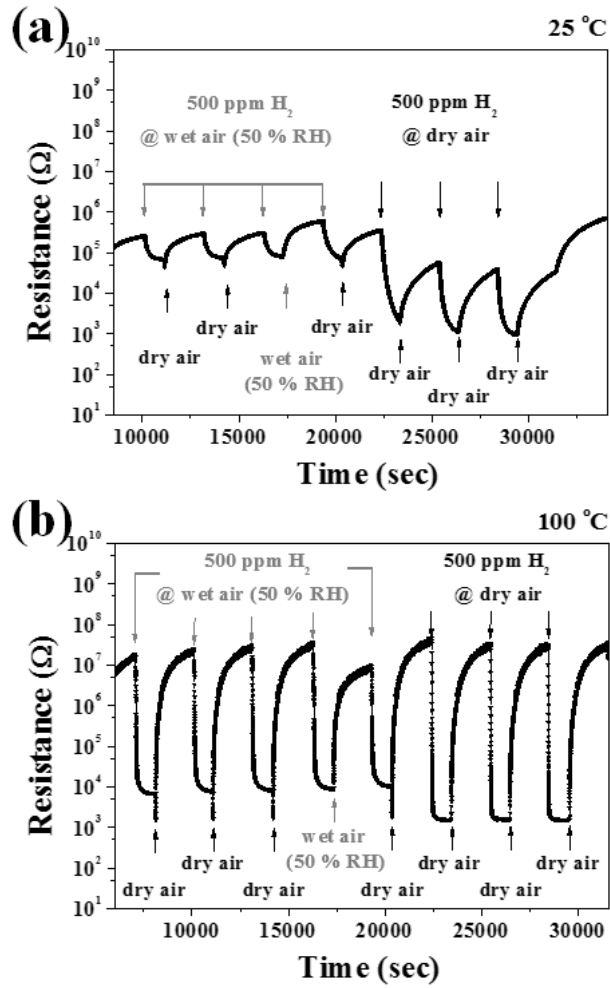


Figure 4.31. Humidity influences of SnO₂-TiO₂ dual layer sensor (a) at 25 °C, and (b) at 100 °C

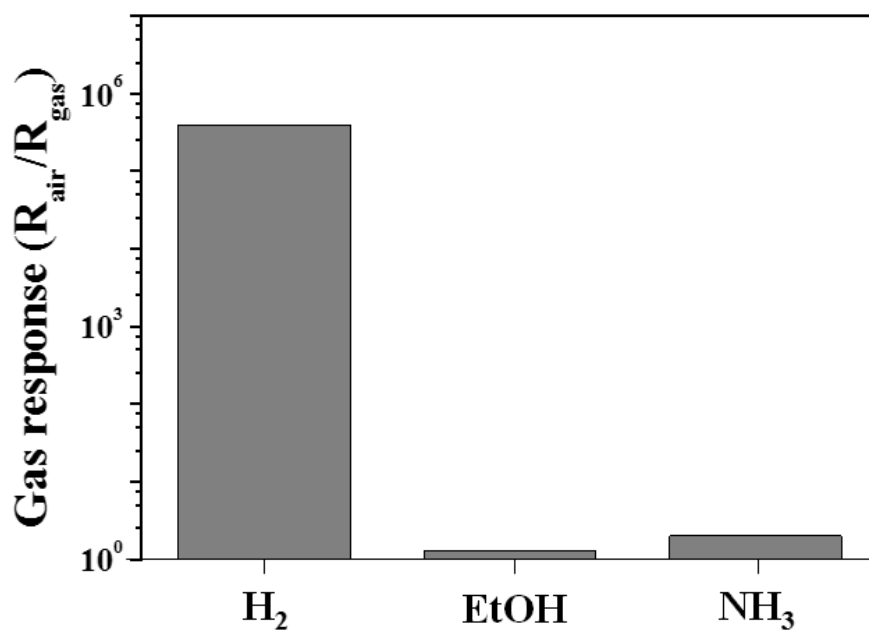


Figure 4.32. Gas response of various reduction gases (1000 ppm H_2 /air, 1000 ppm EtOH/air, 1000 ppm NH_3 /air) on SnO_2 - TiO_2 dual layer sensor measured at 100 °C.

Chapter 5. Conclusions

5.1. Oriented SnO₂ thin films grown on TiO₂ single crystals

Epitaxial SnO₂ films with various orientations were successfully obtained on various cuts of TiO₂ single crystal by PEALD. Out of- and in-plane orientations of SnO₂ films, examined by X-ray diffraction, X-ray pole figure, and selected area electron diffraction, exactly followed substrate orientations. All the SnO₂ films were ~90 nm thick after 1000 ALD cycles and had the similar surface morphology and chemical composition. Epitaxial SnO₂ film sensors responded to H₂ gas at lower temperature (300~500 °C) than the previously reported oriented polycrystalline film sensors. Compared to the other oriented films, the (101) SnO₂ films grown on (101) TiO₂ exhibited the higher H₂ gas response, which was closely related to the different temperature dependence of resistance. The epitaxial SnO₂ film sensors showed a high selectivity for H₂ against NH₃ and CO gases.

5.2. Brookite TiO₂ thin film epitaxially grown on YSZ substrates

B-TiO₂ film was successfully deposited on (110) YSZ substrate at 300 °C by PEALD. TiO₂ film was epitaxially grown on YSZ substrate, and the heteroepitaxial relationships were determined by XRD, pole figure, and HRTEM. As-deposited film was thermally stable, and the brookite phase was maintained up to 700 °C. The average transmittance of B-TiO₂ film was about 70 % in the visible range, and the optical band gap energy was estimated to be 3.29 eV. The B-TiO₂ film sensor stably responded to H₂ gas in air at a relatively low temperature. The maximum gas response toward H₂ gas was observed at 150 °C and B-TiO₂ film sensor exhibited the high selectivity for H₂ against CO, EtOH, and NH₃.

5.3. SnO₂-TiO₂ dual layer gas sensor

SnO₂-TiO₂ dual layer gas sensors are fabricated for low temperature selective H₂ gas sensor using PE-ALD method. The gas sensing properties of dual layer is investigated with SnO₂ and TiO₂ thickness variations and the optimum gas response was observed at ~ 4 nm of SnO₂ and ~ 4 nm of TiO₂. Dual layer sensor showed the excellent gas selectivity against NO_x gas compared with SnO₂ single layer sensor. Although the dual layer sensors exhibited poor selectivity against humidity, the problem is solved with adjusting of operating temperature up to 100 °C.

References

- [1] T. Hübert, L. Boon-Brett, G. Black, U. Banach, *Sensors and Actuators B*, 157 (2011) 329-352.
- [2] H. Gu, Z. Wang, Y. Hu, *Sensors*, 12 (2012) 5517-5550.
- [3] J. X. Wang, X. W. Sun, H. Huang, Y. C. Lee, O. K. Tan, L. Vayssleres, *Nanotechnology*, 17 (2006) 4995-4998
- [4] W.-S. Kim, B.-S. Lee, D.-H. Kim, H.-C. Kim, W.-R. Yu, S.-H. Hong, *Nanotechnology*, 21 (2010) 245605 (7p)
- [5] G. Korotcenkov, *Sensors and Actuators B*, 107 (2005) 209-232
- [6] C. Wang, L. Yin, L. Zhang, D. Xiang, R. Gao, *Sensors*, 10 (2010) 2088-2106
- [7] S. Semancik, R. E. Cavicchi, *Thin Solid Films*, 206 (1991) 81-87
- [8] T. Suntola, *Mater. Sci. Rep.* 4 (1989) 261-.312
- [9] N. Yamazoe, G. Sakai, K. Shimano, *Catalysis Surveys from Asia* 7 (2003) 63-75.
- [10] H. Huang, H. Gong, C. L. Chow, J. Guo, T. J. White, M. S. Tse, O. K. Tan, *Adv. Funct. Mater.* 21 (2011) 2680-2686
- [11] J. M. Lee, J.-E. Park, S. Kim, E. Lee, S.-J. Kim, *Int. J. Hydrogen Energy*, 35 (2010) 12568-12573

- [12] O. K. Varghese, D. Gong, M. Paulose, K. G. Ong, C. A. Grimes, *Sensors and Actuators B* 93 (2003) 338-344
- [13] L. Boon-Brett, J. Bousek, G. Black, P. Moretto, P. Castello, T. Hübner, U. Banach, *Int. J. Hydrogen Energy*, 35 (2010) 373-384
- [14] A. Katsuki, K. Fukui, *Sensors and Actuators B* 52 (1998) 30-37
- [15] G. Tournier, C. Pijolat, *Sensors and Actuators B* 106 (2005) 553-562
- [16] R. A. Kadir, Z. Li, A. Z. Sadek, R. A. Rani, A. S. Zoolfakar, M. R. Field, J. Z. Ou, A. F. Chrimes, K. Kalantar-zadeh, *J. Phys. Chem. C* 118 (2014) 3129–3139
- [17] A. Z. Adamyan, Z.N. Adamyan, V.M. Aroutiounian, *Int. J. Hydrogen Energy*, 34 (2009) 8438-8443
- [18] P. A. Russo, N. Donato, S. G. Leonardi, S. Baek, D. E. Conte, G. Neri, N. Pinna, *Angew. Chem. Int. Ed.* 51 (2012) 11053-11057
- [19] S. Shukla, P. Zhang, H. J. Cho, S. Seal, L. Ludwig, *Sensors and Actuators B* 120 (2007) 573-583
- [20] S. Shukla, S. Seal, L. Ludwig, C. Parish, *Sensors and Actuators B* 97 (2004) 256-265
- [21] S. Shukla, P. Zhang, H. J. Cho, Z. Rahman, C. Drake, S. Seal, V. Craciun, L. Ludwig, *J. Appl. Phys.* 98 (2005) 104306

- [22] C.-H. Han, S.-D. Han, I. Singh, T. Toupance, *Sensors and Actuators B* 109 (2005) 264-269
- [23] T. Suzuki, T. Yamazaki, H. Yoshioka, K. Hikichi, *J. Mater. Sci.* 23 (1988) 1106-1111
- [24] A. L. Linsebigler, G. Lu, J. T. Yates Jr., *Chem. Rev.* 95 (1995) 735-758
- [25] S. Ito, S. M. Zakeeruddin, R. Humphry-Baker, P. Liska, R. Charvet, P. Comte, M. K. Nazeeruddin, P. Péchy, M. Takata, H. Miura, S. Uchida, M. Grätzel, *Adv. Mater.* 18 (2006) 1202-1205
- [26] Y. Shimizu, N. Kuwano, T. Hyodo, M. Egashira, *Sensors and Actuators B* 83 (2002) 195-201
- [27] W. Hu, L. Li, G. Li, C. Tang, L. Sun, *Crystal Growth & Design* 9(8) (2009) 3476-3682
- [28] K. R. Moonosawmy, H. Katzke, M. Es-Souni, M. Dietze, M. Es-Souni, *Langmuir* 28 (2012) 6706-6713
- [29] D. dambournet, I. Belharouak, K. Amine, *Chem. Mater.* 22 (2010) 1173-1179
- [30] M. Addamo, M. Bellardita, A. D. Paola, L. Palmisano, *Chem. Commun.* (2006) 4943-4945
- [31] Y. Djaoued, R. Brüning, D. Bersani, P.P. Lottici, S. Badilescu, *Materials Letters* 58 (2004) 2618-2622

- [32] A. D. Paola, M. Addamo, M. Bellardita, E. Cazzanelli, L. Palmisano, *Thin Solid Films* 515 (2007) 3527-3529
- [33] I.N. Kuznetsova, V. Blaskov, I. Stambolova, L. Znaidi, A. Kanaev, *Materials Letters* 59 (2005) 3820-3823
- [34] C. Lu, Z. Chen, *Sensors and Actuators B* 140 (2009) 109-115
- [35] W.-T. Moon, K.-S. Lee, Y.-K. Jun, H.-S. Kim, S.-H. Hong, *Sensors and Actuators B* 115 (2006) 123-127
- [36] M. K. Kumar, L. K. Tan, N. N. Gosvami, H. Gao, *J. Phys. Chem. C* 113 (2009) 6381-6389
- [37] J. Lee, D.-H. Kim, S.-H. Hong, J. Y. Jho, *Sensors and Actuators B* 160 (2011) 1494-1498
- [38] M. Epifani, A. Helwig, J. Arbiol, R. D'áz, L. Francioso, P. Siciliano, G. Mueller, J. R. Morante, *Sensors and Actuators B* 130 (2008) 599-608
- [39] K. Chen, K. Xie, X. Feng, S. Wang, R. Hu, H. Gu, Y. Li, *Int. J. Hydrogen Energy*, 37 (2012) 13602-13609
- [40] A. Z. Sadek, J.G. Partridge, D.G. McCulloch, Y.X. Li, X.F. Yu, W. Wlodarski, K. Kalantar-zadeh, *Thin Solid Films* 518 (2009) 1294-1298
- [41] F. Ren, L. Huang, Y. Ling, J. Feng, *Sensors and Actuators B* 148 (2010) 195-199

- [42] Y. Shimizu, T. Hyodo, M. Egashira, *Sensors and Actuators B* 121 (2007) 219-230
- [43] M. Guo, X. Xia, Y. Gao, G. Jiang, Q. Deng, G. Shao, *Sensors and Actuators B* 171-172 (2012) 165-171
- [44] M. Egashira, T. Matsumoto, Y. Shimizu, *Sensors and Actuators* 14 (1988) 205-213
- [45] Y.-H. Choi, S.-H. Hong, *Sensors and Actuators B* 125 (2007) 504-509
- [46] M. Utriainen, H. Lattu, H. Virola, L. Niinistö, R. Resch, G. Friedbacher, *Mikrochim. Acta* 133 (2000) 119-123
- [47] J. Sundqvist, A. Tarre, A. Rosental, A. Hårsta, *Chem. Vap. Deposition* 9 (2003) 21-25
- [48] J. Lu, J. Sundqvist, M. Ottosson, A. Tarre, A. Rosental, J. Aarik, A. Hårsta, J. *Crystal Growth* 260 (2004) 191-200
- [49] A. Tarre, A. Rosental, J. Sundqvist, A. Hårsta, T. Uustare, V. Sammelseg, *Surf. Sci.* 532-535 (2003) 514-518
- [50] A. Rosental, A. Tarre, A. Gerst, J. Sundqvist, A. Hårsta, A. Aidla, J. Aarik, V. Sammelseg, T. Uustare, *Sens. Actuators B* 93 (2003) 552-555
- [51] J. Sundqvist, J. Lu, M. Ottosson, A. Hårsta, *Thin Solid Films* 514 (2006) 63-68
- [52] H. Virola, L. Niinistö, *Thin Solid Films* 249 (1994) 144-149
- [53] H. Virola, L. Niinistö, *Thin Solid Films* 251 (1994) 127-135
- [54] C. Dücsö, N. Q. Khanh, Z. Horváth, I. Bársony, M. Utriainen, S. Lehto, M. Nieminen, L. Niinistö, *J. Electrochem. Soc.* 143 (1996) 683-687
- [55] M. Utriainen, K. Kovács, J.M. Campbell, L. Niinistö, F. Réti, *J. Electrochem. Soc.*

146 (1999) 189-193

[56] A. Rosental, A. Tarre, A. Gerst, T. Uustare, V. Sammelseg, *Sens. Actuators B* 77 (2001) 297-300

[57] S. K. Kim, W.-D. Kim, K.-M. Kim, C. S. Hwang, *Appl. Phys. Lett.* 85(18) (2004) 4112-4114

[58] D.-H. Kim, Thesis for Master's degree, Seoul National University (2008)

[59] H. Wakabayashi, T. Suzuki, Y. Iwazaki, M. Fujimoto, *Jpn. J. Appl. Phys.* 40 (2001) 6081-6087

[60] J. Oviedo, M.J. Gillan, *Surf. Sci.* 463 (2000) 93-101

[61] V. Caslavská, R. Rov, *J. Appl. Phys.* 40 (1969) 3414

[62] J. F. Moulder, A reference book of standard spectra for identification and interpretation of XPS data, Physical Electronics, Minnesota (1995)

[63] W. Gödel and K. D. Schierbaum, *Sens. Actuators B* 26 (1995) 1-12

[64] Y.-H. Choi, M. Yang, S.-H. Hong., *Sens. Actuators B* 134 (2008) 117-121

[65] K. Nomura, H. Shiozawa, T. Takada, H. Reuther, E. Richter, *J. Mater. Sci. Mater. Electron.* 8 (1997) 301-306

[66] S. W. Lee, P. P. Tsai, H. Chen, *Sens. Actuators B* 67 (2000) 122-127

[67] Y.-D. Wang, C.-L. Ma, X.-H. Wu, X.-D. Sun, H.-D. Li, *Sens. Actuators B* 85 (2002) 270-276

- [68] H. G. Kim, K. T. Kim, *Acta Mater.* 47 (1999) 3561-3570
- [69] H. Zhang, J. F. Banfield, *J. Phys. Chem. B* 104 (2000) 3481-3487
- [70] J.-G. Li, T. Ishigaki, *Acta Mater.* 52 (2004) 5143-5150
- [71] G. A. Tompsett, G. A. Bowmaker, R. P. Cooney, J. B. Metson, K. A. Rodgers, J. M. Seakins, *J. Raman Spectrosc.* 26 (1995) 57-62
- [72] Y. Gao, K. L. Merkle, H. L. Chang, T. J. Zhang, D. J. Lam, *Phil. Mag. A* 65(5) (1992) 1103-1125
- [73] T. A. Kandiel, A. Feldhoff, L. Robben, R. Dillert, D. W. Bahnemann, *Chem. Mater.* 22 (2010) 2050-2060
- [74] J.-G. Li, T. Ishigaki, X. Sun, *J. Phys. Chem. C* 111 (2007) 4969-4976
- [75] A. Lotnyk, S. Senz, D. Hesse, *Thin Solid Films* 515 (2007) 3439-3447
- [76] M. Epifani, J. D. Prades, E. Comini, E. Pellicer, M. Avella, P. Siciliano, G. Faglia, A. Cirera, R. Scotti, F. Morazzoni, J. R. Morante, *J. Phys. Chem. C* 112 (2008) 19540-19546
- [77] <http://www.Jseng.com/kor/>
- [78] S. J. Nog, S. K. Lee, E. H. Kim, Y. J. Kong, *Curr. Appl. Phys.* 6 (2006) 171-173
- [79] M. Ohring, *Materials Science of Thin Films*, Academic press (2002) 417-419

- [80] K.-B. Kim, Thin Film Technology-Lecture note, (2007)
- [81] M.-H. Yeh, W.-S. Hwang, G.-B. Lee, Y.-M. Lu, Materials Transactions 45(12) (2004) 3318-3323
- [82] F. Hernandez-Ramirez, J. D. Prades, A. Tarancon, S. Barth, O. Casals, R. Jimenez-Diaz, E. Pellicer, J. Rodriguez, J. R. Morante, M. A. Juli, S. Mathur, A. Romano-Rodriguez, Adv. Funct. Mater. 18 (2008) 2990-2994
- [83] D.-H. Kim, W.-S. Kim, S. B. Lee, S.-H. Hong, Sens. Actuators B 147 (2010) 653-659
- [84] D.-H. Kim, W.-S. Kim, S. Kim, S.-H. Hong, ACS Appl. Mater. Interfaces (2014) Accepted

국 문 초 록

환경 오염이 증가하면서 석탄, 석유 에너지를 대체할 수 있는 운반 에너지에 대해 연구가 활발히 진행되고 있다. 이 중에서 수소는 반응을 해서 물이 생성이 되므로 깨끗한 에너지 중 하나로 주목을 받고 있으며 이에 따라 폭발성을 가지는 수소 가스의 효과적인 검지에 대해서도 많은 관심을 보이고 있다. 수소 가스 센서에 대한 연구는 이미 오래전부터 진행이 되었으며 상용화된 센서도 나와있지만 그 응용처가 증가함에 따라 작은 크기로 빠르게 검지하는 능력과 더불어 낮은 생산 단가, 낮은 작동 온도 및 전력 소모, 다른 가스에 대한 선택성 (녹스 (NO_x), 에탄올 (EtOH), 수증기 (H₂O), etc), 장기 안정성 등이 보장되는 새로운 센서가 요구 되고 있다.

본 연구에서는 낮은 단가와 높은 감도를 가지는 반도체식 가스 센서에 주목을 하였으며 효과적인 센서 구조를 연구하기 위해 비교적 조건을 제어하기 쉬운 원자층 증착법을 이용하였다. 또한, 센서 물질로는 반도체형 가스 센서로서 많이 쓰이는 산화 주석 (SnO₂)와 산화 티타늄 (TiO₂)를 이용하였다. 본 연구의 결과는 크게 단결정 기판을 이용해서 물질의 결정학적 구조에 따른 센서 특성을 연구한 부분과 실리콘 기판 위에 두께

및 증착 구조를 변경하면서 가장 효과 적인 가스 센서의 조건을 확립하는 부분으로 나눌 수 있다.

가스 센서의 결정학적 특성에 대한 연구는 이론적으로 많이 되어 지고 있으며 특정 결정면을 가지거나 상이 변함에 따라 가스 센서의 감도 또한 변하는 것으로 보고 되고 있다. 이러한 현상을 실험적으로 확인을 하기 위해서는 변수 분리를 통해서 특정 결정면과 특정 상과 같이 원하는 부분만 변화를 시켜야 하지만 결정면 또는 상이 변하면서 그 표면 형상도 같이 변하기 때문에 결정면과 상에 대한 영향을 평가하기 어려운 문제점이 있다. 따라서 본 연구에서는 상용화된 단결정 기판 위에 증착하는 방법으로 원하는 요인만을 조절할 수 있었으며 결정면과 상에 대한 영향을 확인 할 수 있었다.

먼저, 결정면을 확인하기 위해서는 (110), (100), (101), (001) 결정면을 가지는 TiO_2 기판을 사용해서 SnO_2 박막을 성장하였으며 결정면에 따른 가스 감도를 확인하였다. (101) TiO_2 에 성장된 (101) SnO_2 박막의 경우 수소나 에탄올에 대해서 높은 감도를 보이는 것을 알 수 있었다. 이는 SnO_2 (101) 결정면이 공기 중의 산소와 가장 효과적으로 반응을 하기 때문에 가능한 것으로 생각 된다. 기존 문헌의 보고에 의하면 (101) 면이 산소와 흡착 또는 탈착 시 가장 낮은 에너지를 가지는 것으로 보고 되고 있으며 본 연구의 결과는 이를 실험적으로 증명을 하였다고 할 수 있다.

결정상에 대한 연구는 YSZ 기판 위에 증착한 TiO_2 박막을 사용하였다. 기존 TiO_2 물질에 대한 연구는 화학적이나 열적으로 안정하기 때문에 높은 작동온도에서 반응을 확인 하였으며 수소 센서 측정에 있어서 공기 분위기가 아닌 N_2 와 같은 불활성 분위기를 사용하였다. 하지만, 최근에는 TiO_2 저온 수소 반응성에 대한 보고가 있으며 이러한 특성에 대한 요인으로는 아나타제 (anatase)와 브루카이트 (brookite)와 같은 중간안정상이 제기되고 있다. 하지만 일반적인 방법으로는 표면 형상을 변화시키지 않고 상을 변화하는 것에 어려움이 있으며 이에 따라 기판을 사용하는 에피탁시얼 (epitaxial) 방법을 이용하였다. 본 연구에서는 중간 안정상인 브루카이트 박막을 (110) YSZ 기판 위에 성장 시켰으며 그 대조군으로 (110) 사파이어 기판을 이용해서 루타일 (rutile) 박막을 성장시켰다. 센서 측정 결과 브루카이트 박막이 성장된 센서가 보다 낮은 온도에서 작동을 하는 것을 확인하였으며 루타일 박막이 성장된 센서는 저온에서 측정이 어려우며 오직 불활성 분위기와 고온에서 반응을 하는 것을 확인하였다.

앞에 연구는 기초적인 센서 요인을 확인하기 위해서 진행이 되었지만 두번째로 진행된 연구는 값이 싸고 대량 생산이 가능한 실리콘 기판을 이용해서 효과 적인 센서를 구현하려고 하였으며 저온 동작 온도와 가스에 대한 선택성이 함께 고려되었다. 일반적인 SnO_2 박막은 고온에서 작동을 하며 대부분의 가스에 대해 반응을 하므로 수소에 대한 선택성이 낮은

것으로 보고되고 있다. 이를 효과적으로 제어하기 위해서 SnO₂의 두께에 따른 가스 감응 특성을 연구하였으며 흡착된 가스가 재료에 영향을 미치는 3~4 nm의 두께에서 우수한 저온 가스 감응 특성이 나타나는 것을 확인하였다. 하지만 제작된 센서는 여전히 녹스 (NO_x)에 대해서 낮은 선택성을 가졌으며 이를 극복하기 위해서 TiO₂ 박막을 SnO₂ 위에 증착하여 이중층의 박막 (dual-layer thin film)을 형성하였다. 생성된 박막은 각각의 두께가 3~4 nm의 두께를 가졌을 때 가장 효과적으로 반응을 하는 것을 확인하였다. 습도와 다른 환원성 가스에 대한 영향도 확인을 하였으며 100도에서 작동을 할 경우 그 선택성이 확보되는 것을 확인하였다.

주 요 어 : 가스 센서, 반도체식 가스 센서, 수소 가스 센서, 박막, 산화주석, 산화 티타늄, 원자층 증착법, 에피택시, 브루카이트, 이중층, 가스 선택성

학 번 : 2008-30847

Research Activities

Thesis

1. **Dai-Hong Kim**, “Growth of SnO₂ and TiO₂ thin films by PE-ALD : their structural characteristics and H₂ gas sensing properties” Ph.D. Thesis, Seoul National University, (2014).
2. **Dai-Hong Kim**, “H₂ and CO gas sensitivity of oriented SnO₂ thin films deposited by PE-ALD” Master degree Thesis, Seoul National University, (2008).

International Articles (SCI Journals)

1. **Dai-Hong Kim**, Won-Sik Kim, Sungtae Kim, Seong-Hyeon Hong, “Brookite TiO₂ Thin Film Epitaxially Grown on (110) YSZ Substrate by Atomic Layer Deposition” ACS Applied Materials & Interfaces (2014) Accepted
2. Yun-Hyuk Choi, **Dai-Hong Kim**, Hyun Soo Han, Sun Shin, Seong-Hyeon Hong, and Kug Sun Hong, "Direct Printing Synthesis of Self-Organized Copper Oxide Hollow Spheres on a Substrate Using Copper(II) Complex Ink: Gas Sensing and Photoelectrochemical Properties" Langmuir 30 (2014) 700–709
3. Shin-Ik Kim, **Dai-Hong Kim**, Yoonjung Kim, Seon Young Moon, Min-Gyu Kang, Jong Kwon Choi, Ho Won Jang, Seong Keun Kim, Ji-Won Choi, Seok-

Jin Yoon, Hye Jung Chang, Chong-Yun Kang, Suyoun Lee, Seong-Hyeon Hong, Jin-Sang Kim, Seung-Hyub Baek, "Non-Volatile Control of 2DEG Conductivity at Oxide Interfaces", *Advanced Materials* (2013) 25, 4612~4617

4. Jeong-Hoon Jeun, Kyu-Young Park, **Dai-Hong Kim**, Won-Sik Kim, Hong-Chan Kim, Byoung-Sun Lee, Honggu Kim, Woong-Ryeol Yu, Kisuk Kang, Seong-Hyeon Hong, "SnO₂@TiO₂ double-shell nanotubes for lithium ion battery anode with excellent high rate cyclability", *Nanoscale* 5 (2013) 8480~8483

5. **Dai-Hong Kim**, Choong Ki Lee, Jun Seong Lee, Seong-Hyeon Hong, Young Jin Kim, "Epitaxial recrystallization and luminescence of CaAl₂O₄:Eu²⁺ thin films prepared on sapphire substrates", *J. Electroceram.* 30 (2013) 36~40

6. Seon Young Moon, **Dai-Hong Kim**, Hye Jung Chang, Jong Kwon Choi, Chong-Yun Kang, Heon Jin Choi, Seong-Hyeon Hong, Seung-Hyub Baek, Jin-Sang Kim, Ho Won Jang, "Tunable conductivity at LaAlO₃/Sr_xCa_{1-x}TiO₃ (0≤x≤1) heterointerfaces", *Applied Physics Letters*, (2013) 102, 012903 1~4

7. Yun-Hyuk Choi, **Dai-Hong Kim**, Seong-Hyeon Hong, Kug Sun Hong, "H₂ and C₂H₅OH sensing characteristics of mesoporous p-type CuO films prepared via a novel precursor-based ink solution route", *Sensors and Actuators B* 178 (2013) 395~403

8. Jeong-Hoon Jeun, **Dai-Hong Kim**, Seong-Hyeon Hong, "SnO₂/CuO nano-hybrid foams synthesized by electrochemical deposition and their gas sensing properties" *Materials Letters* 105 (2013) 58~61

9. Won-Sik Kim, Yun-Guk Jang, **Dai-Hong Kim**, Hong-Chan Kim and Seong-Hyeon Hong, "Hetero-epitaxial growth of vertically-aligned TiO₂ nanorods on m-cut sapphire substrate with (001) SnO₂ buffer layer" Cryst. Eng. Comm. 14 (2012) 4963~4966

10. Min Gyun Chung, **Dai-Hong Kim**, Dong Kyun Seo, Tae woo Kim, Hyeong Uk Im, Hyun Myoung Lee, Ji-Beom Yoo, Seong-Hyeon Hong, Tae June Kang and Yong Hyup Kim, "Flexible Hydrogen Sensors using Graphene with Palladium Nanoparticle Decoration" Sensors and Actuators B 169 (2012) 387-392

11. Min Gyun Chung, **Dai Hong Kim**, Hyun Myoung Lee, Taewoo Kim, Jong Ho Choi, Dong kyun Seo, Ji-Beom Yoo, Seong-Hyeon Hong, Tae June Kang, Yong Hyup Kim, "Highly sensitive NO₂ gas sensor based on ozone treated grapheme", Sensors and Actuators B 166-167 (2012) 172-176

12. Sungtae Kim, **Dai-Hong Kim**, Seong-Hyeon Hong, "Epitaxial growth of orthorhombic SnO₂ films on various YSZ substrates by plasma enhanced atomic layer deposition" J. Cryst. Growth 348 (2012) 15~19

13. Hyunjoong Lee, Sanghoon Lee, **Dai-Hong Kim**, David Perello, Young June Park, Seong-Hyeon Hong, Minhee Yun and Suhwan Kim, "Integrating Metal-Oxide-Decorated CNT Networks with a CMOS Readout in a Gas Sensor", Sensors 12 (2012) 2582~2597

14. Won-Sik Kim, **Dai-Hong Kim**, Yun-Guk Jang and Seong-Hyeon Hong, "Synthesis of well-aligned SnO₂ nanowires with branches on r-cut sapphire substrate", CrystEngComm 14 (2012) 1545~1549

15. Jeong-Hoon Jeun, **Dai-Hong Kim**, Seong-Hyeon Hong, "Synthesis of porous SnO₂ foams on SiO₂/Si substrate by electrochemical deposition and their gas sensing properties", Sensors and Actuators B 161 (2012) 784~790

16. Sungkwon Cho, **Dai-Hong Kim**, Byoung-Sun Lee, Joohyun Jung, Woong-Ryeol Yu, Seong-Hyeon Hong and Seonghoon Lee, "Ethanol sensors based on ZnO nanotubes with controllable wall thickness via atomic layer deposition, an O₂ plasma process and an annealing process", Sensors and Actuators B 162 (2012) 300~306

17. Jiwon Lee, **Dai Hong Kim**, Seong-Hyeon Hong, Jae Young Jho, "A hydrogen gas sensor employing vertically aligned TiO₂ nanotube arrays prepared by template-assisted method", Sensors and Actuators B 160 (2011) 1494~1498

18. Byoung-Sun Lee, Won-Sik Kim, **Dai-Hong Kim**, Hong-Chan Kim, Seong-Hyeon Hong and Woong-Ryeol Yu, "Fabrication of SnO₂ nanotube microyarn and its gas sensing behavior", Smart Mater. Struct. 20 (2011) 105019

19. Yun-Guk Jang, Won-Sik Kim, **Dai-Hong Kim** and Seong-Hyeon Hong, "Fabrication of Ga₂O₃ – SnO₂ core – shell Nanowires by Thermal Evaporation and Atomic Layer Deposition and Their Gas Sensing Properties toward Ethanol", J. Mater. Res. 26 (17) (2011) 2322~2327

20. **Dai-Hong Kim**, Ji-Hwan Kwon, Miyoung Kim, Seong-Hyeon Hong, “Structural characteristics of epitaxial SnO₂ films deposited on a- and m-cut sapphire by ALD”, J. Cryst. Growth. 322 (2011) 33~37
21. Tae June Kang, Ajeong Choi, **Dai-Hong Kim**, Kyoungcheol Jin, Dong Kyun Seo, Dae Hong Jeong, Seong-Hyeon Hong, YungWoo Park and Yong Hyup Kim “Electromechanical properties of CNT-coated cotton yarn for electronic textile applications”, Smart Mater. Struct. 20 (2011) 015004
22. Won-Sik Kim, **Daihong Kim**, Kyoung Jin Choi, Jae-Gwan Park, and Seong-Hyeon Hong, "Epitaxial Directional Growth of Tin Oxide (101) Nanowires on Titania (101) Substrate", Crystal Growth & Design 10 (11) (2010) 4746
23. **Dai-Hong Kim**, Won-Sik Kim, Sung Bo Lee, Seong-Hyeon Hong , “Gas sensing properties in epitaxial SnO₂ films grown on TiO₂ single crystals with various orientations” Sensors and Actuators B 147 (2010) 653~659
24. Won-Sik Kim, Byoung-Sun Lee, **Dai-Hong Kim**, Hong-Chan Kim, Woong-Ryeol Yu, Seong-Hyeon Hong, “SnO₂ nanotubes fabricated using electrospinning and atomic layer deposition and their gas sensing performance” Nanotechnology 21 (2010) 245605 (7pp)
25. Myung Yang, **Dai-Hong Kim**, Won-Sik Kim, Tae June kang, Byung Yang Lee, Seunghun Hong, Yong Hyup Kim, Seunghun Hong, “H₂ sensing characteristics of SnO₂ coated single wall carbon nanotube network sensors” Nanotechnology 21 (2010) 215501 (7pp)

26. Ji-Hwan Kwon, Yun-Hyuk Choi, **Dai-Hong Kim**, Myeong Yang, Jiyoun Jang, Tae Woong Kim, Seong-Hyeon Hong and Miyoung Kim, "Orientation relationship of polycrystalline Pd-doped SnO₂ thin films deposits on sapphire substrates" Thin Solid Films 517 (2008) 550~553

International Conference Presentations

1. **Dai-Hong Kim**, Yun-Hyuk Choi, Bo-Kyung Ahn, Hyun-Jung Shin, Seong-Hyeon Hong, "Gas Sensing Performance of AAO Template with TiO₂ Nanotube", 5th Asian Meeting on Electroceramics, Thailand (2006) (Oral)

2. **Dai-Hong Kim**, Seong-Hyeon Hong, "Characterization of Epitaxial SnO₂ Thin Films Grown on Sapphire Substrate Using PE-ALD", 2007 international symposium on organic and inorganic electronic materials and related nanotechnologies, Japan (2007) (Oral)

3. **Dai-Hong Kim**, Yun-Hyuk Choi, Mi-Young Kim, Seong-Hyeon Hong, "SnO₂ thin films on various sapphire substrates prepared by sputtering and PE-ALD" 17th International Vacuum Congress, Sweden (2007) (Poster)

4. **Dai-Hong Kim**, Seong-Hyeon Hong, "Characterization and gas sensing properties of epitaxial SnO₂ films deposited by PE-ALD" International conference on multifunctional materials and structures, Hong Kong (2008) (Oral)

5. **Dai-Hong Kim**, Seong-Hyeon Hong, “Growth of Epitaxial SnO₂ Thin Films on Various TiO₂ Substrates for Gas Sensing applications” 216th ECS Meeting, Austria (2009) (Oral)

6. **Dai-Hong Kim**, Seong-Hyeon Hong, “Defect structures and gas sensing properties of hetero-epitaxial SnO₂ thin films depending on O₂ plasma time” MRS fall meeting, USA (2010) (Poster)

7. **Dai-Hong Kim**, Sungtae Kim, Seong-Hyeon Hong, “Growth of epitaxial TiO₂ thin films on various YSZ substrates for gas sensing applications” 220th ECS Meeting, USA (2011) (Oral)